LAWRENCE
LIVERMORE
NATIONAL
LABORATORY

LLNL-TH-405338

Meso-Scale Modeling of Spall in a Heterogeneous Two-Phase Material

H. Keo Springer

July 11, 2008

Disclaimer

This work performed under the auspices of the U.S. Department of Energy by Lawrence Livermore National Laboratory under Contract DE-AC52-07NA27344.

Meso-Scale Modeling of Spall in a Heterogeneous Two-Phase Material

By

HARRY KEO SPRINGER
B.S. (California State Polytechnic University, San Luis Obispo) 1996
M.S. (Georgia Institute of Technology) 1998

DISSERTATION

Submitted in partial satisfaction of the requirements for the degree of

DOCTOR OF PHILOSOPHY

in

Mechanical and Aeronautical Engineering

in the

OFFICE OF GRADUATE STUDIES

of the

UNIVERSITY OF CALIFORNIA

DAVIS

Approved:

_____

_____

_____

Committee in Charge

2008

Abstract

The influence of the heterogeneous second-phase particle structure and applied loading conditions on the ductile spall response of a model two-phase material was investigated. Quantitative metallography, three-dimensional (3D) meso-scale simulations (MSS), and small-scale spall experiments provided the foundation for this study. Nodular ductile iron (NDI) was selected as the model two-phase material for this study because it contains a large and readily identifiable second- phase particle population. Second-phase particles serve as the primary void nucleation sites in NDI and are, therefore, central to its ductile spall response.

A mathematical model was developed for the NDI second-phase volume fraction that accounted for the the non-uniform particle size and spacing distributions within the framework of a length-scale dependent Gaussian probability distribution function (PDF). This model was based on novel multi-scale sampling measurements. A methodology was also developed for the computer generation of representative particle structures based on their mathematical description, enabling 3D MSS.

MSS were used to investigate the effects of second-phase particle volume fraction and particle size, loading conditions, and physical domain size of simulation on the ductile spall response of a model two-phase material. MSS results reinforce existing model predictions, where the spall strength metric (SSM) logarithmically decreases with increasing particle volume fraction. While SSM predictions are nearly independent of applied load conditions at lower

loading rates, which is consistent with previous studies, loading dependencies are observed at higher loading rates. There is also a logarithmic decrease in SSM for increasing (initial) void size, as well. A model was developed to account for the effects of loading rate, particle size, matrix sound-speed, and, in the NDI-specific case, the probabilistic particle volume fraction model.

Small-scale spall experiments were designed and executed for the purpose of validating closely-coupled 3D MSS. While the spall strength is nearly independent of specimen thickness, the fragment morphology varies widely. Detailed MSS demonstrate that the interactions between the tensile release waves are altered by specimen thickness and that these interactions are primarily responsible for fragment formation. MSS also provided insights on the regional amplification of damage, which enables the development of predictive void evolution models.

Acknowledgements

This research would not have been possible without the support and encouragement of numerous people. A sincere thank you to everyone who helped me along the way, especially those listed below.

The technical guidance provided by the dissertation committee members, Mike Hill (chair), Dana Goto, and Mark Rashid, as well as technical discussions with Rich Becker, Rich Couch, Dan Nikkel and James Stolken were instrumental to the success of this research. I would also like to express gratitude for the experimental support of Jackson Go and David Urabe, as well as the computational support of JoAnne Levatin. A special thanks to Tom Mason and Ben Henrie of Los Alamos National Laboratory for providing their facilities for dynamic experiments and quantitative metallography studies.

I would like to thank my wife, Kristin, son, Noah, and daughter, Kyla, for their love and patience during this long journey. Kristin, none of this would have been possible, or worthwhile, without your support. I would also like to thank my sister, Leila Minugh, brother-in-law, Billy Minugh, and my late mother, Sallie Springer, for their support throughout the years. Special thanks to my late father, Rick Springer, for instilling a passion for science and engineering with Radio Shack hobby kits and his Schaum's Outlines!

The financial support of this research by the Joint DoD-DOE Munitions Technology Development Program is appreciated. This work was performed under the auspices of the U.S. Department of Energy by Lawrence Livermore National Laboratory under Contract DE-AC52-07NA27344.

Table of Contents

1.0 Introduction to the spall of ductile metals

A consequence of impulsive loading, e.g., loading due to high speed impacts or explosive detonation, on ductile metals is spall fracture. The initial impulsive loading results in compressive stress waves that propagate towards the specimen free surfaces. At the free surfaces, the compressive wave is reflected, changes signs, and develops into a tensile release wave. Spall fracture can result from the intersection of tensile release waves or from a single, relatively larger tensile release wave. At the microscopic level, spall fracture is characterized by the rapid nucleation, growth and coalescence of voids in a narrow band. Voids can nucleate at inclusions, second-phase particles, grain boundaries or other microstructural features. Voids grow under tensile loading and coalesce via impingement or localized strain bands. Figure 1.1 illustrates the growth and coalescence of voids in a ductile metal under dynamic tensile loading. Material (void) damage is depicted as a relatively localized process and spall fracture occurs from void-linking under continued loading.

1.1 Review of spall fracture in ductile metals

Hopkinson [1914] was the first to investigate spall and the loading required to produce it. He described the spall fractures in mild steel as having a brittle appearance since it lacked significant plastic deformation and contrasted this with the relative ductility under quasistatic loading conditions. Nearly four decades passed before Rinehart [1952] systematically explored spall in steel, brass, copper and aluminum alloys. He found that a critical value of tensile stress was required to produce spall and surmised that it was an intrinsic material

quantity. Subsequent experimental studies have demonstrated that the loading profile [Tuler and Butcher 1968; Barbee et al. 1972; Davison and Stevens 1972; Cochran and Banner 1977], and temperature [Kanel et al. 1997, Duffy and Ahrens 1994] influence the spall strength in ductile metals. Fewer studies have investigated the role of microstructure on ductile spall. While grain size [Christy et al. 1986; Minich et al. 2004] and purity levels [Rivas et al. 2000] have been investigated, there have been no systematic correlations between these microstructural features and void nucleation sites.

Analytical spall modeling has traditionally been focused on the dynamic growth of an isolated void under hydrostatic loading [Poritsky 1952; Carroll and Holt 1972; Johnson 1981; Ortiz and Molinari 1992; Wu et al. 2003], axisymmetric loading [Banks-Sills and Budiansky 1982], and general load triaxialitiy conditions [Cortes 1992; Wang 1994; Wang 1997]. These analytical models have provided valuable insights, demonstrating the influence of load amplitude and duration, inertia, temperature, as well as strain and strain-rate hardening, on the micromechanisms of ductile spall failure. However, isolated void growth models can overpredict the material spall resistance because they do not account for the influence of neighboring voids.

Two-dimensional meso-scale simulations (MSS) have demonstrated the influence of the void structure on spall failure [Benson 1993; Tonks et al. 1995; Tonks 1996]. Tonks et al. [1995; 1996] showed that spall at higher strain-rates was stochastic, consisting of many individual void clusters growing independently and impinging with little prior interaction. At lower strain-rates, a single, dominant

void cluster facilitated spall failure. Benson [1993] found that the variation of the peak transmitted stress, a spall strength metric, due to changing the void distributions was as large as the variation associated with doubling the void fraction (nearly 20%). Since these previous studies were based on plane strain analyses without representative material mesostructures, however, they did not rigorously capture the complex, three-dimensional interactions that occur during the spall process. This is discussed further in Section 1.2.5.

Further information on ductile spall can be found in the reviews of Davison et al. [1979], Meyers et al. [1983], Curran et al. [1987], Grady [1988], and Antoun et al. [2003].

1.2 Parameters affecting spall fracture in ductile metals

Previous studies have shown that the loading profile, initial temperature, strain-rate hardening, inertia, and microstructure influence the spall fracture in ductile metals. At the microscale, these parameters can affect void nucleation, growth, or coalescence. Each of these parameters is discussed in the following sections.

1.2.1 Loading profile

Spall fracture in ductile metals has been shown to have a time-dependent character [Tuler and Butcher 1968; Barbee et al. 1972; Davison and Stevens 1972; Cochran and Banner 1977]. Tuler and Butcher [1968] showed that the applied tensile stress magnitude needed to dynamically (spall) fracture aluminum 1100 (pure) and aluminum alloy 6061-T6 decreased with increasing applied tensile stress duration. Interestingly, aluminum 1100, with a lower quasistatic

tensile strength than 6061-T6 aluminum, required a larger applied tensile stress to fracture at fixed applied tensile stress duration. This might result from the higher density of defects in the alloyed aluminum that served as potential void nucleation sites. The work of Tuler and Butcher [1968] provided a foundation for subsequent cumulative (void) damage models [e.g., Barbee et al. 1972; Davison and Stevens 1972].

While void growth is only one micromechanism of the spall process, it is helpful for determining important parameters affecting spall fracture. Analytical void growth models have demonstrated time dependencies, e.g., Poritsky [1952] model of a void in an infinite viscous matrix under remote loading:

$$\frac{d^2R}{dt^2}+\frac{3}{2R}\left(\frac{dR}{dt}\right)^2+\frac{4\eta}{\rho R^2}\frac{dR}{dt}+\frac{2\gamma}{\rho R^2}=\frac{\sigma-\sigma_{g0}}{\rho R} \qquad 1\ (C.1)$$

$$\frac{dR}{dt}=\frac{\sigma-\sigma_{g0}}{4\eta}R \qquad 2\ (C.1)$$

$$\frac{R}{R_0}=\exp\left[\frac{\sigma-\sigma_{g0}}{4\eta}\right]\tau \qquad 3\ (C.1)$$

Where R_0, R is the initial and current void radius, η is the material viscosity, ρ is the material density, γ is the surface tension, σ is the hydrostatic compression, σ_{g0} is the threshold void growth tension, and t is the time. As in Barbee et al. [1972], the left hand side of Equation (1.1) is simplified to Equation (1.2) by only considering the third term, all other higher order terms being negligible in comparison. Equation (1.3) was derived for the case of a square applied tensile wave and is consistent with the notions of applied tensile stress magnitude and duration discussed previously.

1.2.2 Initial temperature

The spall strength has been shown to be dependent on initial temperature [Kanel et al. 1997, Duffy and Ahrens 1994]. Kanel et al. [1997] showed that the spall strength in Aluminum AD1 (nominally aluminum 1100) decreases with increasing initial temperature. The decrease with initial temperature is more rapid near the melting temperature. Also, sensitivity to shock pressure is more significant near the melt temperature because shock heating in this regime can be sufficient enough to melt the material.

1.2.3 Strain-rate hardening

Strain-rate hardening has been shown to affect the void growth predicted by analytical models of isolated voids under hydrostatic loading [Ortiz and Molinari 1992; Wu et al. 2003] and general load triaxialitiy conditions [Wang 1997]. Wu et al. [2003] showed that increased material strain-rate hardening reduces void growth rate and eventual void size. Wang [1997] showed that strain-rate sensitivity had a significant effect at smaller void volume fractions (0.5% to 1%) and only a slight effect at larger void volume fractions (25%). The strain-rate sensitivity parameter is also shown to increase with the load triaxiality for a given value of void volume fraction.

1.2.4 Inertia

Analytical models have confirmed that inertia, hence material density, retards the growth of voids [Poritsky 1952; Ortiz and Molinari 1992; Wang 1997; Wu et al. 2003]. Wang [1997] showed that the inclusion of inertia can reduce the void growth rate by an order-of-magnitude in comparison to the inertia-free case

for void volume fractions exceeding 15%. Using Equation (1.1), Antoun et al. [2003] showed that for void radii up to 10 μm inertia effects are insignificant. For void radii greater than 100 μm, however, inertia effects are pronounced and impede void growth. The reduction of inertia effects in smaller voids enables them to grow relatively faster than the larger voids and, at relatively late-times, significantly reduce the initial size differential. Wu et al. [2003] showed that inertia effects are more pronounced with higher loading rates and was strongly dependent on the initial void size. At relatively late-times, however, voids of all sizes achieved a constant, absolute void growth rate.

1.2.5 Microstructure

1.2.5.1 Experimental studies

The effects of grain size in copper [Christy et al. 1986; Minich et al. 2004] and purity levels in tantalum [Rivas et al. 2000] on spall fracture have been previously investigated. Christy et al. [1986] showed that the spall strength in polycrystalline copper increases with decreasing grain size, analogous to the Hall-Petch relation. While they found that voids nucleated primarily at the grain boundaries for their high purity copper samples, the eventual fracture is facilitated by voids within and on the boundaries of the copper grains.

Minich et al. [2004] showed that the pullback velocity, a metric of spall strength, was significantly lower for 8 μm (average) grain sizes than for 45 to 80 μm grain sizes in polycrystalline copper at shock pressures exceeding 20 GPa. This result directly contrasts with the Hall-Petch relationship. A possible explanation for this result is that the smaller grain sizes, with a larger grain

boundary surface area per unit volume, have more potential for nucleating voids at the boundaries. However, it takes a relatively higher shock pressure to nucleate those voids in comparison to voids inside the grains. It is important to characterize the three-dimensional nature of the grain structure since it influences the localized loading and, in turn, nucleation of voids at the grain boundaries.

Rivas et al. [2000] found that under identical loading conditions, commercial purity tantalum exhibited more incipient spall damage (27% void volume fraction) than high purity tantalum (6% void volume fraction). An explanation for this result was that the commercial purity tantalum contained a higher defect density, enabling the nucleation of relatively more voids under the same loading conditions. Without characterizing the three-dimensional defect structure, though, it is difficult to fully assess how it affects the spall response. In order to develop predictive spall fracture models, it is therefore important to correlate the three-dimensional microstructure to the void nucleation sites. In the current study, a model two-phase material was selected on the basis that its primary void nucleation site structure is readily quantifiable. Void nucleation site structure can be incorporated into predictive spall fracture models or used as the basis for seeding MSS.

Although for quasi-static loading, the experimental investigation of Magnusen et al. [1988] provided insight on the role of void clustering on ductile fracture. They showed that plates with uniformly distributed holes (i.e., macroscopic voids) have larger strain-to-failure than plates with randomly

distributed voids under identical tensile loading conditions. They surmised that void growth and coalescence are accelerated in the plates with randomly distributed voids because those plates contain void clusters that locally concentrate stress and strain. This effect is more prominent in low strain-hardening materials due to increased susceptibility to plastic flow instabilities. These studies suggest that it is important to include the complex, non-uniform (i.e., higher dimensional) nature of the void structure in MSS to capture the realistic fracture behavior of ductile metals. In contrast, the assumption of uniform void size and spacing will likely contribute to the overestimation of a material's resistance to fracture.

1.2.5.2 Two-dimensional MSS

Two-dimensional MSS have demonstrated that void clustering can accelerate the spall fracture process [Benson 1993] and modify spall fracture behavior with strain-rate [Tonks et al. 1995, 1996]. Moreover, including detailed microstructure in MSS permits the study of the spatial variability in spall fracture response [Vogler and Clayton 2007].

Benson [1993] found that the variation of the peak transmitted stress, a spall strength metric, due to changing the void distributions is as large as the variation associated with doubling the void fraction (nearly 20%). Tonks et al. [1995; 1996] showed that spall fracture at higher strain-rates was stochastic, consisting of many individual void clusters growing independently and impinging with little prior interaction. These results suggest that it is critical to include the

detailed void structure in simulations, including the void size and spacing distribution, to most accurately capture its spall fracture response.

Vogler and Clayton [2007] employed two-dimensional MSS in an effort to model experimentally measured variations in the pull-back signal of shocked tungsten heavy alloy. The pull-back signal is derived from the free surface velocity measurements and is a metric of the spall strength. Measured spatial variations in the spall strength metrics were attributed to the heterogeneous nature of this material. While their predicted spall strength variations were qualitatively similar to experimental measurements, the physical domain size of the simulation is believed to contribute to quantitative differences. These results suggest that the physical domain size of the simulation is important and needs to be considered in any new studies of the spatial variability in spall fracture.

1.2.5.3 Necessity for three-dimensional microstructure in MSS

Analytical models of isolated, spherical voids have demonstrated the influence of loading profile, initial temperature, strain-rate hardening, inertia, as well as void size and volume fraction on the dynamic growth of voids. However, these models do not account for void growth alterations arising from the interaction with neighboring voids. This is particularly important for materials that have a large initial volume fraction of void nucleation sites, such as the model material in this study (nodular ductile iron (NDI)), where individual void stress and strain fields overlap at the onset of loading. Not only is it necessary to include the interactions with neighboring voids, but also the non-uniformity of these

interactions. It has been demonstrated experimentally [Magnusen et al. 1988] and numerically [Benson 1993] that microstructural heterogeneity can have a significant impact on the damage and fracture response of materials. Since many engineering materials have heterogeneous microstructures, including NDI, it is then important to capture this aspect in MSS. Predictive meso-scale modeling requires incorporation of multiple void nucleation sites with material-representative size and spacing distributions, intrinsically making these simulations two- or three-dimensional. The need for three-dimensional, rather than two-dimensional, microstructure is discussed further below.

MSS have demonstrated the influence of two-dimensional microstructure on the spall fracture response of materials under impulsive loading conditions [Benson 1993; Tonks et al. 1995, 1996; Vogler and Clayton 2007]. These studies were based on plane-strain conditions, i.e., the void nucleating features were assumed to be cylindrical. The validity of this assumption is partially dependent on the specific material under investigation. Since the void nucleation sites in NDI consist of spherical, not cylindrical, graphite particles, plane-strain analysis is qualitatively inappropriate. There are also quantitative differences in void growth for cylindrical and spherical voids. The growth of a spherical void can be as much as 200% greater than than of an equally-sized cylindrical void under (identical) imposed displacements (see Appendix A). This result is based on the assumption of equal void volume fraction, void size, and work rate (energy) for both types of voids. The models of McClintock [1968] and Rice and Tracey [1969] for the growth of a cylindrical void (under plane-strain) and a spherical

void, respectively, in a rigid-perfectly plastic matrix are also quantitively different. In addition, void coalescence differs for cylindrical and spherical voids. Thomason [1968, 1999] qualitatively demonstrated that the coalescence geometry for cylindrical voids under plane-strain conditions involves the intersection of triangular wedges of plastic strain. The coalescence geometry for spherical voids involves the intersection of conical regions of plastic strain. Considering the shape of void nucleation features in NDI and the differences in void growth and coalescence mechanisms, it is appropriate to model the graphite second-phase particles as spheres in a *three-dimensional MSS*.

1.3 Outline of current work

The objective of this study is to investigate the effects of the second-phase particle structure and loading conditions on the ductile spall response of a model two-phase material. Quantitative metallography, three-dimensional meso-scale simulations (MSS), and small-scale spall experiments provide the foundation for this study. Nodular ductile iron (NDI) was selected as the model two-phase material for this study because it contains a large and readily identifiable second-phase particle population. Second-phase particles serve as the primary void nucleation sites in NDI and are, therefore, central to its ductile spall response.

In Chapter 2, a mathematical description for the three-dimensional second-phase particle structure in NDI that includes the size and spatial distributions of those particles will be developed. Additionally, a methodology for the computer generation of representative particle structures based on their

mathematical description will be developed, enabling detailed three-dimensional MSS in Chapters 3 and 4. Previous studies have not systematically characterized the void-nucleating sites relevant to the micromechanisms of ductile spall or integrated this information into three-dimensional MSS.

The primary goal of Chapter 3 is to utilize three-dimensional MSS to investigate the effects of second-phase particle size and spacing distributions, loading conditions, and length-scale on the spall response of a model two-phase material. Previous modeling studies have been, at most, two dimensional and did not consider representative microstructures. This prevents accurate depiction of the complex, three-dimensional interactions that influence void growth and coalescence in ductile metals. A spall strength model will be developed that accounts for the influence of the microstructure, loading, and length-scale parameters under study.

In Chapter 4, small-scale spall experiments will be designed and executed for the purpose of validating closely-coupled three-dimensional MSS. These experiments will probe the effects of specimen geometry on NDI spall behavior under impulsive loading. Fragment size and spall strength will be used as the primary valiation metrics. Previous studies have not attempted to couple MSS directly to experiments, preventing direct validation of simulations. MSS will be performed to gain insights on the response of NDI to explosive loading.

1.4 Figures

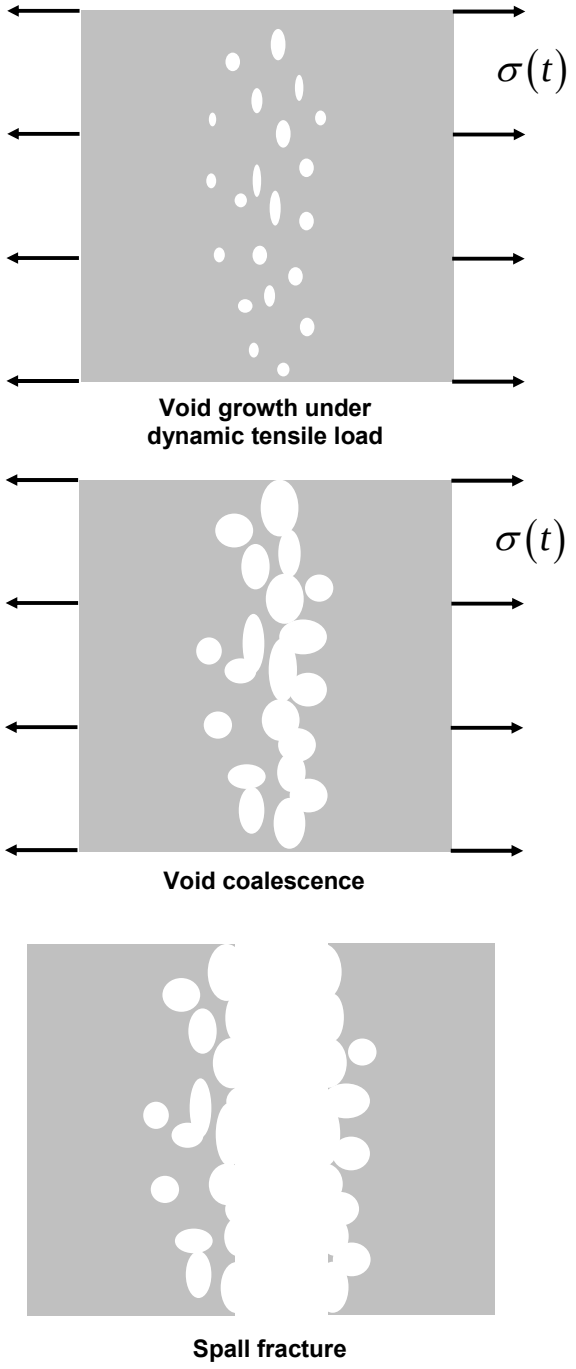

Figure 1.1: Void growth, coalescence, and spall fracture of a ductile metal under dynamic tensile loading.

1.5 References

T Antoun, L Seaman, DR Curran, GI Kanel, SV Razorenov, AV Utkin; *Spall Fracture*; Springer-Verlag New York, Inc. (2003)

L Banks-Sills, B Budiansky; *On void collapse in viscous solids*; Mechanics of Materials 1 (1982) 209-218

TW Barbee Jr., L Seaman, R Crewdson, D Curran; J. Materials 7 (1972) 393
R Becker; *The Effect of Porosity Distribution on Ductile Failure*; Journal of the Mechanics and Physics of Solids, 35:5 (1987) 577-599

R Becker; *The Effect of Porosity Distribution on Ductile Failure*; Journal of the Mechanics and Physics of Solids, 35:5 (1987) 577-599

DJ Benson; *An Analysis of Void Distribution Effects on the Dynamic Growth and Coalescence of Voids in Ductile Metals*; Journal of the Mechanics and Physics of Solids, 41:8 (1993) 1285-1308

MM Carroll, AC Holt; *Static and dynamic pore-collapse relations for ductile porous materials*; J. Appl. Phys. 43 (1972) 1626-1636

S Christy, HR Pak, MA Meyers; in *Metallurgical Applications of Shock-Wave and High-Strain-rate Phenomenon* edited by LE Murr, KP Staudhammer, MA Meyers; Dekker, New York (1986) 835

S Cochran, D Banner; *Spall studies in uranium*; J. Appl. Phys. 48:7 (1977) 2729-2737

R Cortes; *Dynamic growth of microvoids under combined hydrostatic and deviatoric stresses*; International Journal of Solids and Structures, 29:13 (1992) 1637-1645

DR Curran, L Seaman, DA Shockey; *Dynamic Failure of Solids*; Physics Reports, 147:5-6 (1987) 253-388

L Davison, AL Stevens; *Continuum measures of spall damage*; J. Appl. Phys. 43:3 (1972) 988-994

L Davison, RA Graham; *Shock Compression of Solids*; Physics Reports 55:4 (1979) 255-379

TS Duffy, TJ Ahrens; *Dynamic Response of Molybdenum Shock Compressed at 1400°C*; J. Appl. Phys. 76:2 (1994) 835-842

DE Grady; *The spall strength of condensed matter*. Journal of the Mechanics and Physics of Solids, 36 (1988) 353-384

B Hopkinson; Trans. R. Soc. London, 213A (1914) 437

Y Huang; *The role of nonuniform particle distribution in plastic flow localization*; Mechanics of Materials, 16 (1993) 265-279

JN Johnson; *Dynamic fracture and spallation in ductile solids*; Journal of Applied Physics, 52:4 (1981) 2812-2825

GI Kanel, SV Razorenov, A Bogatch, AV Utkin, DE Grady; *Simulation of spall fracture of aluminum and magnesium over a wide range of load duration and temperature*; Int. J. Impact Engng. 20 (1997) 467-478

PE Magnusen, EM Dubensky, DA Koss; *The Effect of Void Arrays on Void Linking During Ductile Fracture*; Acta Metallurgica 36:3 (1988) 1503-1509

FA McClintock; *A Criterion For Ductile Fracture by the Growth of Holes*; Journal of Applied Mechanics, 35 (1968) 363-371

MA Meyers, CT Aimone; *Dynamic fracture (spalling) of metals*; Progress in Materials Science 28 (1983) 1-96

RW Minich, JU Cazamias, M Kumar, AJ Schwartz; *Effect of microstructural length scales on spall behavior of copper*; Metallurgical and Materials Transactions A, 35A (2004) 2663-2673

N Ohno, JW Hutchinson; *Plastic Flow Localization Due to Non-Uniform Void Distribution*; Journal of the Mechanics and Physics of Solids, 32:1 (1984) 63-85

M Ortiz, A Molinari; *Effect of strain hardening and rate sensitivity on the dynamic growth of a void in a plastic material*; Transactions of the ASME, Journal of Applied Mechanics 59 (1992) 48-53

H Poritsky; *The collapse or growth of a spherical bubble or cavity in a viscous fluid*; in the Proceedings of the First U.S. National Congress on Applied Mechanics, ASME, New York (1952) 813

JR Rice, DM Tracey; *On The Ductile Enlargement of Voids in Triaxial Stress Fields*; Journal of the Mechanics and Physics of Solids, 17 (1969) 201-217

JS Rinehart; *Scabbing of metals under explosive attack: Multiple scabbing*; Journal of Applied Physics, 23 (1952) 1229

JS Rinehart, J Pearson; *Behavior of metals under impulsive loads*; Dover Publications, Inc (1965) (originally published by the American Society of Metals in 1954)

JM Rivas, AK Zurek, WR Thissell, DL Tonks, RS Hixson; *Quantitative description of damage evolution in ductile fracture of tantalum*; Metallurgical and Materials Transactions A, 31A (2000) 845-851

PF Thomason; J. Inst. Metals, 96 (1968) 360-367

PF Thomason; *Ductile spallation fracture and the mechanics of void growth and coalescence under shock-loading conditions*; Acta mater. 47:13 (1999) 3633-3646

DL Tonks, AK Zurek, WR Thissell, in *Metall. and Materials Applications of Shock-Wave High-Strain-Rate Phenomena*, edited by L. E. Murr et al, Elsevier, (1995) 171 – 178

DL Tonks in *Shock Compression of Condensed Matte: Dynamic Fracture and Fragmentation;* edited by L Davison et al. Springer Verlag New York, Inc. (1996) 237-263

FR Tuler, BM Butcher; Int. J. Fract. Mech., 4 (1968) 431

TJ Vogler, JD Clayton; *Heterogeneous deformation and spall of an extruded tungsten alloy: plate impact experiments and crystal plasticity modeling*; Journal of the Mechanis and Physics of Solids (2007) in press

ZP Wang; *Void growth and compaction relations for ductile porous materials under intense dynamic general loading conditions*; Int. J. Solids Structures, 31:15 (1994) 2139-2150

ZP Wang; *Void-containing nonlinear materials subject to high-rate loading*; J. Appl. Phys. 81:11 (1997) 7213-7227

XY Wu, KT Ramesh, TW Wright; *The dynamic growth of a single void in a viscoplastic material under transient hydrostatic loading*; Journal of the Mechanics and Physics of Solids, 51 (2003) 1-26

2.0 Characterization of the void nucleation sites in a model two-phase material

2.1 Introduction

In order to improve the understanding of the micromechanisms of ductile spall, it is important to identify and characterize the microstructural features relevant to void nucleation. Voids can nucleate at inclusions, second-phase particles, grain boundaries or other microstructural features. A limited number of experimental studies have explicitly considered the effects of initial microstructure on the spall response of metals [Christy et al. 1986; Rivas et al. 2000; Minich et al. 2004]. While these studies investigated the effects of average grain size and impurity levels, rigorous characterization of the microstructural features relevant to void nucleation was not performed. It is difficult to characterize void nucleation sites because they may not be readily discernable from other microstructural features and are non-uniformly sized and spaced.

The first objective of this chapter is to develop a mathematical description for the three-dimensional second-phase particle structure in a model material that includes the size and spatial distributions of those particles. Nodular ductile iron (NDI) was selected as the model material for this study because it contains a readily identifiable second-phase particle population. These particles serve as the primary void nucleation sites in NDI, i.e., particle structure quantification is tantamount to (potential) void nucleation site characterization. A high-order mathematical description of the particle structure that includes the small-scale heterogeneity is important to spall failure modeling in NDI.

The second objective of this chapter is to develop a methodology for the computer generation of representative particle structures based on the mathematical description developed in the first objective. Computer generation methods that accurately account for the mathematical description of the complex, three-dimensional particle structure enable detailed meso-scale simulations (MSS). MSS are important because they provide the foundation for small-scale and macro-scale structure-spall response studies that follow in subsequent chapters. Comparisons of the computer generated realization to the experimental measures of the particle structure were performed to verify accuracy of the particle generation methods.

2.2 Methods

2.2.1 Nodular ductile iron (NDI)

ASTM A536, 60-40-18 NDI was selected as the model two-phase material for this study. The material used for this study was purchased from DuraBar®. NDI is a Fe-C-Si alloy and its chemical composition is shown in Table 2.1. NDI comprises a ductile matrix (first phase) with loosely-bound, large graphite particles (second-phase). These particles are central to its ductile fracture response [Clough et al. 1957; Shi et al. 1992; Liu et al. 2002], i.e., voids nucleate primarily at the graphite particles. Figure 2.1 depicts the two-phase microstructure of NDI in a undeformed metallographic section (Figure 2.1a) and in a fractograph (Figure 2.1b). The fractograph demonstrates that the voids nucleate at the graphite particles, signifying their central role in NDI ductile fracture. In the metallographic section, the graphite second-phase is the darker

particles within the contiguous matrix phase. These large and nearly spherical graphite particles make NDI well-suited for quantitative metallography studies.

2.2.2 Mathematical description of the particle structure in NDI

The development of a mathematical description of the three-dimensional particle structure in NDI consisted of the following steps: preparation of a metallographic specimen; capture of a digital image montage; extraction of particle structure data from digital image; and, analysis of particle structure data, including the calculation of particle area fraction, size distribution, and nearest neighbor distance.

Metallographic sections of undeformed NDI formed the basis for all particle structure characterization. Image analysis software was used to extract the raw particle structure data, i.e., particle size and coordinates, from the metallographic sections of undeformed NDI. Particle area fraction, size distribution, and area fraction fluctuations were calculated directly from the particle structure data. Particle area fraction fluctuations are discussed further below. Where necessary, these quantities were transformed to a three-dimensional form based on the assumption of a polydispersed system of spheres, i.e., a system of randomly and isotropically positioned spheres with a measurable size distribution [Underwood 1972; Corti et al. 1974]. The nearest neighbor distance was calculated directly from the particle volume fraction.

2.2.2.1 Metallographic specimen preparation

Particle structure characterization was performed on a metallographic section of undeformed NDI. The specimen was taken from the mid-radius of the

as-received NDI round stock, following the process for specimen preparation described in ASTM E-8 *Standard Test Methods For Tension Testing of Metallic Materials*. The mounted specimen was hand ground on successively finer SiC-impregnated polishing papers, starting with 320-grit and finishing with 4000-grit paper. The specimen was then promptly polished on a Struers TegraPol using a nylon cloth with an aqueous solution of 3 μm diamond particles, washed with soap and water, and rinsed in flowing water. The specimen was then polished with 1 μm diamond on a nap cloth, washed and rinsed. The specimen was then given a final polish on a nap cloth with an aqueous solution of 0.04 μm colloidal silica, washed with water, rinsed with ethanol and dried. The specimen was not etched.

2.2.2.2 Digital image montage and extraction of particle structure data

A Reichert-Jun MeF3 inverted optical microscope with an automated two-axis stage was used to capture and montage approximately 150 high resolution two dimensional images. Approximately 70,000,000 μm^2 of metallographic section data were captured at a resolution of 1.36 μm/pixel. Quantitative metallography analyses based on large image montages of the two-dimensional metallographic sections has been shown to be more representative of the particle structure than limited, high-magnification sampling [Shan et al. 2002; Yang et al. 1997]. While the graphite phase is clearly recognizable in these images, further enhancements to the image contrast were necessary prior to raw data extraction.

Image Pro Plus software was used to enhance the image montage and then extract raw particle structure data from the montage. Image enhancements were performed in order to expedite the particle structure quantification process. The image gamma value was reduced from 1.0 to 0.5 and the contrast was increased from 50 to 80, effectively making the matrix phase appear white and the particle phase appear black. An automated counting feature of Image Pro Plus was then used to obtain centroid position and mean diameter of all identified particles. These particle structure data were exported as an ASCII text file for subsequent analysis.

2.2.2.3 Particle area and volume fraction

The particle area fraction is a key scalar descriptor of the particle structure that is derived from the fundamental particle size and spacing distributions. It will be incorporated in the computer generation of representative particle structures and the development of particle structure models. The particle area fraction was calculated from the particle structure data over the *entire montage* by taking the sum of the individual particle areas divided by the total area over which measurements were taken:

$$\Phi_0 = \frac{\sum_{i=1}^{N_{tot}} A_i}{A_{tot}} \tag{2.1}$$

Where Φ_0 is the (initial) macro-scopic particle area fraction, N_{tot} is the total number of particles over the entire image montage, A_i is the area of the current particle, and A_{tot} is the total measurement area of the entire montage

(70,000,000 μm^2). Since the particle area fraction was calculated over the entire image montage, it is referred to as the macro-scopic particle area fraction. In statistical terms, Φ_0 is the mean particle area fraction of the *entire population*. This is an important clarification, as Φ_0 is used to develop statistical sampling methods in Section 2.2.2.6.

2.2.2.4 Particle size distribution

The three-dimensional particle size distribution is important for the computer generation of representative particle structures. In order to determine the three-dimensional particle size distribution, it was necessary to transform the two-dimensional particle size distribution using the process described by Saltykov [1967]. The transformation requires binning of the two-dimensional particle size data. The transformation equations used for this process are:

$$N_{V,i} = \frac{1}{D_i} \sum_{j=1}^{i} N_{A,j} C_j \tag{2.2}$$

$$C_j^T = \left[1.6461, -0.4561, -0.1162, -0.0415, -0.0173, -0.0079\right] \tag{2.3}$$

Where $N_{V,i}$ is the *ith* volume bin count, $N_{A,j}$ is the *jth* area bin count, and C_j is the Saltykov transformation constants. Based on the use of six bins in this study, D_i, the *ith* (two dimensional) bin diameter, was calculated with:

$$D_i = \frac{1}{2}\left(\frac{D_{\max}}{6}\right) + \left(\frac{(i-1)D_{\max}}{6}\right) \tag{2.4}$$

Where $D_{\max}$ is the maximum measured particle diameter. The count for each area bin, $N_{A,j}$, was determined using a simple binning algorithm on the two-

dimensional particle structure data. The data has been sorted into six different bins ranging in average size from 17.3 to 104.2 μm, with a bin extent of approximately 17 μm.

2.2.2.5 Particle nearest neighbor distance

The three-dimensional nearest neighbor distance is important for developing a particle structure model, providing a microstructural length-scale. Since no methods exist for transforming two-dimensional nearest neighbor distance distributions to a three-dimensional quantity, a relationship based on Corti et al. [1974] was used to determine the three-dimensional nearest neighbor distance from the particle volume fraction. The relationship for nearest neighbor distance is:

$$L_{nn} = r\left(\frac{\exp\left(8\Phi_0\right)}{3\Phi_0^{\frac{1}{3}}}\right)\Gamma\left(\frac{1}{3}, 8\Phi_0\right) \tag{2.5}$$

Where L_{nn} is the average three-dimensional edge-edge nearest neighbor distance, r is the average particle radius, Φ_0 is the macro-scopic particle volume fraction, and Γ is the gamma distribution function. This relationship assumes a monodispersed system of spheres, i.e., randomly positioned but with uniform size. The graphite particles in NDI are actually a polydispersed system of spheres, i.e., a system of randomly and isotropically positioned spheres with a measurable size distribution. This assumption is inconsequential because L_{nn} is used to normalize the sampling size in Section 2.2.2.6 and not as a stand-alone microstructural metric.

2.2.2.6 Particle area and volume fraction fluctuations

Particle area and volume fraction fluctuations represent a higher order particle structure metric that provides a measure of the spatial dispersion, e.g., clustering, of the particle area and volume fraction with length-scale. Quintanilla et al. [1997] and Torquato [2002] defined the particle volume fraction fluctuations as the particle volume fraction coefficient-of-variation (COV). In their definition of the COV, the standard deviation of the particle volume fraction *sample ensemble* is divided by the macro-scopic particle volume fraction i.e., the mean particle volume fraction of the *entire* particle population.

A novel, multiscale sampling technique was developed to statistically determine the length-scale dependent area fraction fluctuations from the raw particle structure data. An ensemble of equally-sized sampling windows was generated, each centered at random locations in the particle structure domain (Figure 2.2). The particle area fraction, ϕ_i, of the *ith* sampling window was determined:

$$\phi_i\left(L_k\right) = \frac{\sum_{j=1}^{N_{particles}} A_{part,j}}{L_k^2} \tag{2.6}$$

Where $L_k \; x \; L_k$ is the area of the (square) sampling window, $A_{part,j}$ is the area of the *jth* particle and there are $N_{particles}$ in the sampling window. The sampling ensemble consists of $N_{samples}$ total windows. The subscript *k* refers to the *kth* window size. Equation (2.6) is identical to Equation (2.1) with the exception that

(2.1) is calculated over the entire digital image montage (macro-scale) and (2.6) is calculated over a small sample of the image montage. The smaller sample sizes in Equation (2.6) are expected to yield larger particle area fraction COV. As part of determining the COV, the standard deviation, $S_\phi(L_k)$, over the entire sample ensemble is calculated:

$$S_\phi(L_k) = \sqrt{\frac{\sum_{i=1}^{N_{samples}} \left(\phi_i(L_k) - \Phi_0\right)^2}{N_{samples}}} \tag{2.7}$$

$$COV_\phi(L_k) = \frac{S_\phi(L_k)}{\Phi_0} \tag{2.8}$$

Where $S_\phi(L_k)$ is the standard deviation of the particle area fractions for a fixed window size (fixed L_k), $N_{samples}$ is the total number of samples (100 samples used), Φ_0 is the macro-scopic particle area fraction, and COV_ϕ is the particle area fraction COV at the fixed window size. Quintanilla et al. [1997] and Torquato [2002] used Φ_0 in COV_ϕ because it simplifies arguments for convergence with increased window size, i.e., as the length-scale becomes large, the COV approaches zero. Torquato [2002] argued that normalization with the sample mean, rather than the “true” mean of the entire particle population, would not necessarily guarantee convergence with increased sampling window size. As shown in Figure 2.2, this analysis was repeated for a range of sampling window sizes, $L_0, L_0 + \Delta L, L_0 + 2\Delta L$, where L_0 is 25 μm and ΔL is 25 μm.

As with the 1:1 transformation between particle area and volume fractions for a polydispersed system of spherical particles, it was assumed that a 1:1

transformation also applies for area fraction fluctuations on a sample-per-sample basis. Therefore, the non-dimensional particle area fraction COV measurements above were treated as particle volume fraction fluctuations.

Random positioning of sampling windows reflected the uncorrelated nature of the NDI particle size and spacing distributions. This is particular true at the smallest window sizes considered in this study. Since the NDI second-phase particles are assumed to be isotropic, the directionality was not considered in the sampling process. These assumptions will be discussed further in Section 2.4.

2.2.3 Computer generation of representative particle structures

A methodology for the computer generation of representative particle structures was developed. This methodology was based on the mathematical description of the particle structure and required the following parameters to generate representative particle structures: bounding box spatial extents, particle spacing distribution, particle size distribution parameters, and macro-scopic particle volume fraction.

The spatial extents of the bounding box were described by: $x_{\min} \le x \le x_{\max}$, $y_{\min} \le y \le y_{\max}$, and $z_{\min} \le z \le z_{\max}$. The spatial extents of the rectangular domain bounded the random number generator that was used for initial particle placement. Random and random-clustered particle spacing distributions were used in this study. In random particle generation mode, finite sized particles may overlap. Particle overlap was checked when particles were initially placed. If the non-overlapping option was activated, then the edge-edge nearest neighbor distance was checked with each new particle generation. If this value was

negative, i.e., particle overlap, then the coordinate for the current particle was discarded and another set of coordinates was determined using the random number generator. This process was repeated until the current particle did not overlap existing particles. A Weibull probability distribution function (PDF) was used to model the polydisperse system of particles in this study. To prevent unrealistically large or small particle generation, a maximum and minimum particle radius cutoff was implemented with the Weibull PDF.

A macro-scopic particle volume fraction, Φ_0, with an associated user-defined tolerance, ε, was used to constrain the total number of particles seeded in a specified bounding box region. Particle generation continued until the particle volume fraction criteria, $\Phi_0 - \varepsilon \le \phi \le \Phi_0 + \varepsilon$, was met. Total particle volume fraction was calculated after each particle was generated. For the non-overlapping option, the total particle volume fraction was a sum of the (spherical) particle volumes:

$$\phi_{gen} = \frac{\frac{4}{3}\pi \sum_{i=1}^{N_{part}} (r_i)^3}{(x_{\max} - x_{\min})(y_{\max} - y_{\min})(z_{\max} - z_{\min})} \tag{2.9}$$

Where ϕ_{gen} is the particle volume fraction of the generation, N_{part} is the total number of particles, and r_i is the radius of the *ith* spherical particle. For overlapping particles, a Monte Carlo technique requiring the random placement of many thousands of sampling points was used to determine the total particle volume fraction. In this, the particle total volume fraction was the ratio of the number of sampling points in the particle phase to the total number of sampling

points. While this section describes the utilization of particle domain spatial extents, particle volume fraction, particle size distribution, and random particle spacing for particle generation, spatial clustering beyond that achieved by random placement is not considered.

To account for the random-clustered structure, i.e., spatially clustered, a nearest-neighbor based clustering algorithm was developed. An initially random set of *n* particles is generated, where $\mathbf{p}_n$ denotes the *nth* particle position. The position of the *nth* particle's nearest neighbor, $\mathbf{p}_{NN}$, is then determined. For each iteration, a new particle position, $\mathbf{p}_{n+1}$, is calculated:

$$\mathbf{p}_{n+1} = \mathbf{p}_n + f(A,\alpha)\left(\mathbf{p}_{NN} - \mathbf{p}_n\right) \tag{2.10}$$

$$f(A,\alpha) = (1-A)\exp\left[\frac{\ln(1/2)}{\alpha} + A\right] \tag{2.11}$$

Where $f(A,\alpha)$ returns a value from 0 to 1*, A* is the user-defined asymptotic value of the decaying exponential function (0<A<1), and *α* is the user-defined steepness value of the decaying exponential function (0< *α* <1). The degree of clustering obtained is based on clustering of initial set of particles, values of A and *α* (fixed for iterations), and the number of iterations through the algorithm. Also, for a fixed number of algorithm iterations, decreasing A and *α* increased the clustering tendencies of the particle set.

2.3 Results

2.3.1 Mathematical description of the particle structure in NDI

The particle area and volume fraction, size distribution, nearest neighbor distance, as well as particle area and volume fraction fluctuations were used to develop a mathematical description of the NDI particle structure.

2.3.1.1 Macro-scopic particle area and volume fraction

The NDI macro-scopic particle area fraction, Φ_0, is 0.115. Since the particle area fraction and the volume fraction are identical for a polydispersed system of spheres [Underwood 1972; Corti et al. 1974], the macro-scopic particle volume fraction, also denoted by Φ_0, is 0.115.

2.3.1.2 Three-dimensional particle size distribution

A two parameter Weibull probability distribution function (PDF) with lower (17 μm) and upper (100 μm) particle size bounds was used to fit the (transformed) three-dimensional particle diameter, D, data (Figure 2.3). :

$$P(D) = \frac{\beta D^{\beta-1}}{\eta^{\beta}} \exp\left(-\left(\frac{D}{\eta}\right)^{\beta}\right) \tag{2.12}$$

Where the fitted Weibull shape and scaling parameters are: β=1.8 and η = 29.1 μm, respectively. The mean three-dimensional particle diameter is 25.9 μm. Based on the average particle diameter of 25.9 μm and the macro-scopic particle volume fraction of 0.115, the nearest neighbor distance, L_{nn}, is calculated to be 32.4 μm.

2.3.1.3 Particle area and volume fraction fluctuations

As with particle area and volume fractiona, the area and volume fraction fluctuations were assumed to be identical. The particle volume fraction fluctuation

metric, particle volume fraction COV, $COV_\phi(L)$, was observed to decrease with increasing normalized sampling size ($\frac{L}{L_{nn}}$) and an exponential function adequately describes the decay (Figure 2.4):

$$COV_\phi(L) = \left[A_\phi \exp\left(B_\phi \frac{L}{L_{nn}} \right) \right] \tag{2.13}$$

Where L is the (variable) sampling size, and L_{nn} is the nearest neighbor distance (32.4 μm). The exponential coefficients A_ϕ and B_ϕ are 1.89 and -0.59, respectively. A_ϕ, B_ϕ and L_{nn} are particle structure dependent parameters whose values are unique to NDI.

$COV_\phi(L)$ was specified in order to calculate the representative volume element (RVE) size in NDI. The standard deviation of volume fraction was set to 1% of macro-scopic volume fraction, i.e., $COV_\phi(L)$ = 0.01, where the fluctuations in the particle volume fraction are not significant. At this value, the RVE size was was $8.9L_{nn}$ (288 μm). The choice of this value for $COV_\phi(L)$ is discussed further in Section 2.4.

An analytical model for the heterogeneous second-phase particle structure in NDI was developed. A Gaussian PDF was fit to the length-scale dependent particle volume fraction using the particle volume fraction standard deviation in Equation (2.8) and the macro-scopic particle volume fraction, Φ_0:

$$P_\phi(\phi, L) = \frac{1}{S_\phi(L)\sqrt{2\pi}} \exp\left(\frac{-1}{2} \left[\frac{\phi - \Phi_0}{S_\phi(L)} \right]^2 \right) \tag{2.14}$$

Where $P_\phi(\phi, L)$ is the particle volume fraction PDF, ϕ is the (variable) local particle volume fraction at length-scale, L , and all other terms have been previously defined. Plots of Equation (2.6) at larger length-scales, i.e., $6L_{nn}$ and $8L_{nn}$, demonstrate that the probability of sampling the macro-scopic particle volume fraction also increases (Figure 2.5). In the limit as the length-scale becomes very large, $L \to \infty$, then the particle volume fraction standard deviation approaches zero, $S_\phi \to 0$. $P_\phi(\phi, L)$ essentially becomes a single-valued function since $\phi = \Phi_0$ is the only value with a non-zero probability. Alternately, the spread in $P_\phi(\phi, L)$ increases with decreases in the length-scale, i.e., $1L_{nn}$,$2L_{nn}$ and the probability of sampling the macro-scopic particle volume fraction is not substantially greater than much larger or smaller values.

2.3.2 Computer generation of representative particle structures

The particle volume fraction, size distribution, and volume fraction fluctuations were the primary inputs for generating a representative NDI-specific particle structure. Target and computer generated NDI particle structure data were compared and the error calculated with respect to the target data. While the computer generated macro-scopic particle volume fraction, Φ_0, and the particle size distribution parameters, η and β, have less than 2% error, the error particle volume fraction fluctuation parameters, A_ϕ and B_ϕ, have 6.87% and 10.17%

error, respectively (Table 2.2). Seeding of the computer generated particle structure into a RVE-scale domain is shown in Figure 2.6. In this, the graphite particles are blue and the matrix is red and transparent. While non-uniform particle size and spacing are qualitatively evident in the generated particle structure, previously stated quantitative data are required to adequately compare with target NDI-specific particle structure.

In this study, the nearest neighbor weighted clustering algorithm was utilized as part of achieving the target volume fraction fluctuations. In order to determine the necessary clustering parameters, several particle structure realizations were performed varying *α* and *A* for a fixed number (100) of algorithm iterations [Figure 2.7]. The same starting microstructure was used for each of these. As *α* and *A* are decreased from unity to nearly zero, clustering of the particle structure increases. More significant clustering is observed with decreases in *A.* The clustering algorithm parameters used to develop this computer generated NDI-specific particle structure are *A* = 0.27 and *α* = 0.05.

2.4 Discussion

The development of a mathematical description for the three-dimensional particle structure in NDI lead to the formulation of the probabilistic model in Equation (2.14) for the particle volume fraction, $P_\phi(\phi, L)$. The key parameters in $P_\phi(\phi, L)$ are the macro-scopic particle volume fraction, Φ_0, and the particle volume fraction standard deviation, $S_\phi(L)$. $S_\phi(L)$ comprises the variable (sampling) length-scale, L, as well as the particle structure parameters,

Φ_0, A_ϕ, B_ϕ and L_{nn}. These latter particle structure parameter values are unique for NDI.

The significance of these parameters is now ascertained. For small $S_\phi(L)$, the calculated $\frac{L}{L_{nn}}$ is the length-scale at which the spatial fluctuations in the particle volume fraction dissipate, i.e., particle volume fraction is homogenized. A_ϕ and B_ϕ are also significant because they provide a measure of clustering and size of clusters, through their influence on $S_\phi(L)$. For a relatively more clustered system, $S_\phi(L)$ is relatively large for a fixed (small) $\frac{L}{L_{nn}}$ and, thus, A_ϕ is large. While for a relatively uniform system, $S_\phi(L)$ is relatively small for a fixed (small) $\frac{L}{L_{nn}}$ and, thus, A_ϕ is small. Essentially, for an ensemble of (small) sampling windows, a larger dispersion in sample values are expected for a clustered system and a smaller dispersion of sample values are expected for a uniform array of particles. The average cluster size is discernable by how quickly or slowly $S_\phi(L)$ decays with increased $\frac{L}{L_{nn}}$. $S_\phi(L)$ decays relatively faster with increased $\frac{L}{L_{nn}}$, i.e., B_ϕ is a relatively large negative value, when the average cluster size is relatively small. While $S_\phi(L)$ decays relatively slower with increased $\frac{L}{L_{nn}}$, i.e., B_ϕ is a relatively small negative value, when the average cluster size is relatively large.

In light of Equation (2.14), the NDI particle volume fraction field, ϕ , can be regarded as a superposition of fluctuations onto a mean field:

$$\phi = \Phi_0 + \phi^* \tag{2.15}$$

Where ϕ^* is the particle volume fraction fluctuations and Φ_0 is the macro-scopic particle volume fraction. While Φ_0 is the integral of the local particle volume fraction over the large three-dimensional domain, it was approximated by taking the particle area fraction over the entire image montage:

$$\Phi_0 = \lim_{V\to\infty}\left[\frac{1}{V}\int \phi dV\right] \approx \frac{\sum_{i=1}^{N_{tot}} A_i}{A_{tot}} \tag{2.16}$$

In general, the fluctuating component of the particle volume fraction field is both dependent on location and length-scale over which it is measured, i.e., $\phi^*(\boldsymbol{x}, L)$. Directionality is not considered in the particle volume fraction field because the NDI second-phase particles are assumed to be isotropic. Since the second-phase particles in NDI are spatially random (spatially uncorrelated), only the length-scale dependence is explicitly considered for the fluctuating component, i.e., $\phi^*(x, L) \to \phi^*(L)$. Consistent with this notion, the multiscale sampling technique used for acquiring particle volume fraction fluctuation data did not record sample position or orientation data. These particle volume fraction fluctuation measurements form the basis of $P_\phi(\phi, L)$.

The RVE in materials with heterogeneous particle structures, such as NDI, go beyond unit cell notions. RVE size is a variable quantity based on property

measured and is much larger than characteristic material length-scales. Hill [1963] and other investigators [Hashin et al. 1962; Nemat-Nasser et al. 1999] have suggested that a RVE in realistic materials enclose a sufficiently large number of heterogeneities to adequately capture a macro-scopically uniform stress or strain response under uniform macro-scopic loading. By these qualitative definitions, it is necessary to specify an exceedingly large RVE size to attain a small COV_ϕ and, thus, a relatively uniform macro-scopic NDI response. This assumes that the NDI response correlates to the particle volume fraction. Considering Equation (2.15), as $L \to \infty$, then ϕ^* and $COV_\phi \to 0$ because $\phi \to \Phi_0$. If the user specifies COV_ϕ to be relatively small, as would be expected in a viable RVE, then the length-scale calculated from Equation (2.13) can become large. This impacts the computational resources required for RVE-scale MSS. If the user specifies COV_ϕ to be relatively large, then the calculated length-scale may not be a viable RVE, i.e., at that scale, a sufficient number of heterogeneities may not be enclosed. $COV_\phi(L)$ was specified in order to calculate the RVE size in NDI. The standard deviation of volume fraction was set to 1% of macro-scopic volume fraction, i.e., $COV_\phi(L)$ = 0.01, where the fluctuations in the particle volume fraction are not significant. The calculated RVE size is (288 μm)³ and encloses approximately 700 particles. Using a computational grid spacing of 5 μm results in a relatively feasible 200,000 element RVE-scale MSS. While a sufficient number of particles are enclosed to

ensure a relatively homogeneous stress and strain response, the domain is small enough to execute numerous RVE-scale MSS.

Numerical tools capable of generating particle structures based on their mathematical description enable MSS. In turn, MSS are used in Chapter 3 to study the effects of changing particle size and spacing distributions. Particle volume fraction, particle size distribution, and particle volume fraction fluctuations form the basis of the mathematical description. These parameters are also used as comparison metrics to determine the efficacy of these numerical tools. Better agreement is demonstrated with the particle volume fraction and the (Weibull) particle size distribution parameters, than for the particle volume fraction fluctuation parameters. The particle volume fraction fluctuation parameters do not compare as favorably because there is no explicit input for them in the numerical tools. Instead, the nearest-neighbor weighted clustering algorithm is used to control particle volume fraction fluctuations. Several open-loop iterations with the clustering algorithm are required to approximate measured NDI particle structure data. The development of a closed-loop control for the volume fraction fluctuations may minimize manual intervention, expediting the generation of representative particle structures.

2.5 Figures

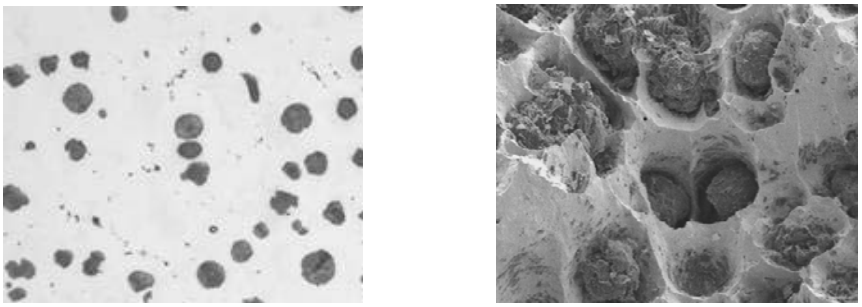

Figure 2.1: a. Nodular ductile iron (NDI) two-phase microstructure consisting of graphite particles (dark) within a contiguous clear (white) Fe-Si matrix. b. NDI fractograph demonstrating central role of graphite particles in void nucleation and ducitile fracture.

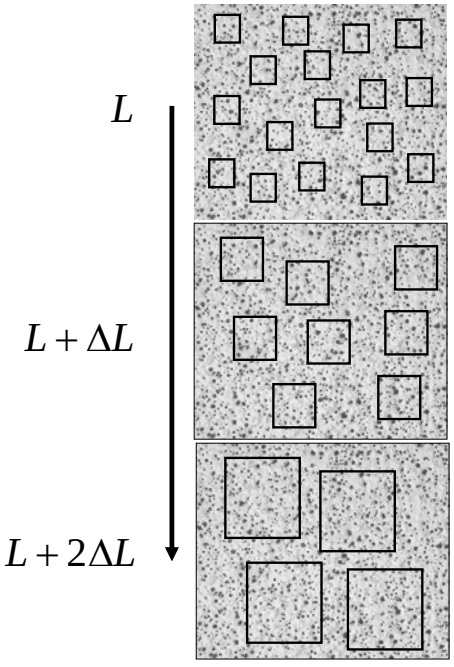

Figure 2.2: Multiscale sampling technique for determination of particle area fraction fluctuations applied to a metallographic section of undeformed NDI. Incrementally larger sampling window sizes are shown.

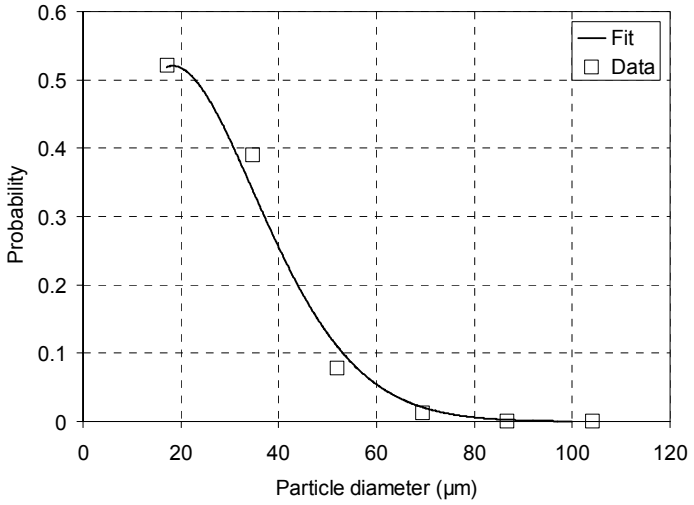

Figure 2.3: Three-dimensional particle diameter probability distribution function (PDF) plots for the binned test data and corresponding Weibull PDF fit.

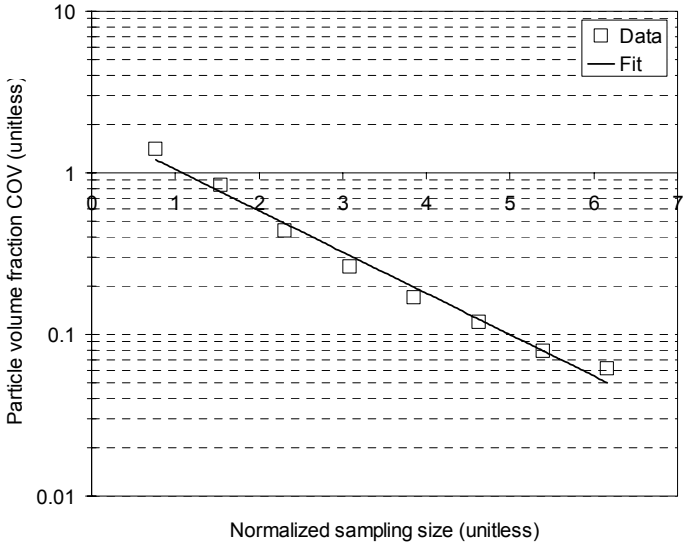

Figure 2.4: Particle volume fraction coefficient-of-variation (COV) versus normalized sampling size, $\frac{L}{L_{nn}}$. Sampling size, L, is normalized by the nearest neighbor distance, L_{nn}.

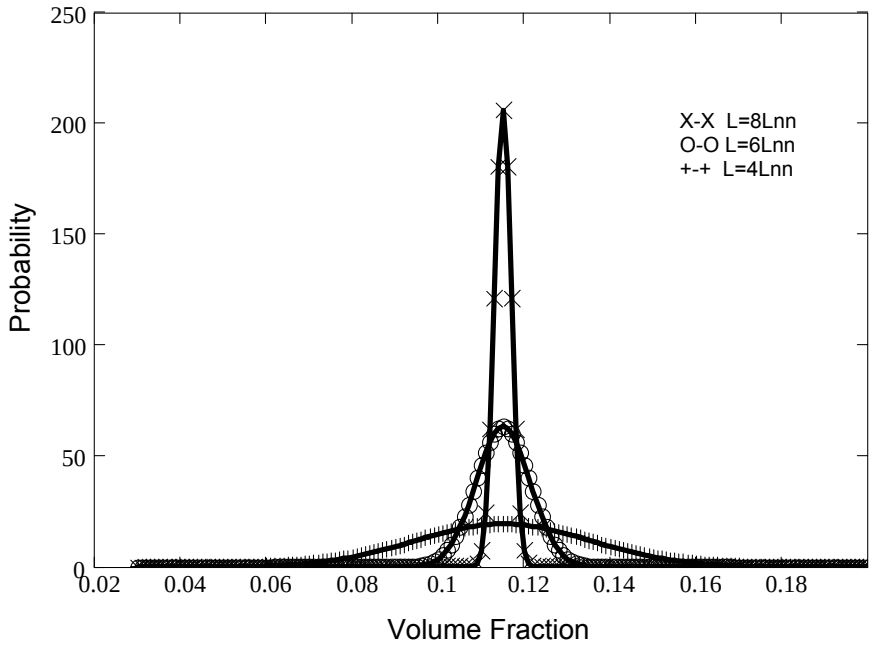

Figure 2.5: Particle volume fraction (Gaussian) PDF model plots for various length-scales demonstrating the increased distribution spread for smaller length-scales with a fixed mean.

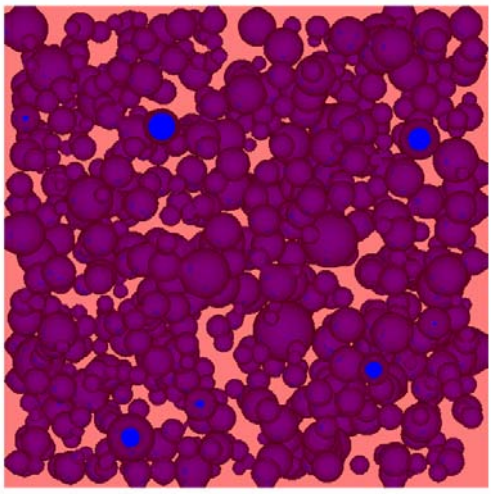

Figure 2.6: Computer generated representative particle structure for NDI in an approximately 300 μm side cube. Particle size and non-uniform spacing distribution is qualitatively observed in image.

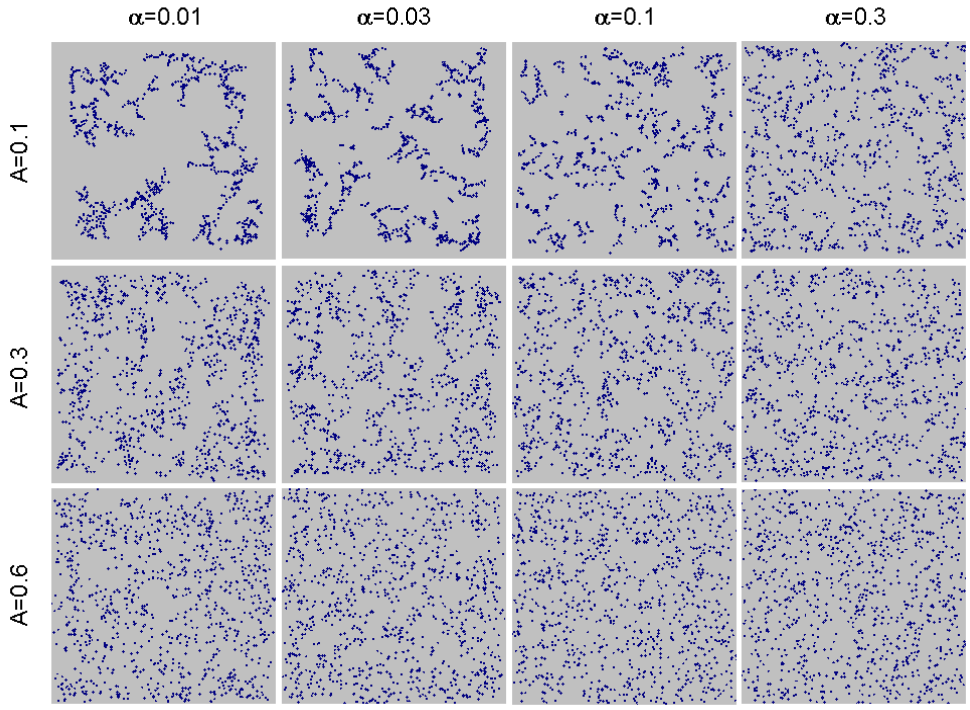

Figure 2.7: Computer generated particle structure realizations for various clustering algorithm parameters, A and α.

2.6 Tables

Element	C	Si	Mn	P	S	Cr	Mg
Weight %	3.72	2.51	0.31	0.07	0.01	<0.05	0.05

Table 2.1: NDI chemical composition

	Target NDI particle structure	Computer generated particle structure	%Error
Φ_0	0.115	0.114	0.86%
η (um)	29.1	29.3	0.69%
β	1.8	1.77	1.67%
A_ϕ	1.89	2.02	6.87%
B_ϕ	-0.59	-0.65	10.17%

Table 2.2: Target NDI and computer generated particle structure data

2.7 References

S Christy, HR Pak, MA Meyers; in *Metallurgical Applications of Shock-Wave and High-Strain-rate Phenomenon* edited by LE Murr, KP Staudhammer, MA Meyers; Dekker, New York (1986) 835

WR Clough, ME Shank; *The Flow and Fracture of Nodular Cast Iron; Trans. Am. Mech. Engrs*., 79 (1957) 1911-1920

CW Corti, P Cotterill, GA Fitzpatrick; *The Evaluation of the Interparticle Spacing in Dispersion Alloys*; International Metallurgical Reviews, 19 (1974) 77-88

Z Hashin, S Shtrikman; J. Mech. Phys. Solids, 10 (1962) 335

R Hill; Journal of the Mechanics and Physics of Solids, 11 (1963) 357-372

JH Liu, XY Hao, GL Li, GS Liu; *Microvoid evaluation of ferrite ductile iron under strain*; Materials Letters 56 (2002) 748-755

RW Minich, JU Cazamias, M Kumar, AJ Schwartz; *Effect of microstructural length scales on spall behavior of copper*; Metallurgical and Materials Transactions A, 35A (2004) 2663-2673

S Nemat-Nasser, M Hori; Micromechanics: Overall properties of heterogeneous materials; North-Holland Elsevier, 2nd Edition (1999)

J Quintanilla, S Torquato; *Local volume fraction fluctuations in random media*; J. Chem. Phys. 106:7 (1997) 2741-2751

JM Rivas, AK Zurek, WR Thissell, DL Tonks, RS Hixson; *Quantitative description of damage evolution in ductile fracture of tantalum*; Metallurgical and Materials Transactions A, 31A (2000) 845-851

SA Saltykov; Developments in Stereology, H. Elias, Ed., Proceedings of the Second International Congress for Stereology, Springer-Verlag, New York (1967) 163

Z Shan, AM Gokhale; *Representative Volume Element for Non-Uniform Microstructure*; Computational Materials Science, 24 (2002) 361-379

J Shi, MA Savas, RW Smith; *Plastic deformation of a model material containing soft spheroidal inclusions: Spheroidal graphite cast iron*; Journal of Materials Processing Technology, 133 (2003) 297-303

S Torquato; *Random Heterogeneous Materials: Microstructure and Macroscopic Properties*; Springer-Verlag (2002)

EE Underwood; *The mathematical foundations of quantitative stereology*; Stereology and Quantitative Metallography, ASTM STP 504, ASTM (1972) 3-38

S Yang, A Tewari, AM Gokhale; *Modeling of non-uniform spatial arrangement of fibers in a ceramic matrix composite*; Acta mater. 45:7 (1997) 3059-3069

3.0 Second-phase particle structure and loading effects on the ductile spall response of a model two-phase material under uniaxial strain conditions

3.1 Introduction

The primary goal of this chapter is to utilize three-dimensional meso-scale simulations (MSS) to investigate the effects of second-phase particle size and spacing distributions, loading conditions, and length-scale on the spall response of a model two-phase material. Analytical spall modeling has traditionally been focused on the dynamic growth of an isolated void under hydrostatic loading [Poritsky 1952; Carroll and Holt 1972; Johnson 1981; Ortiz and Molinari 1992; Wu et al. 2003], axisymmetric loading [Banks-Sills and Budiansky 1982], and general loading triaxialities [Cortes 1992; Wang 1994]. These analytical models have provided valuable insights, demonstrating the influence of void volume fraction, void size, load amplitude and duration, inertia, temperature, as well as strain and strain-rate hardening, on the micromechanisms of ductile spall failure. However, isolated void growth models tend to overpredict the material spall resistance because they do not account for the influence of neighboring voids.

Two-dimensional MSS have demonstrated the influence of void clustering on spall failure [Benson 1993; Tonks et al. 1995; Tonks 1996]. Since these previous studies were based on plane strain analyses without representative material mesostructures, they did not rigorously capture the complex, three-dimensional interactions that occur during the spall process.

In heterogeneous materials, more pronounced spatial variations in *microscale* spall response are expected. Only recently have studies focused on this phenomenon. Vogler and Clayton [2007] employed two-dimensional MSS in an effort to model experimentally measured variations in the pull-back signal of shocked tungsten heavy alloy. The pull-back signal is derived from the free surface velocity measurements and is a metric of the spall strength. Measured spatial variations in the spall strength metrics were attributed to the heterogeneous nature of this material. While their predicted spall strength variations were qualitatively similar to experimental measurements, the physical domain size of the simulation is believed to contribute to quantitative differences. These results suggest that the physical domain size of the simulation is important and needs to be considered in any new studies of the spatial variability in spall fracture.

The Carroll and Holt [1972] (hereafter the *CH model*) and Johnson [1981] models of isolated void growth behavior demonstrated that the critical stress logarithmically decreases with increasing void volume fraction. The applicability of these analytical models to three-dimensional void growth and coalescence will be determined. MSS will be used to explore the effects of *void volume fraction* and *loading conditions* on spall response of a generic two-phase material.

Analytical models of Poritsky [1952], Ortiz and Molinari [1992], and Wu et al. [2003] demonstrate that at larger void radii, inertia effects are much more pronounced and tend to suppress void growth. However, these models cannot assess the added influence of neighboring voids on void growth and

coalescence. MSS will be used to explore the effects of *void size* on the spall response of a generic two-phase material.

While Vogler and Clayton [2007] showed that spatial variations in spall strength are influenced by material meso-structure, the effects of the physical domain size of the simulation (hereafter *physical domain size*) on these variations, though, were not examined. Material response is expected to homogenize with increased physical domain size based on general notions of representative volume elements (RVEs) [Hill 1963; Hashin et al. 1962; Nemat-Nasser et al. 1999]. MSS will be used to explore the effects of physical domain size on the variations in spall response of the model material, nodular ductile iron (NDI).

3.2 Methods

3.2.1 Meso-scale simulation (MSS) description

Meso-scale simulations (MSS) were used to explore the effects of particle volume fraction, particle radius, as well as applied load magnitude, ramp-time, and loading rate on the material spall response. MSS geometry, boundary conditions and measurements, particle structure generation, component phase material models, and finite element analysis code are described below.

3.2.1.1 Geometry

MSS geometry was designed to permit impulsive loading through void coalescence, prevention of end-effects from interfering with void growth and coalescence, attainment of uniaxial strain conditions, and a representative sampling of the second-phase particle structure.

The approach of Benson [1993] was adopted in this study to satisfy the impulsive loading and end-effects requirements. The second-phase particle region was a subset of larger simulation geometry and staggered from the loading plane, rather than coincident with it, to prevent artificial spall at the loading plane. Surrounding this particle region on either side were matrix phase regions. The simulation geometry was then extended in length downstream of the particle region to prevent the tensile pulse from reflecting at the free surface, propagating back to particle region, and interfering with void growth and coalescence.

In order to study three-dimensional second-phase particle structure, Benson's [1993] two-dimensional, rectangular-strip geometry was "extruded" in the third dimension. This resulted in a prismatic bar, i.e., a long bar with a square cross-section. The particle region was a (subset) cube region within the larger prismatic bar geometry and offset from the loading plane. The lateral extent of the prismatic bar and, thus, particle region was dependent on the particle size and spacing statistics.

A uniaxial strain boundary condition, typically associated with impact-driven shock and spall experiments, was used in these simulations. Uniaxial strain conditions were achieved by designating all lateral faces of the prismatic bar geometry to be symmetry planes.

Figure 3.1 depicts the prismatic bar geometry, the subset particle region, the extended matrix region downstream of particle region, and the designation of

symmetry planes. The prismatic bar geometry had an approximately 300 μm by 300 μm cross-section and was 3000 μm long.

3.2.1.2 Applied loading and measurement of transmitted stress

The applied tensile stress, $\sigma(t)$, and the spall strength metric were qualitatively identical to the approach in Benson [1993]. As shown in Figure 3.1, $\sigma(t)$ was applied normal to an end face of the MSS prismatic bar closest to the particle region. The loading consisted of a finite ramp-time, t_{ramp}, to a constant (maximum) value of stress, σ_0.The loading rate, $\dot{\sigma}$, and t_{ramp} are related by

$$\dot{\sigma} = \frac{\sigma_0}{t_{ramp}} \tag{3.1}$$

Loading rate was modified by either changing the t_{ramp} or σ_0. But the duration of this loading rate was set by t_{ramp}, after which it thresholded at σ_0.

Downstream of the particle region, the transmitted stress time-history in the longitudinal direction was tracked. The peak transmitted stress was used as the spall strength metric (SSM) for this study because it is a measure of the ultimate load capacity of the prismatic bar.

3.2.1.3 Particle structure

Several second-phase graphite particle structure realizations were generated using computational tools developed in Chapter 2. The initial macro-scopic particle volume fraction, Φ_0, and the initial particle radius, r_0, were modified between realizations. Generic particle structures were generated

assuming a uniform particle size distribution and random particle spacing. The number of particles in a given realization was dependent on the particle region volume in the prismatic bar, r_0, and Φ_0.

3.2.1.4 Finite element analysis code

Simulations were performed using LLNL's three-dimensional arbitrary-Lagrange-Eulerian (ALE) code, ALE3D [Nichols 2007]. ALE3D was used for these simulations because it permits seeding of the void nucleating particles across mesh lines, it handles large deformations of the matrix material around the growing void while still capturing the void-matrix interface, and it permits void coalescence as it culminates to spall fracture. Neither a lagrangian-only or eulerian-only code can adequately simulate these material behaviors. MSS had approximately five million elements with an element size of 5 μm in the particle region. Elements were spatially graded outside of the particle region to improve computational efficiency.

3.2.1.5 Component phase material models

Elasticity, yield surface, hardening, equation-of-state (EOS), and failure models were separately specified for the Fe-Si alloy matrix and graphite particle phases. Model parameters were determined from a combination of experiments and literature.

3.2.1.5.1 Elasticity model

An isotropic elasticity model was used for both the Fe-Si alloy matrix and the graphite particles. As is common in finite element analysis (FEA) codes that handle large pressures, the hydrostatic and deviatoric response is treated

separately. A separate EOS model is utilized for the hydrostatic response of the material. Therefore, the isotropic elasticity is only applicable for the deviatoric component of the elastic response,

$$\sigma_{ij}^{/} = 2\mu\varepsilon_{ij}^{el'} \tag{3.2}$$

Where $\sigma_{ij}^{/}$ is the deviatoric stress, μ is the shear modulus, and $\varepsilon_{ij}^{el'}$ is the deviatoric, elastic strain. Only the shear modulus is specified for this model.

3.2.1.5.2 Yield surface model

The J_2 flow (yield surface) model is used to model the inelastic response of the Fe-Si alloy matrix and the graphite particles. The flow potential, φ , is typically expressed as an inequality:

$$\varphi = Y\left(\varepsilon_{eq}\right) - \sigma_{eq} \leq 0 \tag{3.3}$$

At the core of this model is the scalar von Mises stress based on deviatoric stress,

$$\sigma_{eq} = \sqrt{\frac{3}{2}\sigma_{ij}^{/}\sigma_{ij}^{/}} \tag{3.4}$$

and the material strain and strain-rate hardening response, $Y\left(\varepsilon_{eq}, \dot{\varepsilon}_{eq}\right)$. The scalar equivalent plastic strain (EPS), ε_{eq}, is given by:

$$\varepsilon_{eq} = \sqrt{\frac{2}{3}\varepsilon_{ij}^{pl}\varepsilon_{ij}^{pl}} \tag{3.5}$$

Where ε_{ij}^{pl} is the plastic strain tensor.

3.2.1.5.3 Hardening models

The strain-rate dependent Johnson-Cook strength model [Johnson and Cook 1985] was used for the Fe-Si alloy matrix and an elastic-perfectly plastic model was used for the graphite particles. It has been shown that strain-rate can influence spall strength [e.g., Ortiz and Molinari 1992]. The Johnson-Cook model has the form:

$$Y\left(\varepsilon_{eq},\dot{\varepsilon}_{eq}\right)=\left(A+B\varepsilon_{eq}^{n}\right)\left(1+C\ln\left(\frac{\dot{\varepsilon}_{eq}}{\dot{\varepsilon}_{0}}\right)\right)\left(1-\left(\frac{T-T_{room}}{T_{melt}-T_{room}}\right)^{m}\right) \tag{3.6}$$

Where A,B are strain-hardening coefficients, n is the strain hardening exponent, ε_{eq} is the current EPS, C is the strain-rate hardening coefficient, $\dot{\varepsilon}_0$ is the reference strain-rate, $\dot{\varepsilon}_{eq}$ is the current EPS rate, T_{room} is the room (reference) temperature, T_{melt} is the melt temperature, m is the temperature exponent, and T is the current temperature. Quasistatic and Hopkinson bar compression data were used to parameterize this model for the Fe-Si alloy. The Johnson-Cook model parameters and the shear modulus for the Fe-Si alloy are shown in Table 3.1. The graphite elastic-plastic perfectly parameters are shown in Table 3.2. The temperature dependence was disabled in these studies by setting T_{melt} to $10^5 K$ and m to unity.

3.2.1.5.4 Equation-of-state (EOS) model

Under shock compression, an isothermal (elastic) bulk modulus can no longer accurately describe the material pressure-volume relationship and an

EOS model is needed [Duval et al. 1963]. A prevalent EOS form for materials is the Gruneisen model:

$$P = \begin{cases} \dfrac{\rho_0 c^2 \mu \left[1 + \left(1 - \dfrac{\gamma_0}{2}\right)\mu - \left(\dfrac{a}{2}\right)\mu^2\right]}{\left[1 - (S_1 - 1)\mu - S_2\left(\dfrac{\mu^2}{\mu+1}\right) - S_3\left(\dfrac{\mu^3}{(\mu+1)^2}\right)\right]^2} + (\gamma_0 + a\mu)E, \text{ for } \mu > 0 \\ \rho_0 c^2 \mu + (\gamma_0 + a\mu)E, \text{ for } \mu < 0 \end{cases} \quad (3.7)$$

Where P is the pressure, $\mu \left(= \dfrac{\rho_0}{\rho} - 1\right)$ is the volumetric compression, ρ_0, ρ are the initial and current densities, c is the y-intercept of the shock velocity-particle velocity fit (approximately the sound-speed), γ_0 is the Gruneisen coefficient, a is the linear correction to the Gruneisen (gamma) coefficient, S_i are the shock velocity-particle velocity polynomial coefficients, and E is the internal energy. The Gruneisen model was used for both the Fe-Si alloy matrix and the graphite particles. EOS parameters for the graphite particles were taken from Steinberg [1996]. Since EOS parameters did not exist for the Fe-Si alloy, those for a low carbon steel were used [Steinberg 1996]. The Gruneisen EOS model parameters for the Fe-Si alloy and graphite are given in Tables 3.3 and 3.4, respectively.

3.2.1.5.5 Failure models

At the microscopic level, spall fracture is characterized by the rapid nucleation, growth and coalescence of voids in a narrow band. Voids nucleate at inclusions, second-phase particles, grain boundaries or other microstructural features. Voids grow under tensile loading and coalesce via impingement or localized strain bands. In the current study, void nucleation at the graphite

particles and void coalescence via intervoid matrix shear were modeled by applying material failure criteria.

Void nucleation was modeled by applying a hydrostatic-pressure based criterion to the graphite material in the MSS. A relatively small value of hydrostatic tension was used (10 MPa) since graphite particles were assumed to be loosely bound to the matrix material. This value is less than 1% of the lowest applied load magnitude (2 GPa). Void nucleation is effectively induced in the graphite particles whenever hydrostatic tension is encountered. After nucleation occurred, the pressure and deviatoric stress were zeroed in the particle (now void) region. In this study, the term “particles” refers to the initial graphite particles and the term “voids” refers to the region after nucleation by hydrostatic tension.

Void coalescence via intervoid shear was modeled by applying an equivalent plastic strain (EPS) criterion to the matrix materials in the MSS. This EPS criterion (0.4) was pressure-independent because the void and matrix phases are treated as separate and distinct regions in current simulations. Continuum-scale strain-based ductile failure models have pressure-dependence primarily because the void and matrix phases are homogenized [Hancock and MacKenzie 1976; Johnson and Cook 1985] and pressure affects the micromechanisms of ductile fracture. Pressure-dependence would only be relevant in MMS if the matrix phase had a much smaller (sized) void population in it that facilitated coalescence, i.e., void-sheeting [Cox et al. 1974]. Void-sheeting has not been observed in NDI fracture.

Since mesh sensitivity associated with material softening and failure is well documented [Bazant 1976; Bazant and Belytschko 1985], a limited study investigating the effects of mesh size (2, 4, 5, 10 μm) on the SSM were conducted. These were performed on the MSS configuration shown in Figure 3.1. For this study, an applied load magnitude of 2 GPa, ramp-time of 0.05 μs, initial macro-scopic particle volume fraction of 11.5%, and initial radius of 13 μm was used.

3.2.2 Generic two-phase material MSS

Initial RVE-scale MSS studies of the generic two-phase material explored the effects of initial macro-scopic particle volume fraction, Φ_0 (1%, 5%, 11.5%, 15%) on the peak transmitted stress, i.e., the SSM, for differing applied load magnitudes, σ_0 (2, 4, 6, 8 GPa). The load ramp-time, t_{ramp} (0.050 μs), and the initial particle radius, r_0 (13 μm) were fixed in these studies. These studies provide baseline comparison metrics to existing analytical models, especially the CH model.

Additional studies investigated the effects of load ramp-up, t_{ramp} (0, 0.05, 0.5 μs) for various Φ_0 (5%, 11.5%) and σ_0 (2, 4, 6 GPa) on the SSM. r_0 was fixed at 13 μm. The purpose of these studies is to determine if the increased t_{ramp}, in conjunction with changes to Φ_0 and σ_0, can accelerate the material void growth and alter the SSM.

The effects of r_0 (1, 13, 50 μm) and σ_0 (2, 4, 6 GPa) on the SSM were also explored. In these studies, Φ_0 (5 %) and t_{ramp} (0.5 μs) were fixed. The

purpose of these studies is to determine if SSM response is dominated by inertia effects at larger particle sizes or if loading or interaction effects come into play during void growth and coalescence.

The effects of load rate, $\dot{\sigma}$ (6, 12, 24, 60, 120 GPa/ μs) on void growth rate, $\dot{\Phi}$, and SSM were also investigated. The σ_0 (6 GPa), Φ_0 (5 %), and r (13 μm) were fixed. The purpose of these studies is to directly determine if changes to $\dot{\sigma}$ correlate to changes in $\dot{\Phi}$ and, thus, SSM. This study complements the previously described t_{ramp} study by more narrowly focusing on the effects of $\dot{\sigma}$, but with a fixed σ_0.

3.2.3 NDI-specific sub-scale MSS

NDI-specific studies explored the effects of MSS physical domain size (100, 300 μm) on the spatial variations of the SSM. σ_0 (2 GPa), t_{ramp} (0.05 μs), Φ_0 (11.5%) and r_0 (13 μm) were fixed. The latter two particle structure data is specific to NDI. The objective of this study was to quantify the changes in spatial variation with changes to the physical domain size. The metric used to quantify variations was the SSM coefficient-of-variation (COV), which is the ratio of the SSM standard deviation to the SSM mean value.

Particle structure for the NDI-specific MSS were extracted from a single, master realization. Rather than re-creating realizations for each of the sixty simulations, a master realization was randomly (spatially) sampled. Thirty samples were taken each at the 100 and 300 μm physical domain sizes. Each sample of microstructure became the particle structure used for one simulation. Thirty (30) simulations were conducted for each physical domain size in order to

ensure statistical significance of the variations of peak transmitted stress. The master realization was that of the largest direct numerical simulation in Chapter 4. At a 4000 μm diameter by 2000 μm thickness, the master realization provided ample volume from which to sample for these simulations.

3.3 Results

3.3.1 The effects of initial volume fraction and applied load magnitude

Figure 3.2 demonstrates the MMS-predicted effects of initial particle volume fraction, Φ_0 (1%, 5%, 11.5%, 15%), on the spall strength metric (SSM) for different applied load magnitudes, σ_0 (2, 4, 6, 8 GPa). For constant σ_0, the SSM decreases with increasing Φ_0, being linear in $\ln(\phi)$. For constant Φ_0, the SSM decreased with increasing σ_0. This was more pronounced at lower Φ_0 (1%, 5%) and lower σ_0. At a 15% particle volume fraction, though, there was less then 0.03 GPa (5% of SSM) change in SSM for σ_0 from 4 to 8 GPa. At a 1% volume fraction and σ_0 of 2 GPa, there was no apparent spall detected in the simulation and, thus, no peak transmitted stress was observed.

Carroll-Holt [1972] model (CH model) and Johnson [1981] model results are also plotted for comparison. For these models, the initial void volume fraction is assumed to be equal to the initial particle volume fraction, Φ_0. This assumption is consistent with the modeling of void nucleation in MSS, whereby the loosely bound graphite particles are assumed to nucleate voids at a hydrostatic tension

value of less than 1% of the lowest applied load magnitude. It is remarkable how well the CH model, a model based on an isolated and spherical void, compares with the MSS results for lower σ_0. This agreement motivated the selection of the CH model as the framework for the new model described in Section 3.3.5.

3.3.2 The effects of load ramp-time

Figures 3.3, 3.4, and 3.5 demonstrate the effects of Φ_0 (5%, 11.5%) on the SSM for different load ramp-up (0, 0.05, 0.5 μs) and σ_0 (2, 4, 6 GPa). For σ_0 of 6 GPa (Figure 3.5), there was nearly 0.25 GPa (25% of SSM) difference in the SSM between 0 μs and 0.5 μs ramp-time. For σ_0 of 2 GPa (Figure 3.3), there was a 0.025 GPa (<2.5% of SSM) change with t_{ramp} and the SSM value at Φ_0 of 5% and 11.5% were approximately 1.0 and 0.7 GPa, respectively. Furthermore, it was observed that the SSM values for the higher σ_0 (4, 6 GPa) at higher Φ_0 (5%, 11.5%) for the 0.5 μs ramp-time are also approximately 1.0 and 0.7 GPa, respectively. The similarity of the SSM for the lowest σ_0 for all t_{ramp} (Figure 3.3) and the higher σ_0 at the longest t_{ramp} (Figure 3.4 and 3.5) is notable, and will be discussed later, in Section 3.4.

The void volume growth rates, $\dot{\Phi}$, for the upper (6 GPa) and lower (2 GPa) applied load bounds, t_{ramp} from 0 to 0.5 μs, and a Φ_0 of 5% are shown in Figure 3.6. For σ_0 of 6 GPa, the peak $\dot{\Phi}$ is 4.5 and 2.5 μs^{-1} for t_{ramp} of 0 and 0.5 μs, respectively. The longer t_{ramp} tends to reduce the void growth rate at a σ_0 of 6 GPa. For σ_0 of 2 GPa, the peak $\dot{\Phi}$ is 1.75 and 1.85 μs^{-1} for t_{ramp} of 0 and 0.5 μs,

respectively. As the peak $\dot{\Phi}$ increased, the SSM decreased. The SSM is 0.75 and 1.01 for peak $\dot{\Phi}$ of 4.47 μs^{-1} (maximum) and 1.73 μs^{-1} (minimum).

3.3.3 The effects of initial particle radius and applied load magnitude

Figure 3.7 demonstrates the effect of the initial particle radius r_0 (1, 13, 50 μm) on the SSM for different σ_0 (2, 4, 6 GPa). SSM decreased for increasing r_0 with a log-linear relationship The effects of r_0 were less pronounced for σ_0 of 2 GPa, where the SSM dropped 0.05 GPa (<5% of SSM) for r_0 from 1 to 50 μm, than for σ_0 of 6 GPa, where the SSM dropped 0.14 GPa (<15% of SSM) for r_0 from 1 to 50 μm. For fixed r_0, the SSM decreased with increasing σ_0. For example, for r_0 equal to 1 μm, the SSM was 1.07, 0.97, and 0.9 GPa for σ_0 of 2, 4, and 6 GPa, respectively. For r_0 equal to 50 μm, the SSM was 1.02, 0.84, and 0.76 GPa for σ_0 of 2, 4, and 6 GPa, respectively. Since inertia has been shown to have a more significant effect at larger r_0 (for fixed Φ_0 and σ_0), these results were unexpected and will be discussed later in Section 3.4.

While the SSM decreased for increasing r_0, the peak $\dot{\Phi}$ did not increase for decreasing SSM, as was described in the latter portion of Section 3.3.2. The realization that the transit time of an elastic wave at velocity, c_0, across a nucleated void with radius, r_0, affects incremental load across the void led to the utilization of a normalized time (discussed further in Section 3.4):

$$t_{norm} = \frac{t}{\left(r_0 / c_0 \right)} \tag{3.8}$$

A normalized void growth rate, $\dot{\Phi}_{norm}$ (unitless), was then defined. It is the incremental void growth, $d\phi$, divided by the increment in normalized time, dt_{norm}. Figure 3.8 shows $\dot{\Phi}_{norm}$ as a function of t_{norm}. For σ_0 of 2 GPa, $\dot{\Phi}_{norm}$ for the 50 μm radius ($3.70\text{x}10^{-3}$) is approximately 250% of that for the 1 μm radius ($1.40\text{x}10^{-3}$). For σ_0 of 6 GPa, $\dot{\Phi}_{norm}$ for the 50 μm radius ($1.07\text{x}10^{-2}$) is approximately 200% of that for the 1 μm radius ($5.34\text{x}10^{-3}$). Maximum $\dot{\Phi}_{norm}$ ($1.07\text{x}10^{-2}$) was found for the 6 GPa applied load and 50 μm radius, and the minimum $\dot{\Phi}_{norm}$ ($1.40\text{x}10^{-3}$) was found for σ_0 of 2 GPa and 1 μm radius. As in Section 3.3.2, the maximum $\dot{\Phi}_{norm}$ leads to the minimum SSM (0.76 GPa) and the minimum $\dot{\Phi}_{norm}$ leads to the maximum SSM (1.07 GPa).

3.3.4 The effects of load rate

Figures 3.9 and 3.10 demonstrate the effects of load rate, $\dot{\sigma}$ (6, 12, 24, 60, 120 GPa/ μs) on the time-history of $\dot{\Phi}$ and the peak $\dot{\Phi}$. The peak $\dot{\Phi}$ of 3.2 μs^{-1} (120 GPa/μs) was 215% larger than the peak $\dot{\Phi}$ of 1.49 μs^{-1} (6 GPa/μs). The peak $\dot{\Phi}$ decreased for decreasing $\dot{\sigma}$ but reached a floor value at approximately 1.5 μs^{-1}. In fact, a linear relationship was found between the peak $\dot{\Phi}$ and the $\dot{\sigma}$ (Figure 3.10).

Figure 3.11 demonstrates the linear increase in SSM with decreasing $\dot{\sigma}$ to a maximum SSM of approximately 1.0 GPa.This reinforces the trends in Figures

3.3 to 3.6 that longer ramp-times, and thus smaller loading rates, tend to have larger SSM up to a maximum value that is relatively insensitive to $\dot{\sigma}$. Altogether, Figure 3.11 demonstrates that increasing $\dot{\sigma}$ beyond a threshold value (~24 GPa/μs) tends to increase the peak $\dot{\Phi}$, and decrease the SSM.

Figure 3.12 illustrates the qualitative differences in the void growth and coalescence at loading rates of 120 and 12 GPa/μs. The transverse view of the MSS particle region is shown. The tensile loading wave approaches the particle region from the right side. The particles have been subdivided into ten color coordinated regions in the loading direction to better track void recruitment downstream (to the left). Void growth occurs sooner in the 120 GPa/μs case than in the 12 GPa/μs case primarily because, at a fixed time, the load in the higher loading rate case is higher (up to the maximum of 6 GPa). Of course, the wave transit time needs to be accounted for in these cases, as well, since the particle region is offset from the loading plane. Based on an offset of 300 μm and a wave-speed of 3980 μm/ μs, the time offset is 0.075 μs. At a simulation time of 0.15 μs (adjusted time of 0.075 μs), the load has reached 0.9 GPa in the 12 GPa/μs case and thresholded at 6.0 GPa in the 120 GPa/μs case. At a simulation time of 0.40 μs (adjusted time of 0.325 μs), the load has reached 3.9 GPa in the 12 GPa/μs case and remains thresholded at 6.0 GPa in the 120 GPa/μs case. At this time, the voids have nearly coalesced in the 120 GPa/μs case while they have grown significantly in the 12 GPa/μs case. By the simulation time of 0.55 μs (adjusted time of 0.475 μs), the void coalescence has occurred in both cases. While void growth in the 12 GPa/μs case involves four

color (subdivided) regions (red, green, blue, and turquoise), void growth in the 120 GPa/μs case only involves two color (subdivided) regions (blue and turquoise). This suggests that at lower loading rates, relatively more downstream voids are recruited in the coalescence process. This is a significant result that will be discussed later in Section 3.4.

3.3.5 Carroll-Holt (CH) model modification

Based on the foregoing MSS results, the CH model was modified to capture the additional effects of $\dot{\sigma}$ and r_0. Figures 3.13 and 3.14 depict the construction of this model. Figure 3.13 is an altered version of Figure 3.2 that showcases the key effect to be captured, i.e., the change in SSM-Φ slope with loading. Figure 3.14 demonstrates the influence of loading rate on the SSM-Φ slope, which is separated into two load rate regimes: the subcritical regime and the supercritical regime. The resulting modified CH model has the form:

$$\sigma_{spall} = -m\left(Y,\dot{\sigma}_{norm}\right)\left[\ln\left(\Phi_0\right)-\ln\left(\Phi_{off}\right)\right]+\sigma_{spall,off} \tag{3.9}$$

$$m\left(Y,\dot{\sigma}_{norm}\right)=\begin{cases}\dfrac{2}{3}Y, & \dot{\sigma}_{norm}<\dot{\sigma}_{norm,crit}\\ A\ln(\dot{\sigma}_{norm})+B, & \dot{\sigma}_{norm}>\dot{\sigma}_{norm,crit}\end{cases} \tag{3.10}$$

$$\dot{\sigma}_{norm}=\frac{d\sigma}{dt_{norm}}=\dot{\sigma}\left(r_0 \Big/ c_0\right) \tag{3.11}$$

Where $m\left(Y,\dot{\sigma}_{norm}\right)$ is the SSM-Φ slope and is a function of the yield strength, Y, and the normalized loading rate, $\dot{\sigma}_{norm}$. $\dot{\sigma}_{norm}$ is a function of the loading rate, $\dot{\sigma}$, the initial void radius, r_0, and the matrix material sound speed, c_0. The coefficients A, B are -0.0838 and 0.1842, respectively. The volume fraction offset, Φ_{off}, was 27.6% and the load offset, $\sigma_{spall,off}$, (based on Φ_{off}) was 0.395

GPa. Figure 3.14 is used to determine the critical loading rate, i.e., the loading rate between the subcritical and supercritical regimes (0.13 GPa- no time unit since normalized). In this subcritical regime ($\dot{\sigma}_{norm}$ ≤ 0.13 GPa), $m\left(Y,\dot{\sigma}_{norm}\right)$ is $\frac{2Y}{3}$. In the supercritical regime ($\dot{\sigma}_{norm}$ > 0.13 GPa), $m\left(Y,\dot{\sigma}_{norm}\right)$ becomes a function of the normalized loading rate, $A\ \ln(\dot{\sigma}_{norm})+B$. The subcritical and supercritical regimes are discussed futher in Section 3.4.

Figure 3.15 depicts the comparison of Figure 3.2 results for σ_0 of 2 and 8 GPa with modified CH model in Equation (3.9). For σ_0 of 2 GPa, $\dot{\sigma}_{norm}$ < 0.13 GPa (no time units since normalized) and, therefore, $m\left(Y,\dot{\sigma}_{norm}\right)$ is set to $\frac{2Y}{3}$ in the modified CH model for comparisons to Figure 3.2 results. This is the lower bound case for the loading rate. For σ_0 of 8 GPa, $\dot{\sigma}_{norm}$ > 0.13 GPa and, therefore, $m\left(Y,\dot{\sigma}_{norm}\right)$ is set to $A\ \ln(\dot{\sigma}_{norm})+B$ in the modified CH model for comparisons to Figure 3.2 results. This is the upper bound case for the loading rate. Good agreement is demonstrated for these bounding cases, verifying the implementation of the CH model modification since it was partially based on Figure 3.2.

3.3.6 The effects of length-scale on NDI-specific SSM variations

Figure 3.16 depicts the SSM histogram resulting from the thirty (30) simulations performed at each the 300 and 100 μm physical domain sizes. The SSM histogram consists of 10 bins, ranging from a minimum SSM of 0.456 GPa to a maximum SSM of 1.094 GPa. This results in a bin size of 0.064 GPa. There

are significantly larger SSM variations at the 100 μm physical domain size than with the 300 μm physical domain size. The mean and standard deviation are 0.802 and 0.027 GPa for the 300 μm physical domain size and 0.778 and 0.166 GPa for the 100 μm physical domain size.

Figure 3.17 demonstrates the effects of the normalized physical domain size, $\frac{L}{L_{nn}}$, on the SSM coefficient-of-variation (COV) for the MSS at each physical domain size (100 or 300 μm). Where L is the MSS physical domain size and L_{nn} is the nearest-neighbor distance. The COV is the ratio of the standard deviation to mean value. Each MMS data point in Figure 3.17 represents predictions from thirty simulations. Model data in Figure 3.17 is discussed below in Section 3.3.7. For the MSS predictions, the SSM COV decreases from 0.25 at $\frac{L}{L_{nn}}$ of 3.0 to 0.035 at $\frac{L}{L_{nn}}$ of 7.75. Extrapolation of model data out to a SSM COV of 0.01, which was used in Chapter 2 to determine the effective RVE size based on the particle volume fraction, leads to $\frac{L}{L_{nn}}$ of approximately 10.5.

3.3.7 Incorporation of NDI-specific particle volume fraction model with modified CH model

In order to account for SSM variations due to MSS physical domain size, Equation (3.9) was integrated with the NDI specific probabilistic particle volume fraction model, $P_{\phi}(\phi, L)$, from Chapter 2:

$$P_{\phi}(\phi, L) = \frac{1}{S_{\phi}(L)\sqrt{2\pi}} \exp\left(\frac{-1}{2} \left[\frac{\phi - \Phi_0}{S_{\phi}(L)} \right]^2 \right) \tag{3.12}$$

$$S_{\phi}(L) = \Phi_0 \left[A_{\phi} \exp\left(B_{\phi} \frac{L}{L_{nn}} \right) \right] \tag{3.13}$$

Where Φ_0 = 0.115, A_{ϕ} =1.89, B_{ϕ} = -0.58, and L_{nn} = 32.4 μm and these parameters are discussed in Chapter 2. In order to generate results with this model, $\frac{L}{L_{nn}}$ was fixed in Equation (3.13), and then it was substituted into Equation (3.12). For each fixed $\frac{L}{L_{nn}}$, ten thousand particle volume fraction samples were taken from $P_{\phi}(\phi, L)$. Each particle volume fraction sample was input to the modified CH model in Equation (3.9) to calculate the SSM. A SSM COV value was calculated and reported at each $\frac{L}{L_{nn}}$. The SSM COV versus $\frac{L}{L_{nn}}$ is shown in Figure 3.17. For the model, the SSM COV exponentially decreases from 0.9 at a $\frac{L}{L_{nn}}$ of 1.0 to 0.015 at a $\frac{L}{L_{nn}}$ of 8.0. Extrapolation of model data out to a SSM COV of 0.01, which was used in Chapter 2 to determine the effective RVE size, leads to a $\frac{L}{L_{nn}}$ of approximately 9. This contrasts with the larger value (10.5) predicted by the MSS.

3.3.8 Mesh sensitivities

Figure 3.18 shows the effects of mesh size on SSM. For mesh sizes of 10, 5, 4, and 2 μm, the SSM is 0.709, 0.739, 0.745, and 0.751 GPa, respectively.

With respect to the 2 μm case, the SSM of the 10, 5, and 4 μm cases differ by 5.67%, 1.68%, and 0.83%, respectively. While the SSM difference appears to decrease with decreasing mesh size for these particular simulations, mesh sensitivities associated with material failure are still considered to be a source of uncertainty for the suite of MMS-based studies in this chapter and will be discussed further in Section 3.4.

3.4 Discussion

While the MSS capture the three-dimensional nature of the void interactions, they are remarkably consistent with the isolated (spherical) void models of Carroll-Holt [1972] and Johnson [1981] in the lower loading rate ($\dot{\sigma}$) regimes. Small differences at a fixed, lower loading rate can be attributed to the initialization of MSS with non-uniform particle structures. Several studies have shown that materials with non-uniform void distributions tend to concentrate stress and strain [Ohno et al. 1984; Becker 1987; Huang et al. 1993], and more rapidly fracture [Magnusen et al. 1988] than those with uniform void distributions. This bolsters the need for representative, three-dimensional particle size and spacing distributions in MSS.

While the predicted SSM is nearly independent of applied load conditions at lower $\dot{\sigma}$, loading dependencies are observed at higher $\dot{\sigma}$. This is conveyed in Figure 3.11, where the SSM is shown to be a linear function of $\dot{\sigma}$ beyond a critical threshold value. Figure 3.12 qualitatively demonstrates the effects of $\dot{\sigma}$ on void growth and coalescence. At higher $\dot{\sigma}$, void growth and coalescence is relatively more spatially localized. The voids tend to interact and coalesce with

other voids that encounter the stress wave at nearly the same time. Whereas at lower $\dot{\sigma}$, void growth and coalescence is relatively more spatially diffused. In this case, the voids tend to interact with nearest-neighbors or even the nearest cluster and more momentum, as evidenced by void growth, is transmitted downstream. Benson [1993] also found the peak transmitted stress to be relatively independent of applied loading. However, they did not observe SSM dependence on loading conditions likely because they did not consider higher $\dot{\sigma}$.

Lower $\dot{\sigma}$ can be regarded as a "quasistatic" limit, or subcritical regime loading rate, for the SSM. In this regime, the SSM is independent of loading, which is analogous to, but not identical to, observations in actual quasi-static tests. The higher $\dot{\sigma}$ can be regarded as being in the supercritical regime [Wu et al. 2003]. In the supercritical loading regime, the increased $\dot{\Phi}$ reduces momentum transfer downstream of the spall plane prior to void coalescence and, thus, the transmitted stress decreases. This is evidenced by the trends showing increased void growth rate, $\dot{\Phi}$, with increasing $\dot{\sigma}$ (Figure 3.9), as well as the relatively more localized growth and coalescence of voids for higher $\dot{\sigma}$ (Figure 3.12).

The logarithmic decrease in SSM for increasing r_0 contrasts with previous model predictions of the inhibiting effects of inertia and the limiting velocity of materials under tension (i.e., elastic wave speed). Analytical models have confirmed that inertia retards the growth of voids [Poritsky 1952; Ortiz and Molinari 1992; Wang 1997; Wu et al. 2003]. Using Equation (1.1) in Chapter 1, Antoun et al. [2003] showed that for r_0 up to 10 μm, there are no significant

inertia effects. For r_0 greater than 50 μm, however, inertia effects are much more pronounced and can impede void growth. The elastic wave speed limitation on void growth has not been thoroughly examined, but such limitations have been reviewed in the context of dynamic crack growth [e.g., Meyers 1994]. Studies within a hollow sphere construct (Appendix B) suggest that material sound-speed limitations would be significant for Φ_0 less than 1% and r_0 greater than 25 μm. Since these values are not within the parameter space considered in this work, sound-speed limitations are not expected to play a significant role in the void growth mechanisms.

A possible explanation for the decreased SSM for larger r is the interaction of loading time-scales, e.g., t_{ramp}, with the void transit time, t_{trans}. For a fixed t_{ramp} or $\dot{\sigma}$, the load increment over the smaller void is relatively small in comparison to the larger void due to the smaller t_{trans}. While $\dot{\sigma}$ at the scale of the smaller void appears relatively "slow" (i.e., subcritical regime, $\dot{\sigma}_{norm} < \dot{\sigma}_{norm,crit}$), $\dot{\sigma}$ at the scale of the larger void appears relatively "fast" (i.e., supercritical regime, $\dot{\sigma}_{norm} > \dot{\sigma}_{norm,crit}$). This results in a larger $\dot{\Phi}_{norm}$ (Figure 3.8) and lower SSM (Figure 3.7). For the 6 GPa applied load case in Section 3.3.3, SSM decreased 0.14 GPa (<15% of SSM) and $\dot{\Phi}_{norm}$ increased approximately 200% for r_0 from 1 to 50 μm. Void size effects were incorporated in the modification of the CH model.

The NDI-specific probabilistic particle volume fraction model in Equation (3.12) was incorporated into the modified CH model for the purpose of predicting small-scale variations in spall strength. The form of the CH model, with explicit

dependence on Φ_0, simplified this process. Model predicted SSM variations are a direct result of the multi-scale, probabilistic nature of Equation (3.12). At small physical domain sizes, there is a large variation in the initial, small-scale particle volume fraction ϕ_0 that feeds the modified CH model. So, SSM variations are reflected in ϕ_0 variations. Satisfactory agreement was demonstrated between the modified CH model and the MSS results for the SSM COV versus $\frac{L}{L_{nn}}$ and the extrapolated RVE size. This suggests that detailed microstructural information can enhance the predictive capability of spall models.

Despite the relatively positive results of the mesh size studies, mesh sensitivities are considered a source of uncertainty in the larger suite of MSS studies. Mesh sensitivities associated with material softening and failure has been clearly demonstrated in previous studies [Bazant 1976; Bazant and Belytschko 1985]. In dynamic simulations where the material in a mesh element softens or fails, the tangential stiffness becomes negative and the wave speed can become imaginary. The problem can change from hyperbolic to elliptic and becomes ill posed. This inevitably leads to spurious localization of damage into a zone of zero volume and convergence with mesh refinement is no longer assured [Bazant 1976].

The non-local integral approach offers one possibility of eliminating mesh sensitivities in finite element analysis while using microstructural information. The non-local integral approach consists of replacing a certain variable with its non-local counterpart obtained by weighted averaging over a spatial neighborhood of

each point under consideration [Bazant et al. 2002; Tvergaard et al. 1995]. The spatial neighborhood is determined by applying a characteristic length scale. Microstructurally-based length-scales that are characteristic of material softening or failure response can serve in this capacity. For the studies in this chapter, the average particle size or the particle nearest-neighbor distance may serve as relevant characteristic length-scales since they participate in the void growth and coalescence process. The application of non-local integral approaches to future MSS-based spall studies appears promising.

While spall results from the intersection of tensile release waves created by the reflection of initial (shock) compressive stress waves at a free surface, only tensile loading was considered in the current study. It has been shown that the initial shock compression can cause phase transformations [Meyers et al. 1992], strain-hardening [Asay et al. 1993], and yield stress alteration upon compression-tension load reversal, i.e., Bauschinger effect [Cochran and Banner, 1977; Asay et al. 1993]. Phase transformations have been shown to play an important role in the spall behavior of iron alloys, influencing the fracture mode and the spall strength [Meyers et al. 1992]. Shock-induced hardening, in conjunction with a reduced tensile yield stress due to the Bauschinger effect, can significantly increase the initial strain in the specimen prior to tensile loading. It is recommended that future MSS-based studies incorporate initial compressive loading to explore phase transformation, shock-hardening, and the Bauschinger effects on spall fracture response.

3.5 Figures

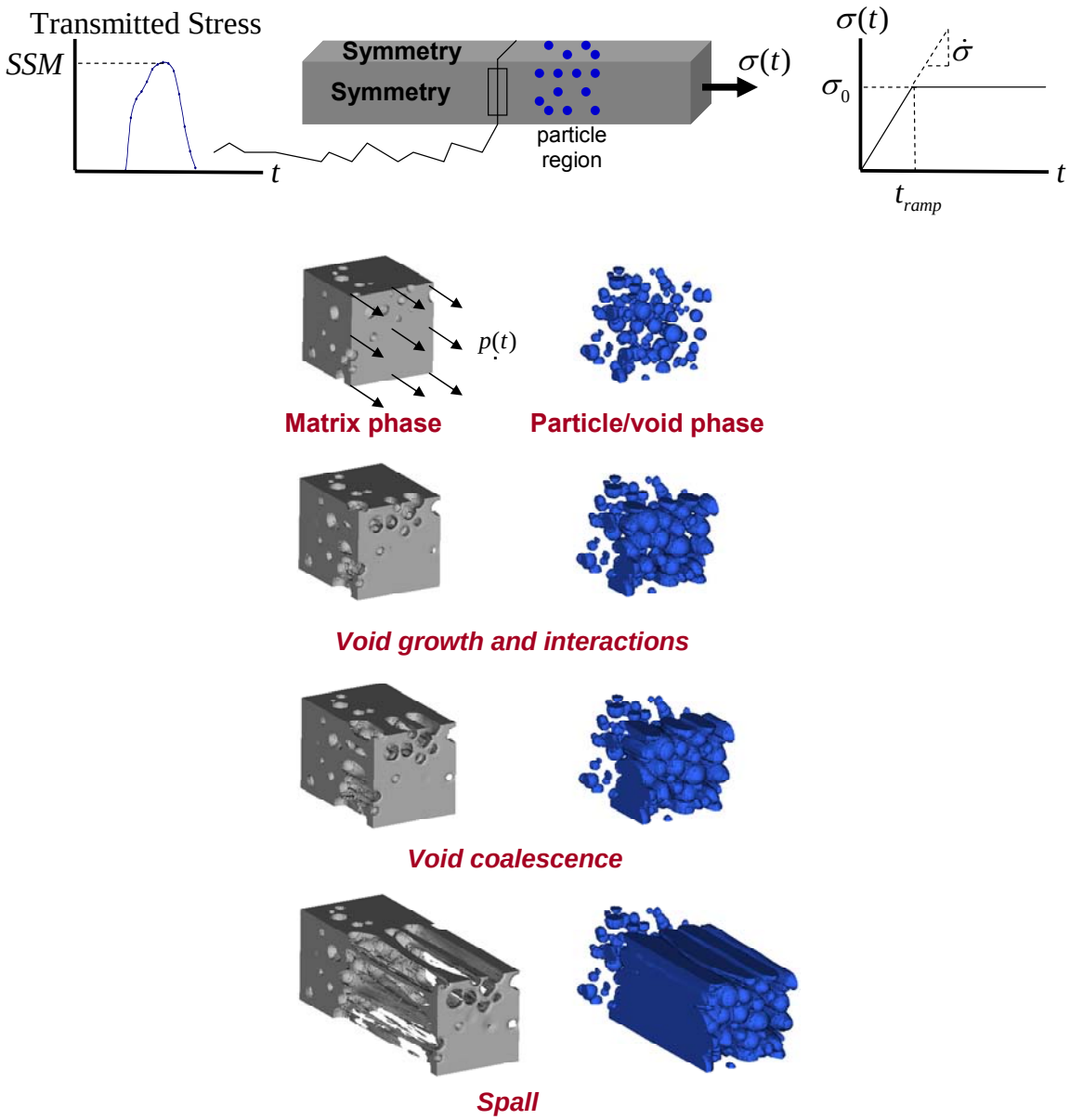

Figure 3.1: Meso-scale simulation (MSS) setup, including applied loading conditions, isolated particle region, symmetry constraints, and peak transmitted stress measurement. MSS progression depicting the culmination of void growth and coalescence to spall. Only the MSS particle region is shown.

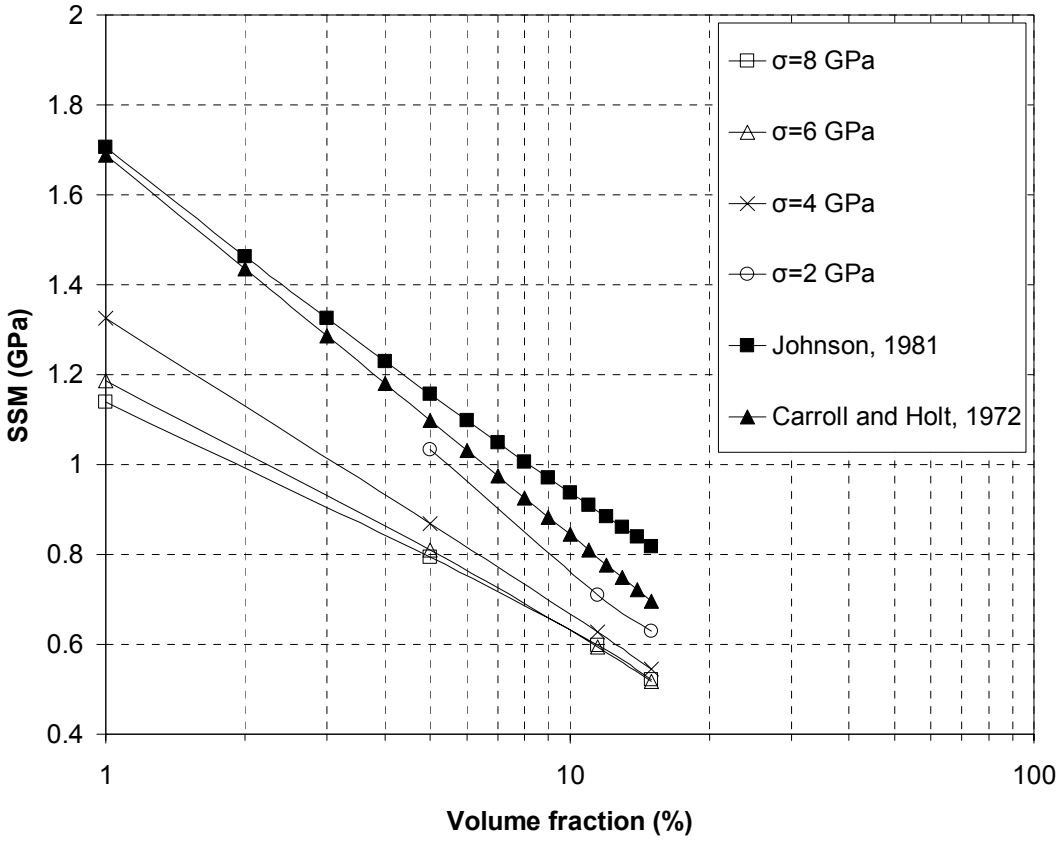

Figure 3.2: Spall strength metric (SSM), i.e., peak transmitted stress, versus initial macro-scopic particle volume fraction for applied loading (σ_0) of 2, 4, 6, 8 GPa.

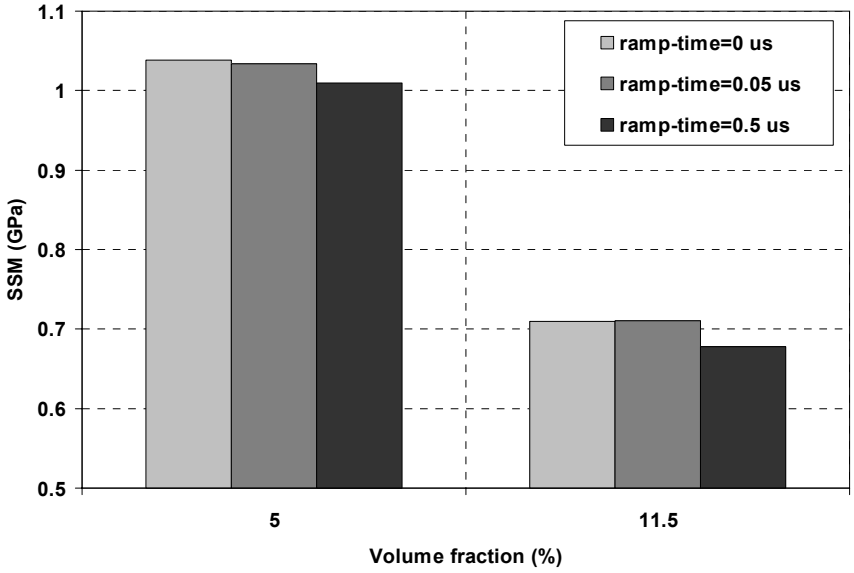

Figure 3.3: SSM for initial macro-scopic particle volume fraction of 5, 11.5% and ramp-time of 0, 0.05, 0.5 μs and σ_0 of 2 GPa

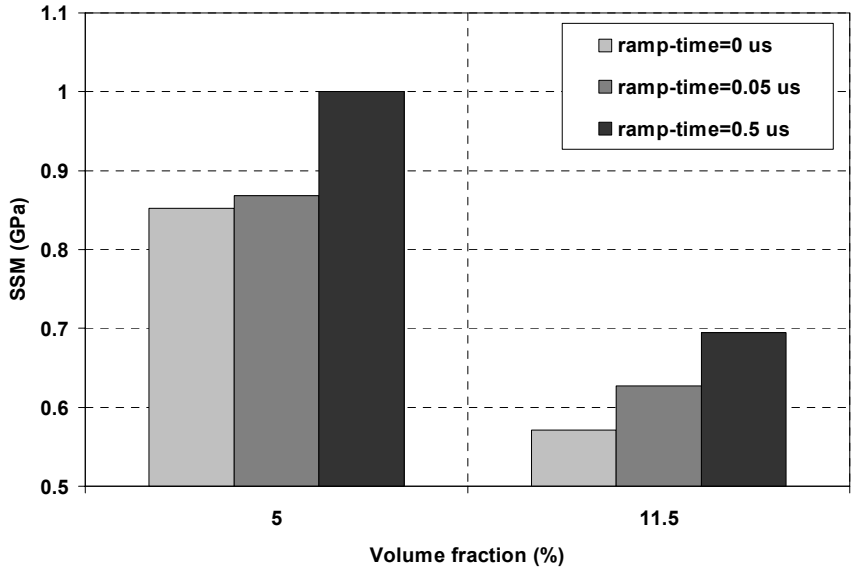

Figure 3.4: SSM for initial macro-scopic particle volume fraction of 5, 11.5% and ramp-time of 0, 0.05, 0.5 μs and σ_0 of 4 GPa

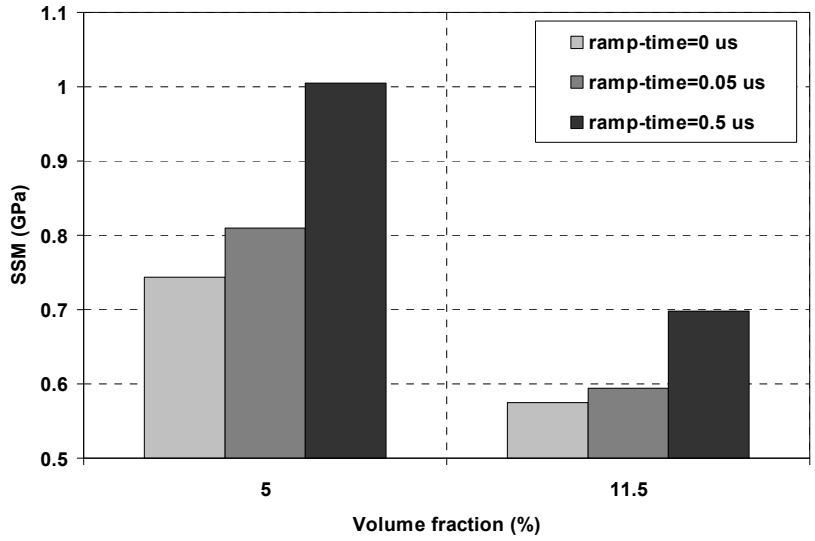

Figure 3.5: SSM for initial macro-scopic particle volume fraction of 5, 11.5% and ramp-time of 0, 0.05, 0.5 μs and σ_0 of 6 GPa

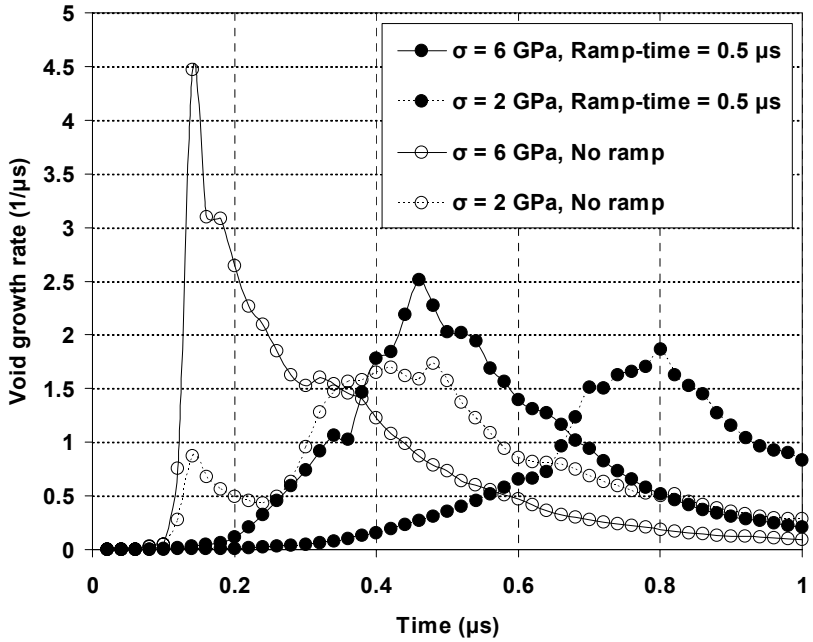

Figure 3.6: Void growth rate versus time, for ramp-time of 0 and 0.5 μs and σ_0 of 2, 6 GPa

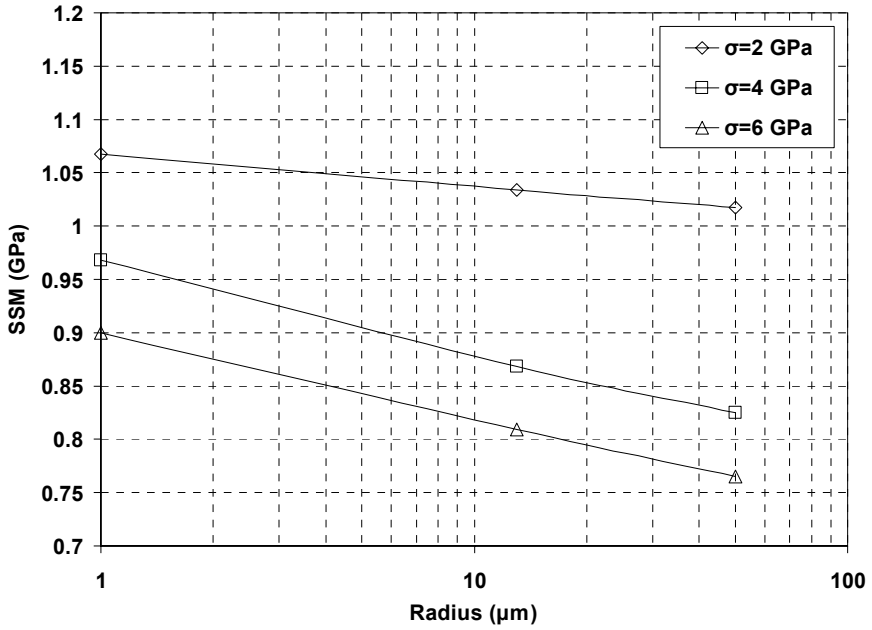

Figure 3.7: SSM versus initial particle radius for σ_0 of 2, 4, 6 GPa

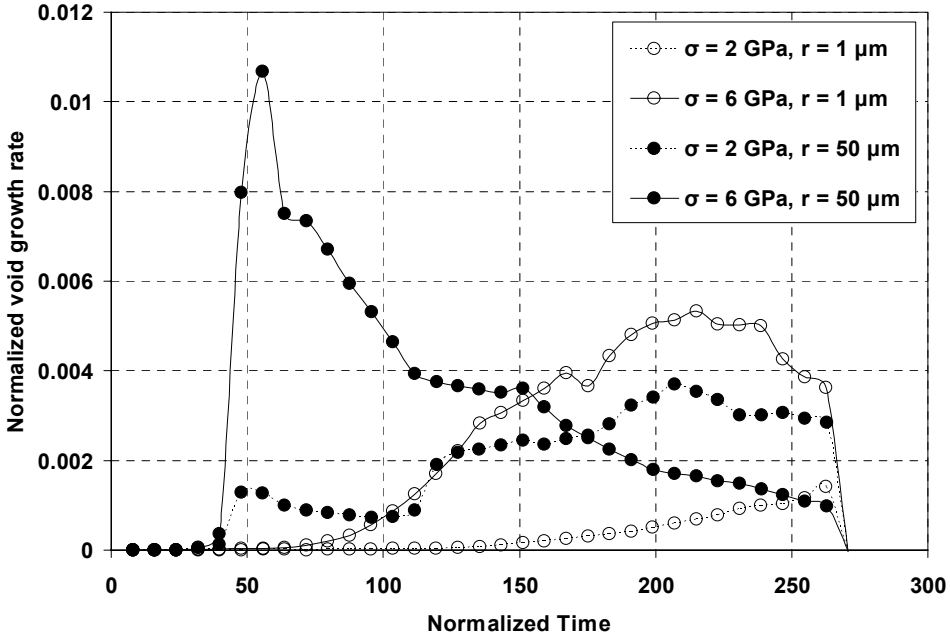

Figure 3.8: Normalized void growth rate versus normalized time for initial particle radius of 1, 5 μm, and σ_0 of 2, 6 GPa

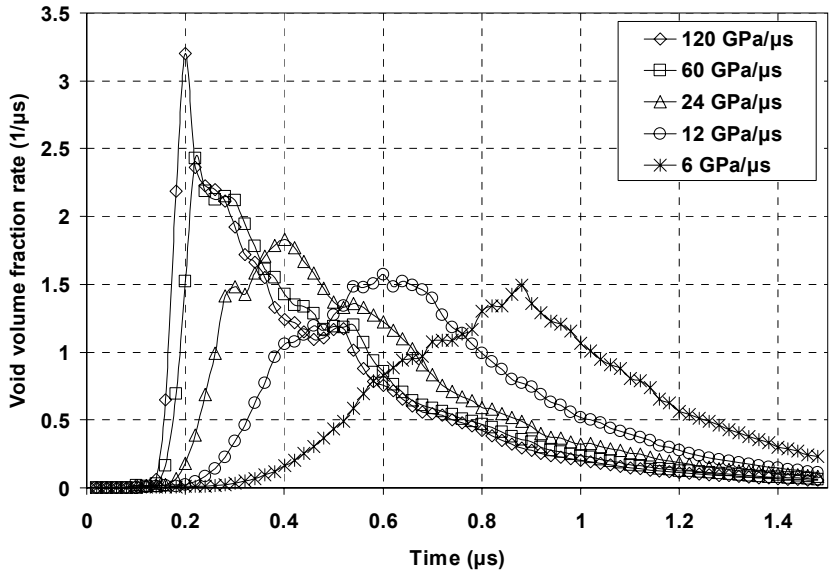

Figure 3.9: Void growth rate versus time, for applied loading rates of 6, 12, 24, 60 and 120 GPa/μs

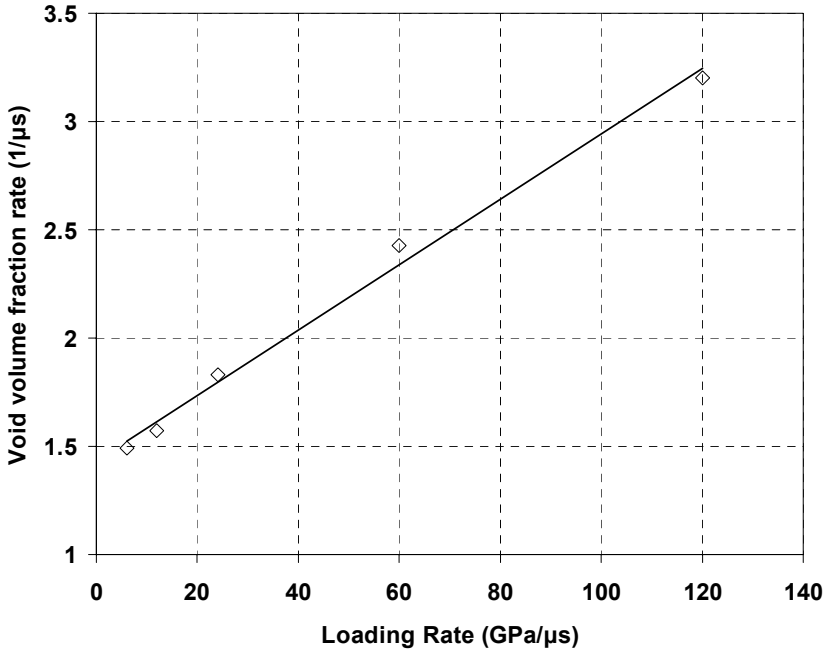

Figure 3.10: Applied loading rates versus peak void growth rate.

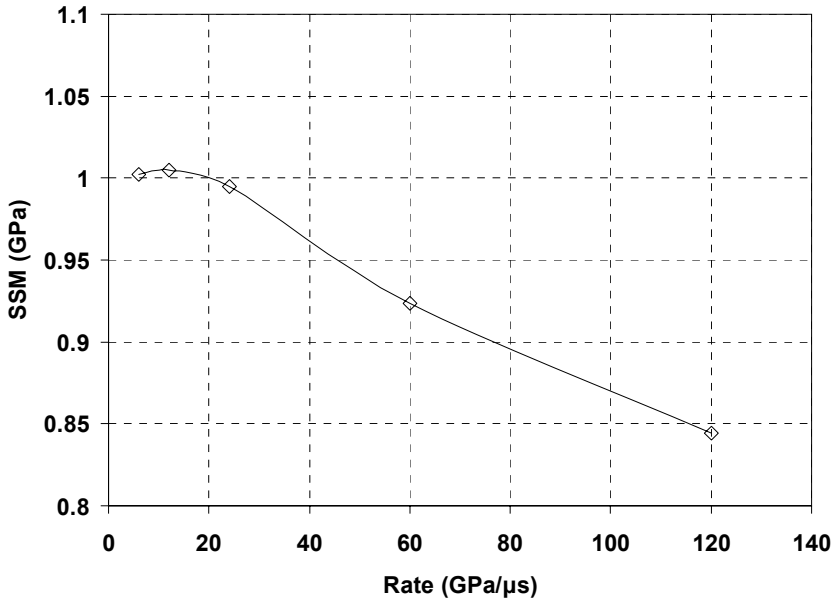

Figure 3.11: SSM versus applied loading rates for σ_0 of 6 GPa

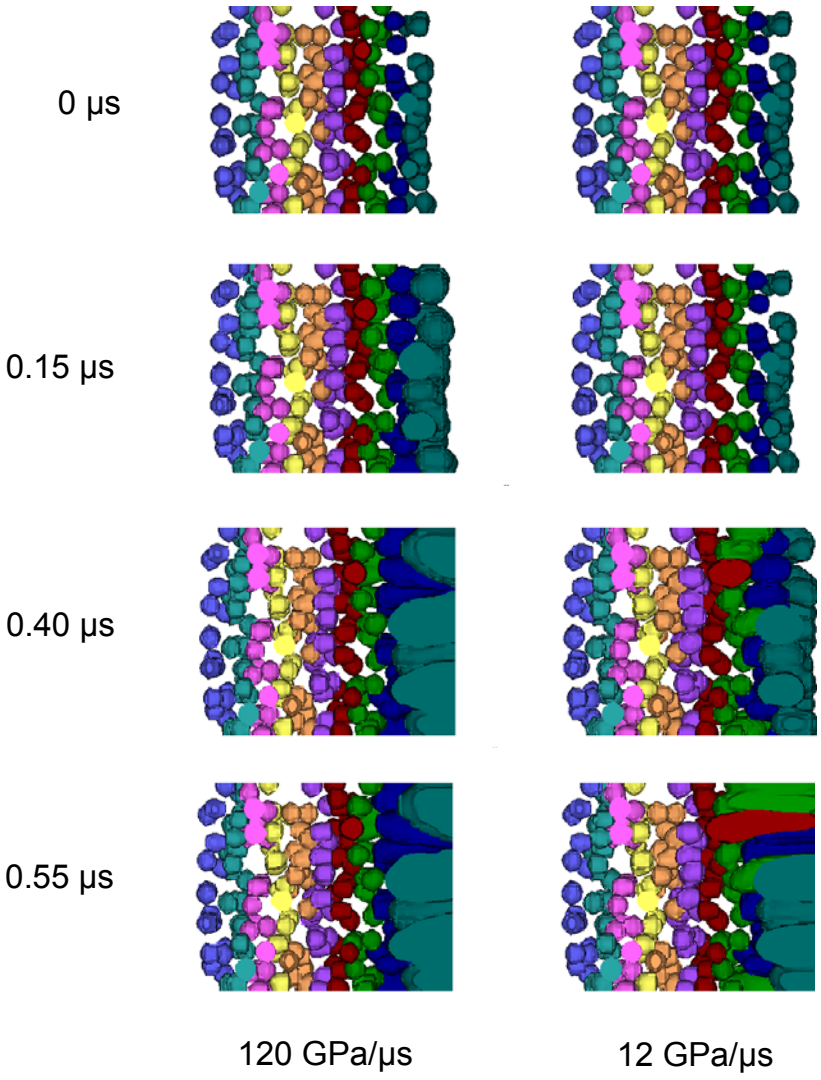

Figure 3.12: The comparison of void growth and coalescence at loading rates of 120 and 12 GPa/μs. The transverse view of the MSS particle region is shown (without matrix). The tensile loading wave approaches the particle region from the right side. The particles have been subdivided into ten color coordinated regions in the loading direction to better track void recruitment downstream (to the left).

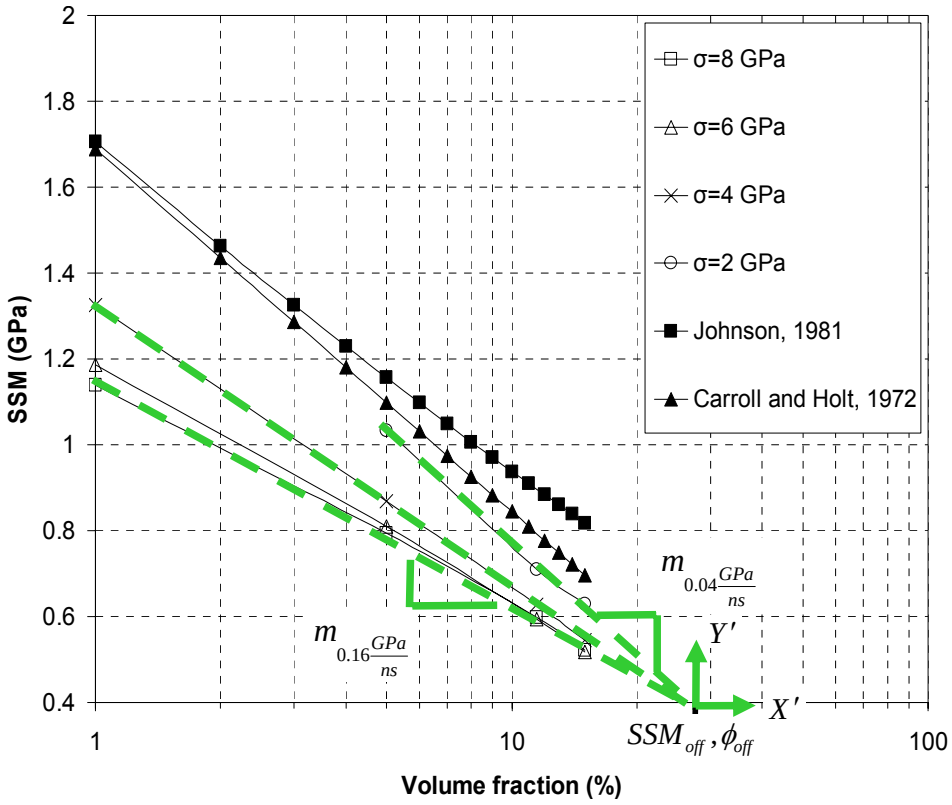

Figure 3.13: Determination of the slope (*m*) of the SSM versus particle volume fraction curves, as part of the construction of the modified Carroll-Holt model. The green dashed lines represent fits to the MSS results.

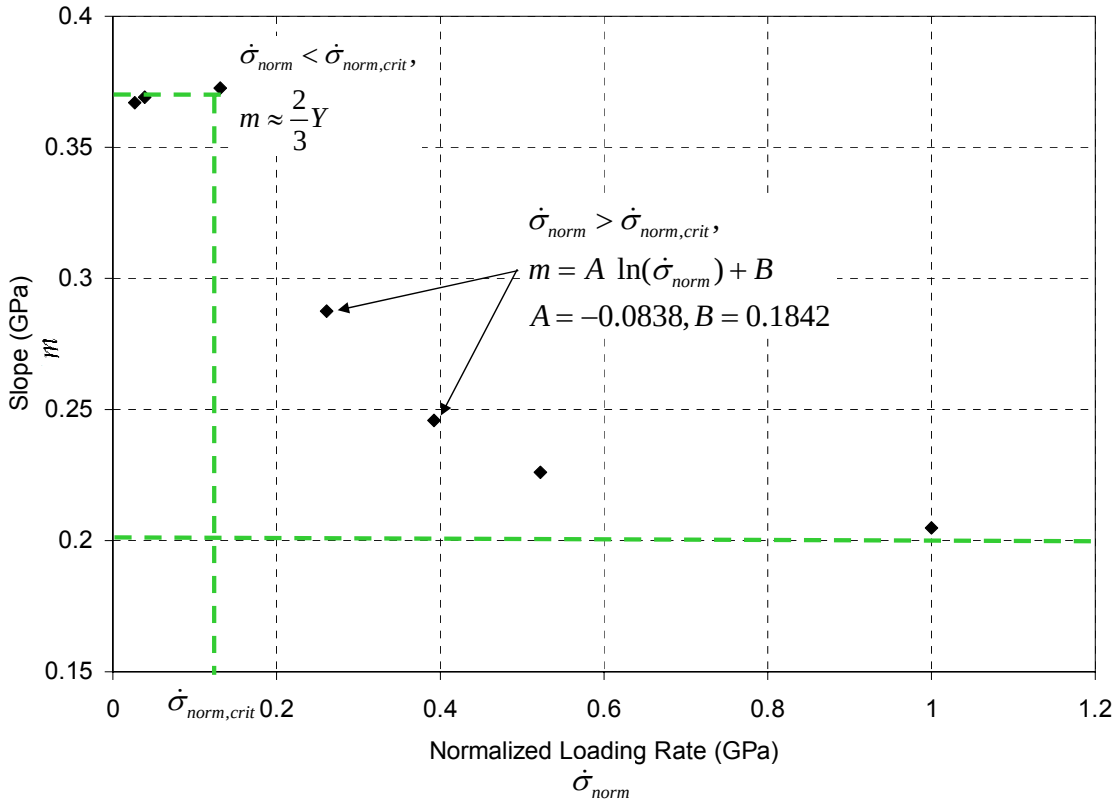

Figure 3.14: Determination of the slope (*m*) of the SSM versus particle volume fraction curves as a function of normalized loading rate ($\dot{\sigma}_{norm}$). The data in this plot is taken from Figure 3.13. In the subcritical regime ($\dot{\sigma}_{norm} < \dot{\sigma}_{norm,crit}$), the slope is constant. In the supercritical regime ($\dot{\sigma}_{norm} > \dot{\sigma}_{norm,crit}$), the slope is a logarithmic function of the normalized loading rate.

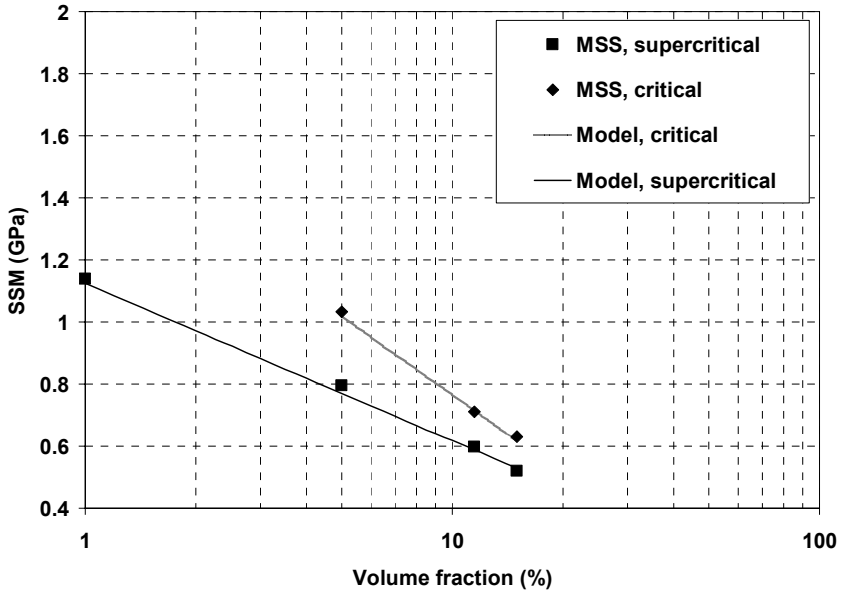

Figure 3.15: Comparison of Figure 3.2 results for applied loads of 2, 8 GPa with modified CH model in Equation (3.9)

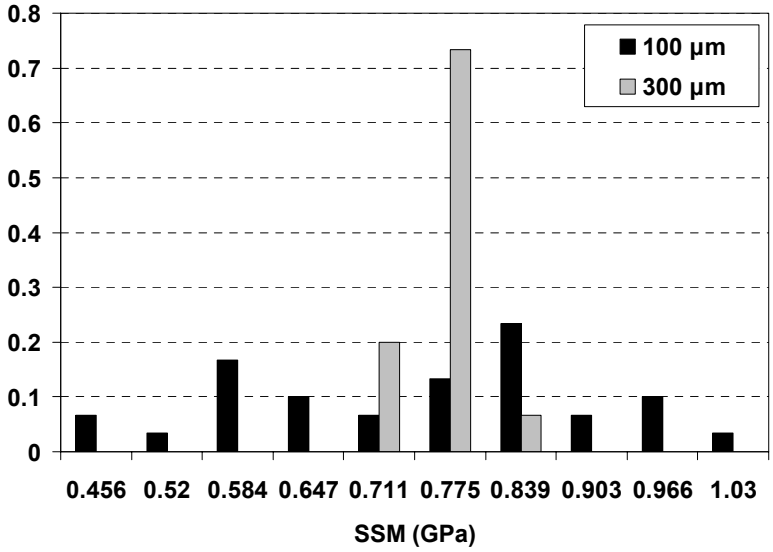

Figure 3.16: SSM histogram for simulations with length-scales of 100 and 300 µm

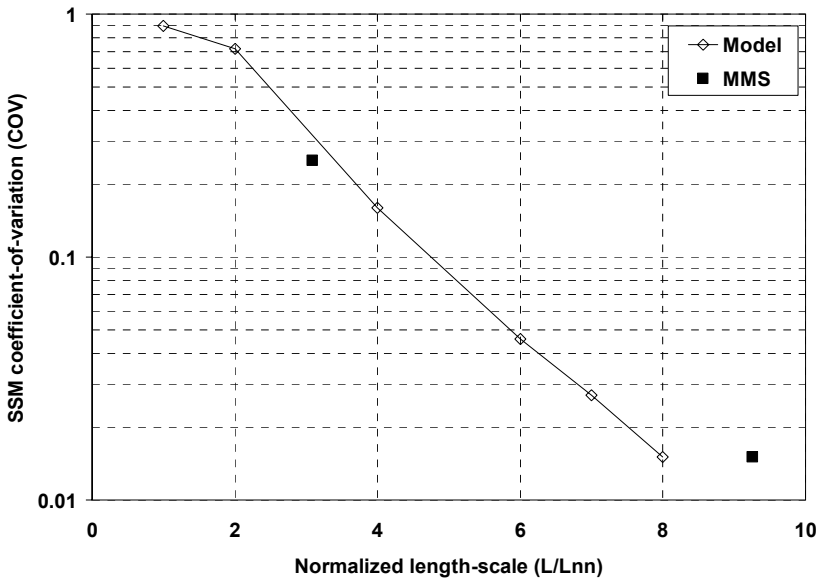

Figure 3.17: SSM COV versus normalized length-scale for MMS and model predictions

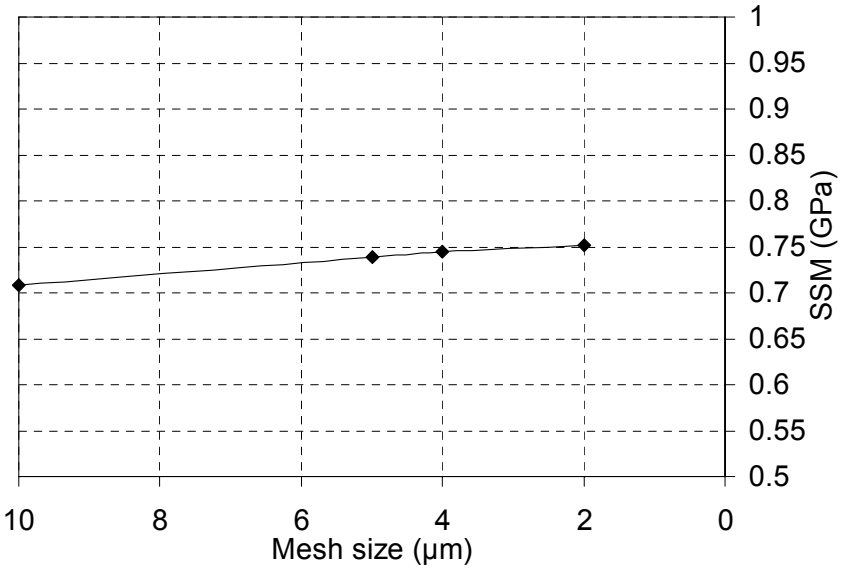

Figure 3.18: The effects of mesh size (2, 4, 5, 10 μm) on the SSM for an applied load of 2 GPa, initial particle volume fraction of 11.5%, and initial particle size of 13 μm.

3.6 Tables

μ (GPa)	A (MPa)	B (MPa)	n (none)	C (none)	$\dot{\varepsilon}_0$ (1/s)	T_{melt} (K)	m (none)
69.0	345	550	0.43	0.023	0.001	100,000	1.0

Table 3.1: Fe-Si matrix shear moduli and Johnson-Cook parameters

μ (GPa)	Y_0 (MPa)
9.56	250

Table 3.2: Graphite particles elastic-perfectly plastic parameters

ρ_0 (gm/cc)	c (km/s)	γ_0 (none)	a (none)	S_1 (none)	S_2 (none)	S_3 (none)
7.45	3.98	1.6	0.5	1.58	0	0

Table 3.3: Fe-Si matrix Gruneisen EOS model parameters

ρ_0 (gm/cc)	c (km/s)	γ_0 (none)	a (none)	S_1 (none)	S_2 (none)	S_3 (none)
2.20	3.90	0.24	0	2.16	1.54	-9.43

Table 3.4: Graphite particles Gruneisen EOS model parameters

3.7 References

T Antoun, L Seaman, DR Curran, GI Kanel, SV Razorenov, AV Utkin, editors; *Spall Fracture*; Springer-Verlag New York, Inc. (2003)

JR Asay, M Shahinpoor, editors; *High-pressure shock compression of solids*; Springer-Verlag New York, Inc. (1993)

L Banks-Sills, B Budiansky; *On void collapse in viscous solids*; Mechanics of Materials 1 (1982) 209-218

ZP Bazant; *Instability, ductility, and size effect in strain softening concrete;* J. Eng. Mech. Div. 102:2 (1976) 331–344

ZP Bazant, T Belytschko; *Wave propagation in a strain-softening bar: exact solution*; J. Engng. Mech. 111:3 (1985) 381-398

ZP Bazant, M Jirasek; Nonlocal integral formulations of plasticity and damage: Survey of progress; ASCE Journal of Engineering Mechanics 128:11 (2002) 1119-1149

R Becker; *The Effect of Porosity Distribution on Ductile Failure*; Journal of the Mechanics and Physics of Solids, 35:5 (1987) 577-599

DJ Benson; *An Analysis of Void Distribution Effects on the Dynamic Growth and Coalescence of Voids in Ductile Metals*; Journal of the Mechanics and Physics of Solids, 41:8 (1993) 1285-1308

MM Carroll, AC Holt; *Static and dynamic pore-collapse relations for ductile porous materials*; J. Appl. Phys. 43 (1972) 1626-1636

S Cochran, D Banner; *Spall studies in uranium*; J. Appl. Phys. 48:7 (1977) 2729-2737

R Cortes; *Dynamic growth of microvoids under combined hydrostatic and deviatoric stresses*; International Journal of Solids and Structures, 29:13 (1992) 1637-1645

TB Cox, JR Low; *An Investigation of the Plastic Fracture of AISI 4340 and 18 Nickel—200 Grade Maraging Steels*; Metallurgical Transactions, 5 (1974) 1457-1470

GE Duvall, GR Fowles; *High pressure physics and chemistry, Vol. 2* Edited by RS Bradley, Academic Press, New York (1963)

JW Hancock, AC Mackenzie; *On the mechanisms of ductile failure in high-strength steels subjected to multi-axial stress-states*; Journal of the Mechanics and Physics of Solids, 24 (1976) 147-169

Z Hashin, S Shtrikman; J. Mech. Phys. Solids, 10 (1962) 335

R Hill; Journal of the Mechanics and Physics of Solids, 11 (1963) 357-372

Y Huang; The role of nonuniform particle distribution in plastic flow localization; Mechanics of Materials, 16 (1993) 265-279

JN Johnson; *Dynamic fracture and spallation in ductile solids*; Journal of Applied Physics, 52:4 (1981) 2812-2825

GR Johnson, WH Cook; *Fracture characteristics of three metals subjected to various strains, strain-rates, temperatures, and pressures*. Engineering Fracture Mechanics, 21:1 (1985) 31-48

PE Magnusen, EM Dubensky, DA Koss; *The Effect of Void Arrays on Void Linking During Ductile Fracture*; Acta Metallurgica 36:3 (1988) 1503-1509

MA Meyers, LE Murr, KP Staudhammer, editors;*Shock-wave and high-strain-rate phenomena in materials*, Marcel Dekker, Inc. (1992) 759-767

MA Meyers; *Dynamic Behavior of Materials*; 1st Edition, John Wiley & Sons, Inc. (1994)

S Nemat-Nasser, M Hori; Micromechanics: Overall properties of heterogeneous materials; North-Holland Elsevier, 2nd Edition (1999)

AL Nichols; *Users manual for ALE3D: An arbitrary lagrange/eulerian 3D code system*; LLNL technical report, UCRL-MA-152204 Rev 6 (2007)

N Ohno, JW Hutchinson; *Plastic Flow Localization Due to Non-Uniform Void Distribution*; Journal of the Mechanics and Physics of Solids, 32:1 (1984) 63-85

M Ortiz, A Molinari; *Effect of strain hardening and rate sensitivity on the dynamic growth of a void in a plastic material*; Transactions of the ASME, Journal of Applied Mechanics 59 (1992) 48-53

H Poritsky; *The collapse or growth of a spherical bubble or cavity in a viscous fluid*; in the Proceedings of the First U.S. National Congress on Applied Mechanics, ASME, New York (1952) 813

DJ Steinberg; *Equation of state and strength properties of selected materials*; Lawrence Livermore National Laboratory Report UCRL-MA-106439 (1996)

DL Tonks, AK Zurek, WR Thissell, in *Metall. and Materials Applications of Shock-Wave High-Strain-Rate Phenomena*, edited by L. E. Murr et al, Elsevier, (1995) 171 – 178

DL Tonks in *Shock Compression of Condensed Matte: Dynamic Fracture and Fragmentation;* edited by L Davison et al. Springer Verlag New York, Inc. (1996) 237-263

V Tvergaard, A Needleman; *Effects of nonlocal damage in porous plastic solids*; International Journal of Solids and Structures; 32:8 (1995) 1063-1077

TJ Vogler, JD Clayton; *Heterogeneous deformation and spall of an extruded tungsten alloy: plate impact experiments and crystal plasticity modeling*; Journal of the Mechanis and Physics of Solids (2007) in press

ZP Wang; *Void growth and compaction relations for ductile porous materials under intense dynamic general loading conditions*; Int. J. Solids Structures, 31:15 (1994) 2139-2150

XY Wu, KT Ramesh, TW Wright; *The dynamic growth of a single void in a viscoplastic material under transient hydrostatic loading*; Journal of the Mechanics and Physics of Solids, 51 (2003) 1-26

4.0 Direct numerical simulations (DNS) of small-scale spall experiments on nodular ductile iron (NDI)

4.1 Introduction

Advances in computing capabilities now permit direct numerical simulations (DNS) of the material meso-structures of small-scale specimens under dynamic loading. DNS capture the complex interactions not readily accessible by experimental diagnostics or predictable by analytical models. Several studies have demonstrated the effectiveness of DNS in elucidating the dynamic deformation [Romanova et al. 2003, Zhang et al. 2005] and the ductile spall [Benson 1993, Tonks et al. 1995, Tonks 1996, Vogler and Clayton 2007, Becker et al. 2007] of materials. Since these previous studies were based on plane strain analyses without representative material mesostructures, they did not rigorously capture the complex, three-dimensional interactions that occur during the spall process. Computational and physical limitations have also prevented the intimate coupling of simulations with experiment, preventing the validation of DNS in previous studies.

The first objective of this chapter is to design and execute small-scale spall experiments that can be used to validate closely-coupled three-dimensional DNS. These experiments probe the effects of specimen geometry on nodular ductile iron (NDI) spall behavior under impulsive loading. Specimen geometry influences the location of the peak intensities of tensile release waves created by the reflection of a compression wave at a specimen free surface. At regions of

localized hydrostatic tensile loading, voids nucleated at the NDI second-phase particles can grow and coalesce to form spall regions. Measurements of the geometry of the spalled regions and the resulting fragment(s) can serve as a validation metric for closely-coupled DNS. Wave propagation is also influenced by the evolution of damage. At the culmination of void coalescence, an unloading wave emanates from the spalled regions. External measurements of the specimen velocity can capture the unloading wave and can also serve as a validation metric for closely-coupled DNS.

The second objective of this chapter is to perform three-dimensional DNS of the small-scale spall experiments to gain insights on the response of NDI to explosive loading. DNS can improve the understanding of the complex interactions resulting from the combination of impulsive loading and heterogeneous void structures, not otherwise accessible by experimental diagnostics. While it is known that void growth is spatially non-uniform and enhanced in void-rich regions of the material, these mechanisms are not accurately portrayed by previous analytic models of dynamic void growth. Analytic models of dynamic void growth [Poritsky 1952; Carroll and Holt 1972; Johnson 1981; Banks-Sills and Budiansky 1982; Ortiz and Molinari 1992] are based on a single, isolated void and do no capture the void growth and coalescence enhancements caused by the presence of neighboring voids. DNS can provide insights into damage evolution both near to and peripheral to the spalled regions, enabling the development of predictive void growth and coalescence models. The predictions of these closely-coupled simulations can

be directly compared to measurements of the small-scale spall experiments, as part of validating the DNS methods.

4.2 Methods

Methods were developed to compare the small-scale experimental data to DNS results. Key measurements from the small-scale spall experiments were directly compared to DNS predictions, as part of validating DNS methods. The spall strength, based on the free surface velocity (FSV) signal, and the primary spall fragment geometry were the main validation metrics. In order to improve the understanding of void growth in materials with complex microstructures, DNS results for the mean and peak void volume fraction rate were examined.

4.2.1 Small-scale spall experiments

Small-scale spall experiments were designed considering limitations for spall loading mechanism and diagnostics, as well as computational resources necessary for an integrated DNS. Previous experimental configurations were considered as part of constraining the design of these small-scale spall experiments. An explosive-drive spall experiment developed at Los Alamos National Laboratory (LANL) was selected [Mason 2007]. In this experiment, a circular plate specimen is backed by a center-detonated explosive of the same diameter. The FSV is tracked with a photonic doppler velocimetry (PDV) system. Spall fragments are decelerated in a fragment soft-capture system, reducing unintended damage subsequent to primary loading. FSV and spall fragment data were important DNS validation metrics.

4.2.1.1 Specimen geometry

Based on the computational resources, the original LANL explosive-drive spall experiment was scaled-down. Small-scale spall experiments in this study consisted of 4.0 mm diameter circular plates backed with a 4.0 mm diameter x 2.0 mm thick explosive charge, as shown in Figure 4.1 schematic. Three samples were tested, each with different thicknesses (1.0, 1.5, 2.0 mm). This resulted in a computational mesh model size of more than 50,000,000 elements using an element size of 5 μm. The computational model is discussed further in the Section 4.2.2.

4.2.1.2 Fragment soft-cature

A soft-capture setup consisting of open-cell polyurethane foam (0.05 gm/cc) was utilized to prevent secondary damage to the fragmented specimens. To prevent fragment corrosion after experiments and prior to macroscopic measurements, they were cleaned with rubbing alcohol, and then placed in plastic bags that were stored in desiccant-containing jars. Comparisons of the soft-captured and predicted fragments provided another anchoring metric for the DNS. Measurements of the primary spall fragment were performed using a macroscopic (optical) camera system. The number of measurements on each fragment varied due to its size or configuration.

4.2.1.3 Photonic doppler velocimetry (PDV) system

A PDV system was used to measure the FSV time-history for direct comparison to DNS predictions. PDV works by measuring the Doppler shift in frequency of scattered light [Strand et al. 2006]. For these experiments, a single PDV probe was directed at the center of the specimen free surface. FSV time-

histories over 10 microseconds with a temporal resolution of better than 50 nanoseconds were captured and compared to simulation predictions. Due to the small ejecta that immediately jumps off of the specimen free surface when the shock arrives, a velocity envelope is typically measured by the PDV system *after* the initial jump-off velocity (peak). These small ejecta are separate and distinct from the primary spall fragment, which typically forms later in time due to fracture at a finite depth from free surface. Due to the triggering delay, PDV data was temporally out-of-phase from the simulation data. For the purposes of comparison, the predicted FSV was aligned to PDV data at the initial jump-off velocity peak.

4.2.1.4 Spall strength calculations

An established method [Cochran and Banner 1977; Antoun et al. 2003] for determinining the spall strength, σ_{spall} , from the FSV time-histories was modified to account for the damaged state of the material:

$$\sigma_{spall} = \frac{1}{2}\overline{\rho}_0 \overline{c}_0 \Delta u_{fs} \tag{4.1}$$

$$\overline{\rho}_0 = \left(1-\Phi_0\right)\rho_0 \tag{4.2}$$

$$\overline{c}_0 = \left(1-\Phi_0\right)c_0 \tag{4.3}$$

Where $\overline{\rho}_0$ and ρ_0 (7.45 gm/cc) are the damaged and undamaged matrix density, and $\overline{c}_0$ and c_0 (3.98 km/s) are the damaged and undamaged matrix wave speed. Δu_{fs} is the pullback velocity and it is determined from the PDV data as the difference between the peak velocity and the first minima (due to spall pulse arrival) following the peak velocity. Φ_0 (0.115) is the initial macro-scopic particle

volume fraction, which is used to calculate $\bar{\rho}_0$ and $\bar{c}_0$. This modification was based on DNS predictions of void nucleation, without significant growth, in the material between the spall plane and free surface. Spall strength calculations were performed assuming the upper and lower bounds of the FSV envelope. The maximum spall strength was calculated with the lower bound of the FSV envelope (i.e., maximum Δu_{fs}) and the minimum spall strength was calculated with the upper bound of the FSV envelope (i.e., minimum Δu_{fs}).

4.2.2 Direct numerial simulation (DNS) description

4.2.2.1 Geometry

DNS geometry was based on the small-scale spall experiments. Circular NDI plates with a 4.0 mm diameter and different thicknesses (1.0, 1.5, 2.0 mm) were backed with a 4.0 mm diameter x 2.0 mm thick explosive charge. The air surrounding the NDI plate and the explosive was also modeled. This allowed the explosive gas products to advect through the air and vent through the outflow boundary condition. The outflow boundary condition was imposed to allow material to leave the simulation space without restriction, i.e., in a manner that was consistent with the actual experiments.

4.2.2.2 Particle structure

In order to accurately study spall behavior in NDI, it is important to initiate the DNS with a representative and three-dimensional particle structure. The necessity for three-dimensional particle structure was established in Chapter 1. Numerical particle generation tools developed in Chapter 2 were used to

accomplish this task. Approximately 20,000 (1 mm thick) to 40,000 (2 mm thick) particles were incorporated in these DNS.

4.2.2.3 Explosive loading

Impulsive loading on the plates was supplied entirely by the detonating explosive charge. A 1.65 gm/cc density variant of pentaerythritol tetranitrate (PETN) was employed as the explosive for these small-scale spall experiments. A density-based scaling was performed on 1.50 gm/cc and 1.75 gm/cc density PETN data [Wilkins 1999] to obtain the explosive energy per unit volume, Chapman-Jouget (CJ) pressure, detonation velocity, and the Jones-Wilkins-Lee (JWL) equation-of-state (EOS) for the explosive detonation products. Relevant PETN properties, including the JWL model parameters, are summarized in Table 4.1.

4.2.2.4 Sector (volume) and tracer (point) variable tracking

Due to the axisymmetric loading, heterogeneous particle structure, and resulting deformation gradient, the spatial domain of the specimen was radially and longitudinally partitioned into sectors for regional tracking of void volume fraction evolution. The radial and longitudinal partitioning was set at increments of 500 μm. Beyond the central core, the sectors were actually donut-shaped and their volume increased with increments in radial direction. Sector tracking of the void volume fraction evolution improved understanding of the spatial evolution of damage and formation of primary spall fragments in the simulations. Volume-

weighted sums of void volume fraction rate were taken to determine mean sector response:

$$\dot{\phi}_{sector} = \frac{\sum_{i=1}^{N_{sector,elem}} \dot{\phi}_{elem,i} V_{elem,i}}{\sum_{i=1}^{N_{sector,elem}} V_{elem,i}} \tag{4.4}$$

Where $\dot{\phi}_{sector}$ is the sector mean of the void volume fraction rate, $\dot{\phi}_{elem,i}$ is the element-based void volume fraction rate of the *ith* element contained within that sector, $V_{elem,i}$ is the volume of the *ith* element contained within that sector, and $N_{sector,elem}$ is the total number of elements in that sector.

Lagrangian tracers were placed on specimen for the purpose of measuring the FSV time-history. Since the tracers followed the material, it was possible for them to advect to adjacent elements. The tracer measured the velocity of the element they resided in. Predicted FSV time-history was compared directly to experimentally-measured data.

4.2.2.5 NDI component phase material models

Elasticity, yield surface, hardening, EOS, and failure models were separately specified for the Fe-Si alloy matrix and graphite particle phases. Model parameters were determined from a combination of experiments and literature. Since the NDI component phase material models used here were identical to those in Chapter 3, the reader is referred there for further details.

4.2.2.6 Finite element analysis code

Simulations were performed using LLNL's three-dimensional arbitrary-Lagrange-Eulerian (ALE) code, ALE3D [Nichols 2007]. ALE3D was used for these simulations because it permits seeding of the void nucleating particles across mesh lines, it handles large deformations of the matrix material around the growing void while still capturing the void-matrix interface, and it permits void coalescence as it culminates to spall fracture. Neither a lagrangian-only or eulerian-only code can adequately simulate these material behaviors. DNS had approximately 50,000,000 elements with an element size of 5 μm in the particle region. Elements were spatially graded outside of the particle region to improve computational efficiency.

A typical DNS of the small-scale spall experiment is depicted in Figure 4.2. The pressure fringe plot of the progressing detonation wave in the explosive charge is shown to induce tensile release waves on the specimen top and side free surfaces. The interaction of these tensile release waves leads to void nucleation, growth, and coalescence in the the NDI specimen.

4.3 Results

4.3.1 Small-scale spall experiments

FSV measurements for each of the three specimen thicknesses are shown in Figures 4.3, 4.4, and 4.5. FSV data is reported in terms of a velocity envelope. The velocity envelope is a direct result of the small ejecta from specimen free surface and had been previously discussed in Section 4.2.1. Upper bound, lower bound, and mean spall strengths were calculated based on Equation (4.1) and reported in Table 4.2. For the 1 mm thick specimen, the

maximum and minimum Δu_{fs} are 216 m/s and 182 m/s, respectively. This results in upper and lower bound spall strengths of 2.51 GPa and 2.11 GPa, respectively. The mean spall strength is 2.31 GPa. For the 1.5 mm thick specimen, the maximum and minimum Δu_{fs} are 212 m/s and 180 m/s, respectively. This results in upper and lower bound spall strengths of 2.46 GPa and 2.09 GPa, respectively. The mean spall strength is 2.28 GPa. For the 2 mm thick specimen, the maximum and minimum Δu_{fs} are 204 m/s and 173 m/s, respectively. This results in upper and lower bound spall strengths of 2.37 GPa and 2.01 GPa, respectively. The mean spall strength is 2.19 GPa. A slight decrease in the mean spall strength with increasing thickness is observed, especially between the two thicker specimens. However, all calculated mean spall strengths are within the spall strength bounds for all specimen thicknesses. Moreover, the upper and lower bound spall strengths do not vary by more than +/-10% of the mean value for the three configurations.

Macroscopic images of the primary spall fragments with diametric measurements for each of the three configurations are shown in Figures 4.6a-4.6c. Mean diametric measurements were performed on the primary spall fragment “bottom” surface, i.e., side initially facing explosive charge, and “top” (free) surface. Only the primary spall fragment produced in the 1.0 mm thick specimen had portions of both the top and bottom surfaces. Primary spall fragments from the 1.5 and 2 mm specimens had just the top surfaces remaining. For the 1 mm thick specimen, the mean diameter of the top and bottom surfaces was 3.7 mm and 2.5 mm, respectively. For the 1.5 mm thick specimen, the mean

diameter of the top surface was 3.6 mm. For the 2.0 mm thick specimen, the mean diameter of the top surface was 3.5 mm.

4.3.2 DNS results

4.3.2.1 DNS results *with* an experimental analog

FSV predictions for each of the three specimen thicknesses are shown with test data in Figures 4.3, 4.4, and 4.5. Spall strengths were calculated based on Equation (4.1) and reported in Table 4.3. Predicted spall strength for the 1.0 and 1.5 mm thick specimens fell within the experimental lower and upper bound spall strengths. For the 1.0, 1.5, and 2.0 mm thick specimens, the error in predicted spall strength is 1.3%, 7.9%, and 18.7%, respectively. Error increased with increasing specimen thickness.

Measurements of the predicted primary spall fragments from EPS fringe and material boundary plots are in Figure 4.7a-4.7c. Thresholding EPS fringe plots at the matrix failure strain (0.4) permitted visualization of the primary spall fragment boundaries, which consisted of varying levels of void- and shear (EPS)-related damage. For the 1 mm thick specimen, the diameter of the top and bottom surfaces was 3.8 mm and 2.3 mm, respectively. For the 1.5 mm thick specimen, the mean diameter of the top surface was 3.7 mm. For the 2.0 mm thick specimen, the mean diameter of the top surface was 3.4 mm. For the 1.0 mm thick specimen, the EPS path did not percolate completely at the mid-thickness, but rather abruptly followed a localized EPS band to the inner surface. In order to visualize the primary spall fragment for the 2.0 mm thick specimen, a material boundary plot supplemented the EPS fringe plot due to the significant

void-related damage. In fact, the most significant void growth is observed in Figure 4.7c. SEM studies on the 2.0 mm thick specimen revealed significant void growth on the specimen surface, confirming that spall was the failure mode (Figure 4.8). Figure 4.8 also illustrates the central role of the second-phase particles in void nucleation and growth in NDI.

4.3.2.2 DNS results *without* an experimental analog-regional void growth rate

Due to the axisymmetric loading, heterogeneous particle structure, and resulting deformation gradient, the spatial domain of the specimen was radially and longitudinally partitioned into sectors for regional tracking of void volume fraction rate. Peak sector and overall average void volume fraction rate versus time are shown in each Figure 4.9, 4.10, and 4.11 for the three specimen configurations. The peak sector was defined as the sector with the highest void volume fraction. For the 1 mm thick specimen, the maximum void volume fraction rate over the time-history of the peak sector and average are 0.68 and 0.14 μs^{-1}, respectively. The ratio of peak-to-average values is 4.9. For the 1.5 mm thick specimen, the maximum void volume fraction rate over the time-history of the peak sector and average are 0.72 and 0.18 μs^{-1}, respectively. The ratio of peak-to-average values is 3.9. For the 2 mm thick specimen, the maximum void volume fraction rate over the time-history of the peak sector and average are 0.68 and 0.13 μs^{-1}, respectively. The ratio of peak-to-average values is 5.2. While the maximum void volume fraction rate over the time-history of the peak

sector was approximately 0.7 μs^{-1} for all specimen thicknesses, there was some variation in the peak-to-average values.

4.4 Discussion

A capability is demonstrated to perform and integrate three-dimensional DNS with small-scale spall experiments. This capability is significant because it enables the tailoring and assessment of material microstructures under impulsive loading, as part of improving their resistance to spall fracture. Close-coupling of the simulations with experiments also enables the development of predictive structure-property models.

Comparisons of the predicted primary spall fragment dimensions and spall strength yielded good agreement with experiments. Observed geometric changes in primary spall fragment were a consequence of wave interaction alterations resulting from differences in the initial specimen thickness. Due to the center-detonation of the explosive charge, there is limited ability for the side (furthest radial extent) tensile release wave from the radial free surface to interact with the top tensile release wave in the 1 mm thick specimen. In the 2 mm thick specimen, the more prominent interaction of the side and rear tensile release waves result in substantially more void growth in the spall region. This latter point is qualitatively evident in material boundary plots of the spalled 2mm thick specimen (Figure 4.7c). DNS spall strength predictions fell within the measurement uncertainty for all but the 2 mm thick specimen. A comparison of simulated and measured FSV time-histories (Figure 4.5) reveal that despite good

agreement, the the slight underprediction at the peak velocity and overprediction at the final velocity influences this outcome.

The DNS demonstrates the spatial localization of void growth in the spalled regions of the specimen. As the damage evolves in the specimen, overall energy expenditures are focused in the spalled regions. The peak void growth rate in the spalled region was amplified four to five times that of the mean void growth rate for all specimen thicknesses. DNS permits detailed damage quantification, enabling the development of predictive void evolution models and, possibly, the development of new ultrafast, in-situ diagnostics for dynamic void growth characterization [Lorenzana et al. 2007].

4.5 Figures

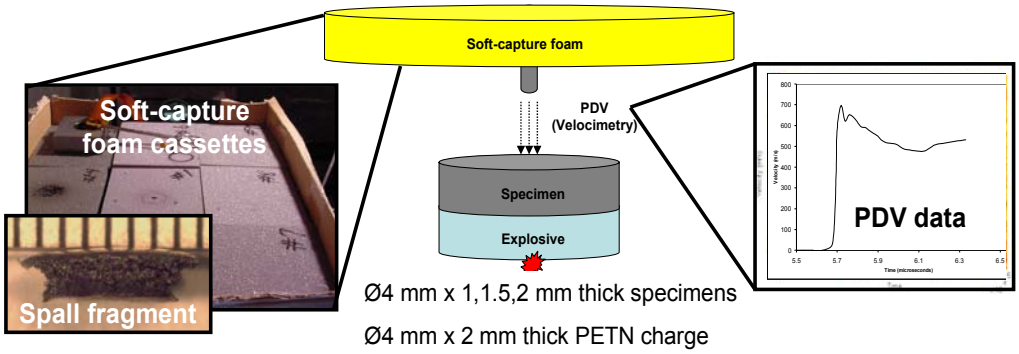

Figure 4.1: Schematic of small-scale spall experiments

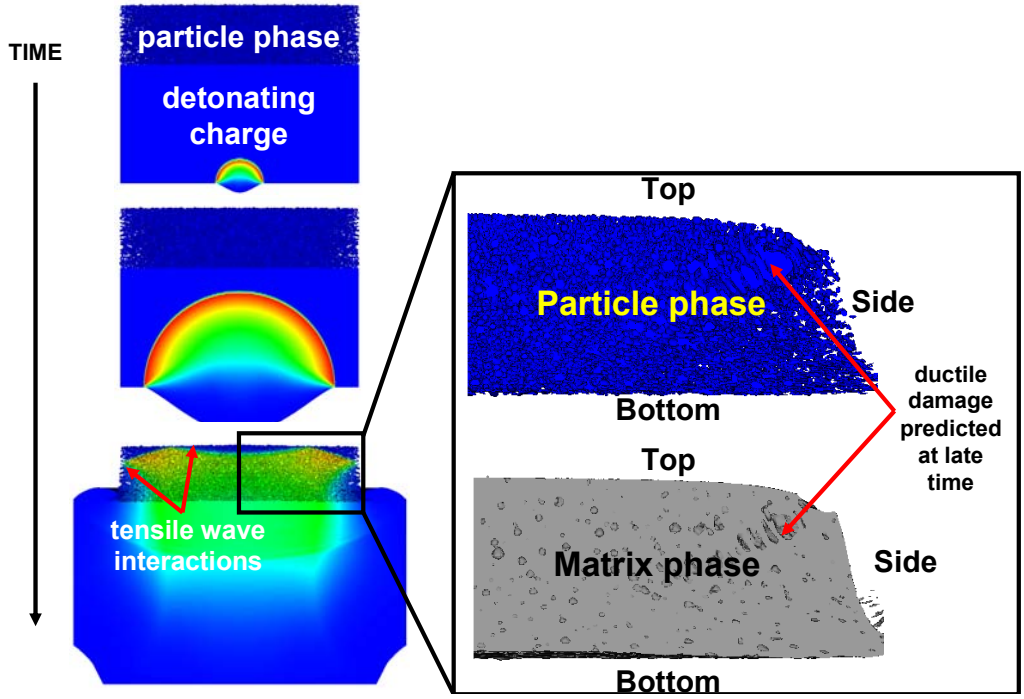

Figure 4.2: Direct numerical simulation (DNS) of nodular ductile iron (NDI) plate backed with detonating explosive charge. Pressure fringe plot of progressing detonation wave shown at left. Material boundaries of the particle and matrix phase in NDI specimen shown at right.

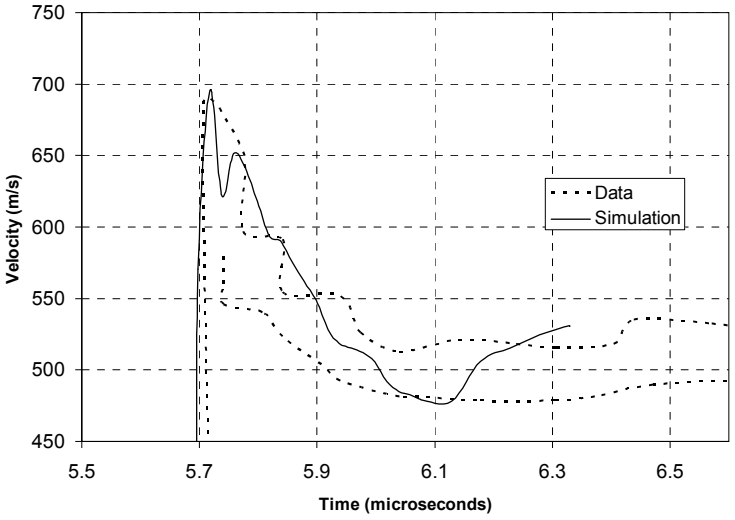

Figure 4.3: Plots of the measured and simulated free surface velocity (FSV) time-history at the center for the 1.0 mm thick specimen. The measured data is reported in terms of a velocity envelope due to the uncertainty in the photonics doppler velocimetry (PDV) diagnostics.

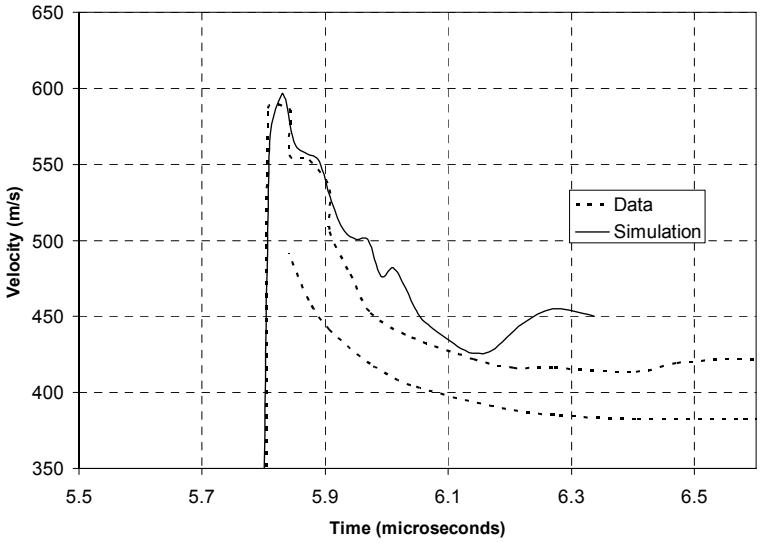

Figure 4.4: Plots of the measured and simulated FSV time-history at the center for the 1.5 mm thick specimen. The measured data is reported in terms of a velocity envelope due to the uncertainty in the PDV diagnostics.

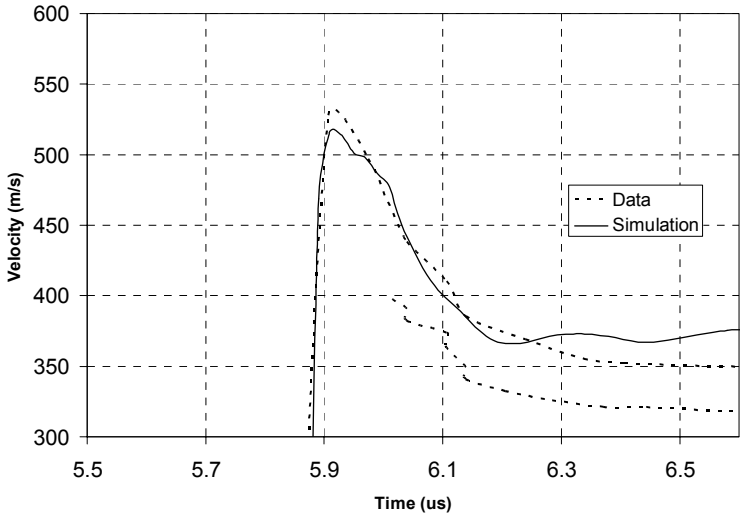

Figure 4.5: Plots of the measured and simulated FSV time-history at the center for the 2.0 mm thick specimen. The measured data is reported in terms of a velocity envelope due to the uncertainty in the PDV diagnostics.

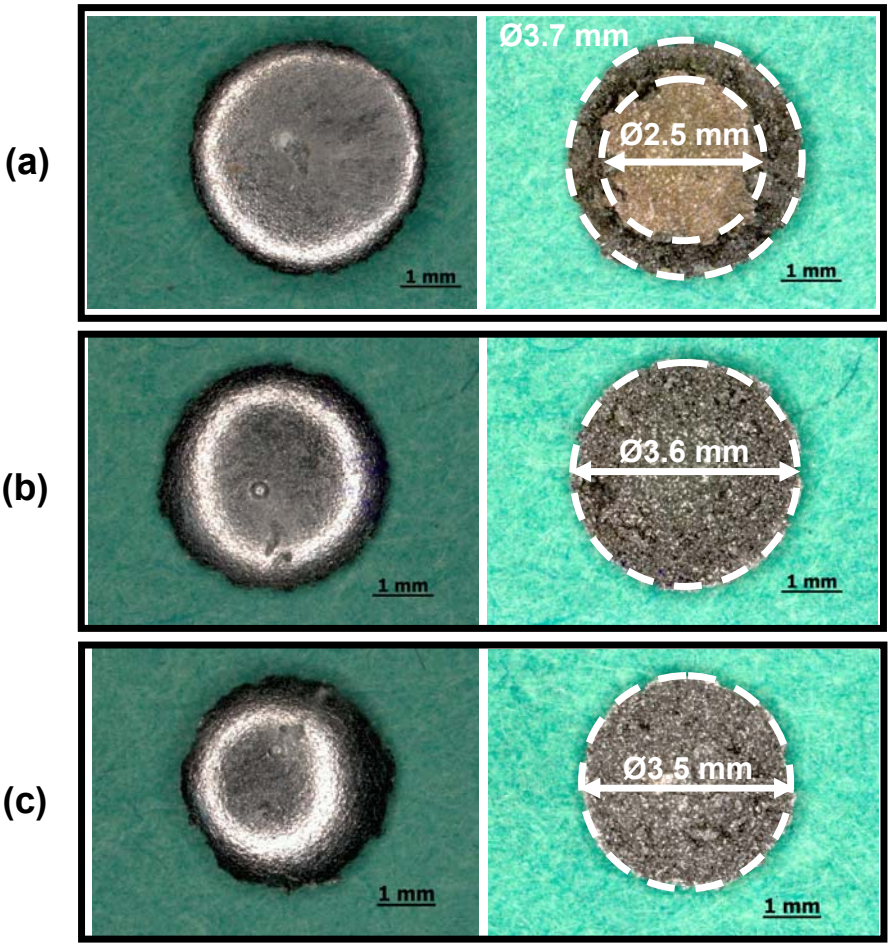

Figure 4.6: Top view (left) and bottom view with diametric measurements (right) of primary spall fragments for differing specimen thicknesses: (a) 1.0 mm, (b) 1.5 mm, (c) 2.0 mm. There are two diametric measurements in (a) corresponding to the top (at left) and bottom surface. There is one diametric measurement for each (b) and (c) corresponding to the top surface (at left).

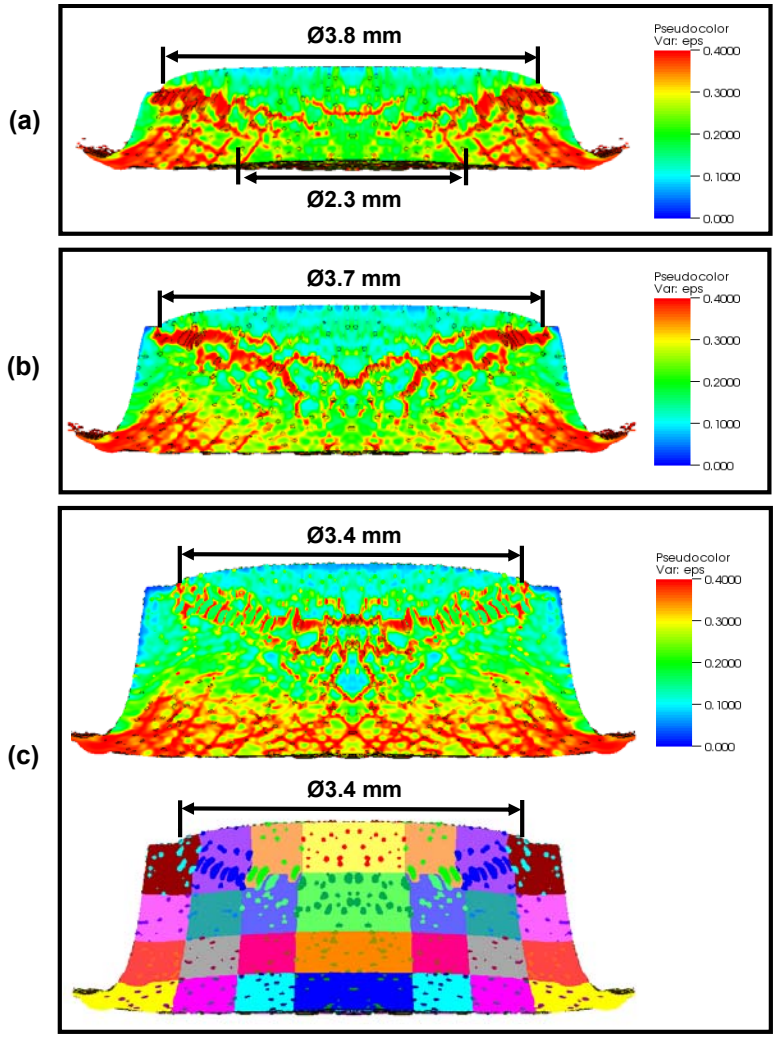

Figure 4.7: Equivalent plastic strain (EPS) fringe plots for the differing specimen thicknesses: a. 1.0 mm, b. 1.5 mm, c. 2.0 mm. A material boundary plot is also shown for the 2.0mm thick specimen. Primary spall fragment measurements are guided by using the EPS fringe plots thresholded (red) at a value of 0.4. For the 2.0 mm thick specimen, the material boundary plot showing voided regions facilitates measurements.

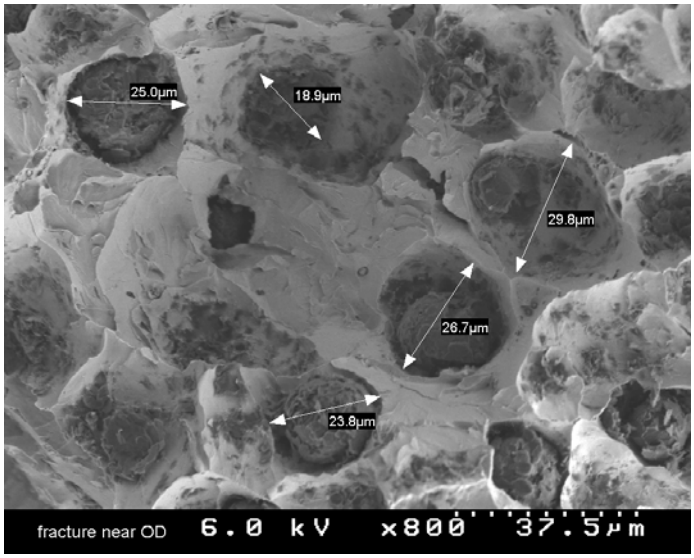

Figure 4.8: Scanning electron microscopy image of the spall surface on the primary spall fragment from the 2.0 mm thick specimen. Second-phase particles and particle remnants occupy voids.

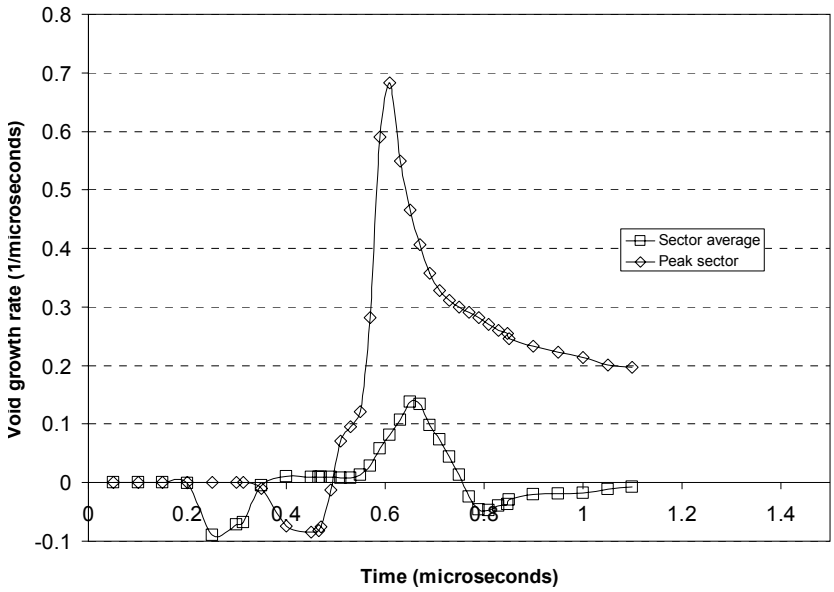

Figure 4.9: Void volume fraction rate versus time for the 1.0 mm thick specimen. The ratio of peak-to-average values is 4.9.

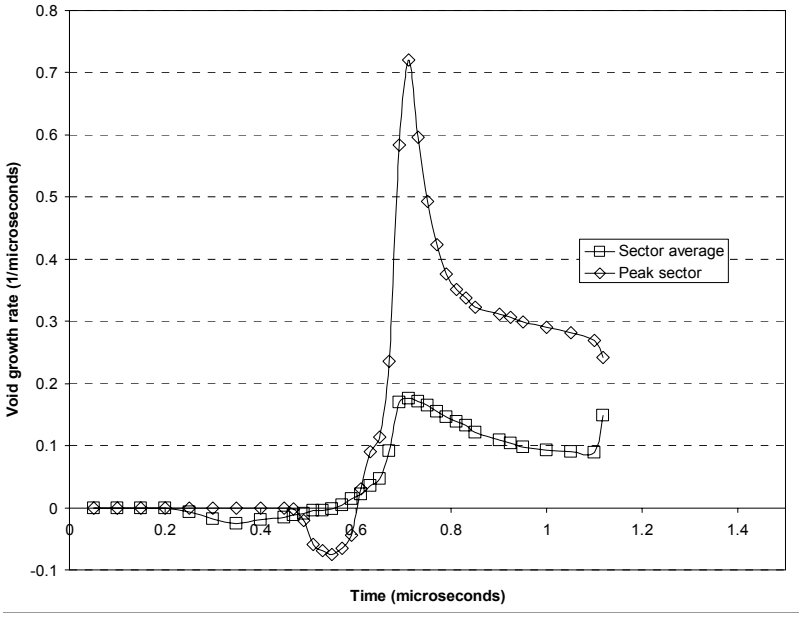

Figure 4.10: Void volume fraction rate versus time for the 1.5 mm thick specimen. The ratio of peak-to-average values is 3.9.

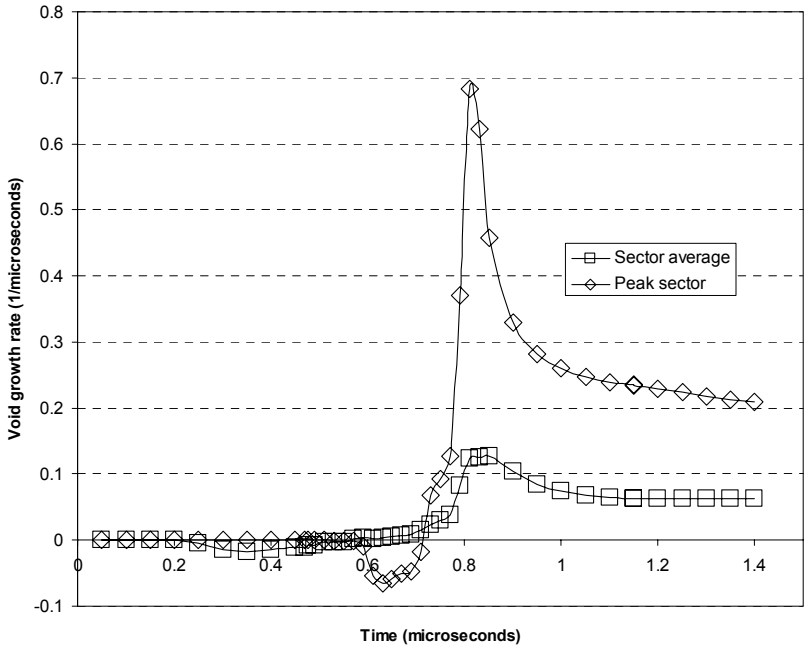

Figure 4.11: Void volume fraction rate versus time for the 2.0 mm thick specimen. The ratio of peak-to-average values is 5.2.

4.6 Tables

E_0 (GPa)	P_{CJ} (GPa)	D (km/s)	A (GPa)	B (GPa)	R_1 (none)	R_2 (none)	ω (none)
9.2	27.0	8.0	625.3	23.39	5.25	1.60	0.28

Table 4.1: PETN explosive JWL EOS parameters

$\sigma_{spall,1\text{ mm}}$ (GPa)	2.11-2.51, mean 2.31
$\sigma_{spall,1.5\text{ mm}}$ (GPa)	2.09-2.46, mean 2.28
$\sigma_{spall,2\text{ mm}}$ (GPa)	2.01-2.37, mean 2.19

Table 4.2: Experimental spall strength range and mean for each specimen based on the FSV time-history

$\sigma_{spall,1\text{ mm}}$ (GPa)	2.28
$\sigma_{spall,1.5\text{ mm}}$ (GPa)	2.10
$\sigma_{spall,2\text{ mm}}$ (GPa)	1.78

Table 4.3: DNS spall strength predictions for each specimen based on the FSV time-history

4.7 References

T Antoun, L Seaman, DR Curran, GI Kanel, SV Razorenov, AV Utkin; *Spall Fracture*; Springer-Verlag New York, Inc. (2003)

L Banks-Sills, B Budiansky; *On void collapse in viscous solids*; Mechanics of Materials 1 (1982) 209-218

R Becker, MM LeBlanc, JU Cazamias; *Characterization of recompressed spall in copper gas gun targets*; Journal of Applied Physics 102 (2007)

DJ Benson; *An Analysis of Void Distribution Effects on the Dynamic Growth and Coalescence of Voids in Ductile Metals*; Journal of the Mechanics and Physics of Solids, 41:8 (1993) 1285-1308

MM Carroll, AC Holt; *Static and dynamic pore-collapse relations for ductile porous materials*; J. Appl. Phys. 43 (1972) 1626-1636

S Cochran, D Banner; *Spall studies in uranium*; J. Appl. Phys. 48:7 (1977) 2729-2737

JN Johnson; *Dynamic fracture and spallation in ductile solids*; Journal of Applied Physics, 52:4 (1981) 2812-2825

HE Lorenzana, J Belak, G Campbell, W King, D Nikkel; Ultrafast, in situ probing of shocked solids at the mesoscale and beyond: A new paradigm for materials dynamics; LLNL Technical Report UCRL-TR-228191 (2007)

TA Mason; Private communications; (2007)

AL Nichols; *Users manual for ALE3D: An arbitrary lagrange/eulerian 3D code system*; LLNL technical report, UCRL-MA-152204 Rev 6 (2007)

M Ortiz, A Molinari; *Effect of strain hardening and rate sensitivity on the dynamic growth of a void in a plastic material*; Transactions of the ASME, Journal of Applied Mechanics 59 (1992) 48-53

H Poritsky; *The collapse or growth of a spherical bubble or cavity in a viscous fluid*; in the Proceedings of the First U.S. National Congress on Applied Mechanics, ASME, New York (1952) 813

V Romanova, R Balokhonov, P Makarov, S Schmauder, E Soppa; *Simulation of elasto-plastic behaviour of an artificial three-dimensional-structure under dynamic loading*; Computational Materials Science, 28:3 (2003) 518-528

OT Strand, DR Goosman, C Martinez, TL Whitworth, WW Kuhlow; Compact system for high-speed velocimetry using heterodyne techniques; Rev. Sci. Instr. 77 (2006)

DL Tonks, AK Zurek, WR Thissell, in *Metall. and Materials Applications of Shock-Wave High-Strain-Rate Phenomena*, edited by L. E. Murr et al, Elsevier, (1995) 171 – 178

DL Tonks in *Shock Compression of Condensed Matte: Dynamic Fracture and Fragmentation;* edited by L Davison et al. Springer Verlag New York, Inc. (1996) 237-263

TJ Vogler, JD Clayton; *Heterogeneous deformation and spall of an extruded tungsten alloy: plate impact experiments and crystal plasticity modeling*; Journal of the Mechanis and Physics of Solids (2007) in press

ML Wilkins; *Computer simulation of dynamic phenomena*; Springer Verlag (1999)

KS Zhang, MS Wu, R Feng; *Simulation of microplasticity-induced deformation in uniaxially strained ceramics by 3-D Voronoi polycrystal modeling*; International Journal of Plasticity, 21:4 (2005) 801-834

Appendix A: Relative growth rates of spherical and cylindrical voids

The objective of Appendix A is to determine the relative growth rates of spherical and cylindrical voids.This will be accomplished by deriving relationships for the void volume fraction rate of each the spherical and cylindrical voids. A single spherical void with radius, a_s, is centered in a finite spherical matrix region with radius, b_s (Figure A.1). A single cylindrical void with radius, a_c, and length, L_c, is centered in a finite cylindrical matrix region with radius, b_c with identical length (Figure A.2). The void volume fraction for a spherical void, ϕ_s, and a cylindrical void, ϕ_c, is given by

$$\phi_s = \frac{\frac{4}{3}\pi {a_s}^3}{\frac{4}{3}\pi {b_s}^3} = \left(\frac{a_s}{b_s}\right)^3 \tag{A.1}$$

$$\phi_c = \frac{\pi {a_c}^2 L_c}{\pi {b_c}^2 L_c} = \left(\frac{a_c}{b_c}\right)^2 \tag{A.2}$$

$$a_s = \phi_s^{\frac{1}{3}} b_s \tag{A.3}$$

$$a_c = \phi_c^{\frac{1}{2}} b_c \tag{A.4}$$

Taking the derivative of a_c and a_s with respect to time yields:

$$\dot{a}_s = \frac{b_s \dot{\phi}_s}{3\phi_s^{\frac{2}{3}}} + \phi_s^{\frac{1}{3}} \dot{b}_s \tag{A.5}$$

$$\dot{a}_c = \frac{b_c \dot{\phi}_c}{2\phi_c^{\frac{1}{2}}} + \phi_c^{\frac{1}{2}} \dot{b}_c \tag{A.6}$$

Substituting Equation (A.3) into Equation (A.5) and Equation (A.4) into Equation (A.6) yields:

$$\dot{a}_s = \frac{a_s \dot{\phi}_s}{3\phi_s} + \phi_s^{\frac{1}{3}} \dot{b}_s \tag{A.7}$$

$$\dot{a}_c = \frac{a_c \dot{\phi}_c}{2\phi_c} + \phi_c^{\frac{1}{2}} \dot{b}_c \tag{A.8}$$

An additional relationship between $\dot{a}_s$ and $\dot{b}_s$, and $\dot{a}_c$ and $\dot{b}_c$s acquired through the assumption that the matrix volume for the spherical void case, $V_{s,m}$, and the cylindrical void case, $V_{c,m}$, is incompressible

$$V_{s,m} = \frac{4}{3}\pi \left({b_s}^3 - {a_s}^3 \right)_s \tag{A.9}$$

$$\dot{V}_{s,m} = 3{b_s}^2 \dot{b}_s + 3{a_s}^2 \dot{a}_s = 0 \tag{A.10}$$

$$\dot{b}_s = \frac{{a_s}^2}{{b_s}^2} \dot{a}_s \tag{A.11}$$

$$V_{c,m} = \pi \left({b_c}^2 - {a_c}^2 \right) L_c \tag{A.12}$$

$$\dot{V}_{c,m} = 2b_c \dot{b}_c + 2a_c \dot{a}_c = 0 \tag{A.13}$$

$$\dot{b}_c = \frac{a_c}{b_c} \dot{a}_c \tag{A.14}$$

Substituting Equation (A.11) into Equation (A.7), Equation (A.14) into Equation (A.8), and solving for $\dot{\phi}_s$ and $\dot{\phi}_c$ yields

$$\dot{\phi}_s = \frac{3\dot{b}_s}{b_s}\left(1 - \phi_s\right) \tag{A.15}$$

$$\dot{\phi}_c = \frac{2\dot{b}_c}{b_c}\left(1 - \phi_c\right) \tag{A.16}$$

Typically in two-dimensional simulations, the void volume fraction and initial radius is assumed to be the same as the three-dimensional case

$$\phi_s = \phi_c \tag{A.17}$$

$$a_s = a_c \tag{A.18}$$

Taking the ratio of Equation (A.15) and Equation (A.16) and substituting Equation (A.17) leads to

$$\frac{\dot{\phi}_s}{\dot{\phi}_c} = \frac{3\dot{b}_s b_c}{2\dot{b}_c b_s} \tag{A.19}$$

Also, setting Equation (A.1) equal to Equation (A.2) and substituting Equation (A.18) leads to

$$a_s = \frac{b_s^3}{b_c^2} \tag{A.20}$$

It is now necessary to apply a loading condition to the spherical and cylindrical voids. A hydrostatic stress, p, is prescribed at the outer bound of each of the voids. The pressure is assumed to be equal for both cases. The work rate due to this loading for the spherical and cylindrical voids is $p4\pi b_s^2 \dot{b}_s$ and $p2\pi b_s \dot{b}_s$, respectively. The work rate is assumed to be equal for these two cases, resulting in

$$\frac{\dot{b}_s}{\dot{b}_c} = \frac{L_c b_c}{2b_s^2} \tag{A.21}$$

Substituting Equation (A.21) into Equation (A.19) yields

$$\frac{\dot{\phi}_s}{\dot{\phi}_c} = \frac{3L_c b_c^2}{4b_s^3} \tag{A.22}$$

And then substituting Equation (A.20) into Equation (A.22) provides a relatively simple relationship for the ratio of growth rates for spherical and cylindrical voids

$$\frac{\dot{\phi}_s}{\dot{\phi}_c} = \frac{3L_c}{4a_s} \tag{A.23}$$

In order to develop a relationship for L_c, we need to first relate a_c to b_c. The void volume fraction for the model material of this study, nodular ductile iron (NDI) (0.115), is substituted into Equation (A.4)

$$b_c = \frac{a_c}{(0.115)^{\frac{1}{2}}} = 2.95a_c \tag{A.24}$$

In order to satisfy plane-strain conditions, one would expect that L_c be at least as large as b_c, if not larger. If they are set equal and L_c is substituted into Equation (A.23)

$$\frac{\dot{\phi}_s}{\dot{\phi}_c} = \frac{3(2.95b_c)}{4a_s} = 2.21 \tag{A.25}$$

$\frac{\dot{\phi}_s}{\dot{\phi}_c}$ is 2.21. This assumes that a, ϕ, p, and work rate between the spherical and cylindrical void are equal. Energy (work rate) arguments do seem more appropriate for this case. Also, setting L_c equal to b_c is a relatively conservative assumption. If L_c is set to be an integer multiple of b_c, then $\frac{\dot{\phi}_s}{\dot{\phi}_c}$ would increase by that same integer multiple.

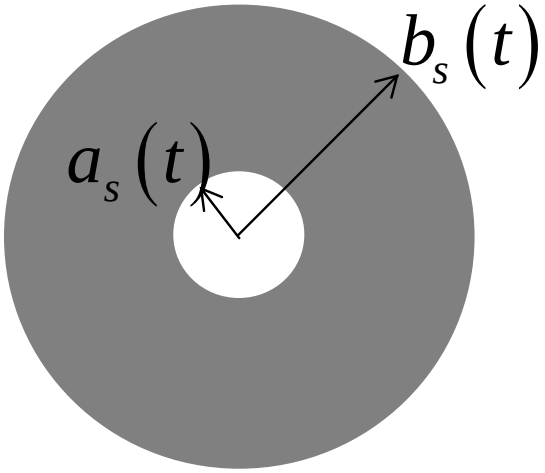

Figure A.1: Spherical void with radius, a_s, centered in a finite spherical matrix with radius, b_s.

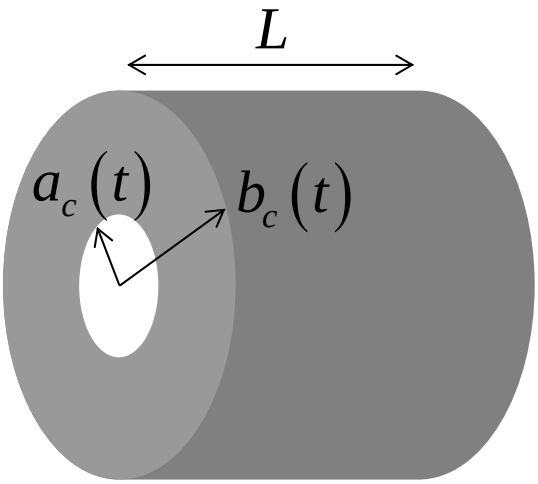

Figure A.2: Cylindrical void with radius, a_c, centered in a finite cylindrical matrix with radius, b_c.

Appendix B: Matrix sound-speed limitations on void growth

The objective of Appendix B is to determine if the matrix sound-speed limits void growth. This will be accomplished by deriving a relationship for the void radius time rate-of-change and checking if it initially exceeds the matrix material sound-speed. For this, a single spherical void with radius, a_s, is centered in a spherical matrix region with radius, b_s (Figure A.1). The void volume fraction, ϕ_s, is given by:

$$\phi_s = \frac{4/3 \pi a_s^{\,3}}{4/3 \pi b_s^{\,3}} = \left(\frac{a_s}{b_s} \right)^3 \tag{B.1}$$

$$a_s = \phi_s^{\frac{1}{3}} b_s \tag{B.2}$$

The subscript denoting that the volume fraction is that of a sphere has been dropped since only spheres are being considered in Appendix B. Taking the derivative of a_s with respect to time yields:

$$\dot{a}_s = \frac{b_s \dot{\phi}_s}{3\phi_s^{\frac{2}{3}}} + \phi_s^{\frac{1}{3}} \dot{b}_s \tag{B.3}$$

Substituting Equation (B.2) into Equation (B.3) yields:

$$\dot{a}_s = \frac{a_s \dot{\phi}_s}{3\phi_s} + \phi_s^{\frac{1}{3}} \dot{b}_s \tag{B.4}$$

An additional relationship between $\dot{a}_s$ and $\dot{b}_s$ is acquired through the assumption that the matrix volume, $V_{s,m}$, is incompressible:

$$V_{s,m} = 4/3 \pi \left(b_s^{\,3} - a_s^{\,3} \right) \tag{B.5}$$

$$\dot{V}_{s,m} = 3b_s{}^2\dot{b}_s + 3a_s{}^2\dot{a}_s = 0 \tag{B.6}$$

$$\dot{b}_s = \frac{a_s{}^2}{b_s{}^2}\dot{a}_s \tag{B.7}$$

Substituting Equation (B.7) into Equation (B.4) yields:

$$\dot{a}_s = \frac{a_s\dot{\phi}_s}{3\phi_s} + \phi_s^{\frac{1}{3}}\frac{a_s{}^2}{b_s{}^2}\dot{a}_s = \frac{a_s\dot{\phi}_s}{3\phi_s} + \phi_s\dot{a}_s \tag{B.8}$$

$$\dot{a}_s = \frac{a_s\dot{\phi}_s}{3\phi_s\left(1-\phi_s\right)} \tag{B.9}$$

In order to calculate an *initial* $\dot{a}_s$, a range of values are used for a_s (1, 25, 50, 100 μm) and ϕ_s (0.01, 0.05, 0.1, 0.15). $\dot{\phi}_s$ is set to be the maximum value predicted in Figure 3.6 (4.5/μs) and is constant. $\dot{a}_s$ is normalized by the matrix sound-speed, c (0.398 cm/ μs) ($\frac{\dot{a}_s}{c}$) and reported as a function of a_s and ϕ_s (Figure B.1). Based on this simple model, sound-speed limitations may become a concern (i.e., $\frac{\dot{a}_s}{c} \geq 1$) at volume fractions less than 0.05 and void radii greater than 25 μm. As ϕ_s decreases, $\frac{\dot{a}_s}{c}$ increases rapidly due to the asymptote at $\phi_s = 0$. Changes to $\dot{a}_s$ correlate directly with changes to a_s, assuming that all other parameters are fixed. Based on these results, sound-speed limitations are not expected to affect parameter studies in Chapter 3 since no individual study considered ϕ_s less than 0.01 and a_s greater than 25 μm. For the parameters considered in Chapter 3, $\frac{\dot{a}_s}{c}$ is not expected to exceed approximately 0.5.

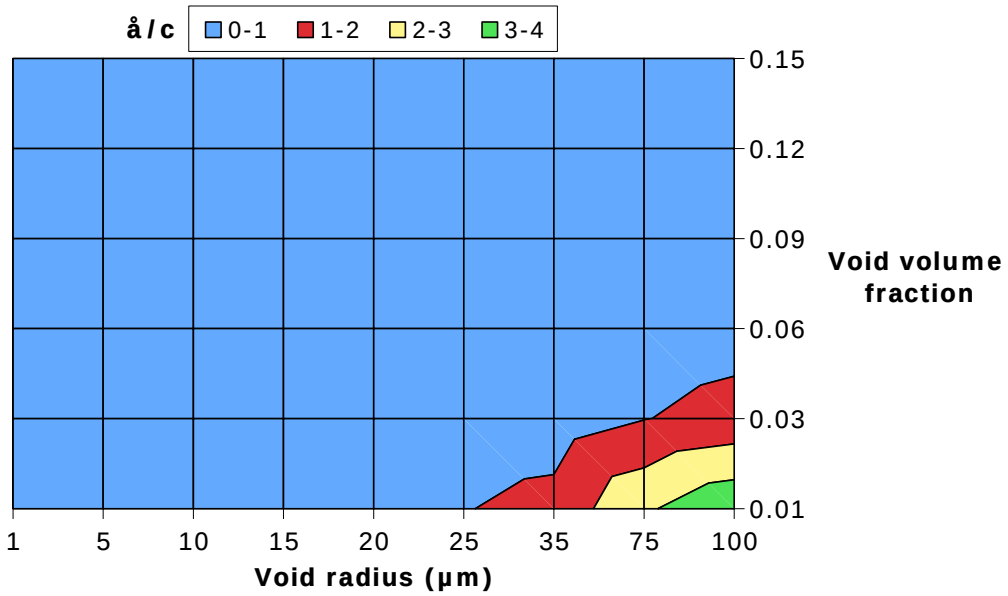

Figure B.1: The effects of void volume fraction and void radius on $\frac{\dot{a}_s}{c}$

Appendix C: Wave propagation

One dimensional wave propagation

One dimensional forms of the conservation of momentum, $\sigma_{,x} = \rho\ddot{u}$, stress-strain, $\sigma = E\varepsilon$, and the strain-displacement, $\varepsilon = u_{,x}$, equations provide the basis for one dimensional wave propagation in an elastic solid. Substituting the strain-displacement relationship into Hooke's Law, $\sigma = Eu_{,x}$, and taking the derivative wrt position yields $\sigma_{,x} = Eu_{,xx}$. Equating latter equation with the conservation of momentum equation gives

$$u_{,xx} = \frac{1}{c_b^2}\ddot{u} \tag{C.1}$$

Where the longitudinal speed is $c_b = \sqrt{\frac{E}{\rho}}$. The solution for the wave equation is well-known:

$$u(x,t) = f(x - c_b t) + g(x + c_b t) \tag{C.2}$$

This derivation assumes no body forces and small strains. The application of these equations to the split Hopkinson pressure bar experiments is discussed in the next section.

As part of this research, split Hopkinson pressure bar (SHPB) experiments were conducted to determine the strain-hardening response of materials at strain-rates of approximately 1,000-5,000/sec. SHPB experiments were essentially one dimensional uniaxial (stress) compression experiments. The one

dimensional wave equation, discussed in the previous section, is applicable to developing SHPB relationships relating the strain gage data to the specimen stress and strain-rate.

Starting with Equation (C.2), the displacement gradient and rate can be defined at each incident (subscript 1) and transmitter (subscript 2) bars:

$$u_1 = f\left(x - c_b t\right) + g\left(x + c_b t\right) \qquad u_2 = h\left(x - c_b t\right) \tag{C.3}$$

$$\dot{u}_1 = c_b\left(-f' + g'\right) = c_b\left(-\varepsilon_i + \varepsilon_r\right) \qquad \dot{u}_2 = -c_b h' = -c_b \varepsilon_t \tag{C.4}$$

$$\frac{\partial u_1}{\partial x} = f' + g' = \varepsilon_i + \varepsilon_r \qquad \frac{\partial u_2}{\partial x} = h' \tag{C.5}$$

where, ε_i is the incident strain, ε_r is the reflected strain, and ε_t is the transmitted strain. The strain data is taken directly from strain gages affixed to the incident and transmitter bar. The specimen strain-rate and stress can now be defined:

$$\dot{\varepsilon}_s = \frac{1}{L_s}\left(\dot{u}_1 - \dot{u}_2\right) = \frac{c_b}{L_s}\left(-\varepsilon_i + \varepsilon_r + \varepsilon_t\right) \tag{C.6}$$

$$\sigma_s = \frac{EA_0\left(\varepsilon_i + \varepsilon_r + \varepsilon_t\right)}{2A} \tag{C.7}$$

where, $\dot{\varepsilon}_s$ is the *specimen* strain-rate, L_s is the instantaneous *specimen* length, σ_s is the *specimen* stress, E is the Young's modulus of the *incident and transmitter bars*, A_0 is the initial cross-sectional area of the *incident and transmitter bars*, and A is the instantaneous *specimen* cross-sectional area. Since there is a finite distance between incident and transmitter bar strain gages, ε_i, ε_r and ε_t are out-of-phase. Therefore, strain gage data must be aligned before strain-rate or stress is calculated.

Three-dimensional wave propagation

For general wave propagation in an elastic solid, the three-dimensional forms of the conservation of momentum, stress-strain, and strain-displacement, equations are utilized, as well as a form for the displacement:

$$\sigma_{ij,j} = \rho \ddot{u}_i \tag{C.8}$$

$$\sigma_{ij} = 2\mu\varepsilon_{ij} + \lambda\varepsilon_{kk}\delta_{ij} \tag{C.9}$$

$$\varepsilon_{ij} = \frac{1}{2}\left(u_{i,j} + u_{j,i}\right) \tag{C.10}$$

$$u_i\left(x,t\right) = d_i f\left(p_l x_l - ct\right) \tag{C.11}$$

where, d_i is the displacement direction, p_l is the propagation direction of the disturbance, and c is the speed of the propagating disturbance. Temporal and spatial derivatives of Equation (C.11) lead to:

$$\ddot{u}_i = c^2 d_i f''\left(p_l x_l - ct\right) \tag{C.12}$$

$$u_{i,j} = d_i p_j f'\left(p_l x_l - ct\right) \tag{C.13}$$

Substituting these expressions into Equation (C.10) and then Equation (C.9) yields:

$$\varepsilon_{ij} = \frac{1}{2} f'\left(p_l x_l - ct\right)\left(d_i p_j + d_j p_i\right) \tag{C.14}$$

$$\sigma_{ij} = \left[\mu\left(d_i p_j + d_j p_i\right) + \lambda\left(d_k p_k\right)\delta_{ij}\right] f'\left(p_l x_l - ct\right) \tag{C.15}$$

Taking the spatial derivative of Equation (C.15) and substituting terms into (C.8):

$$\sigma_{ij,j} = \left[p_i\left(\mu + \lambda\right)\left(p_k d_k\right) + d_i \mu\left(p_k p_k\right)\right] f''\left(p_l x_l - ct\right) \tag{C.16}$$

$$\rho\ddot{u}_i = \rho c^2 d_i f''\left(p_l x_l - ct\right) \tag{C.17}$$

$$\sigma_{ij,j} = \rho\ddot{u}_i \rightarrow \left[p_i\left(\mu + \lambda\right)\left(p_k d_k\right) + d_i \mu\left(p_k p_k\right)\right] = \rho c^2 d_i \tag{C.18}$$

For shear waves, $\underset{\sim}{d} \perp \underset{\sim}{p}$ and so, $d_i \mu = \rho c^2 d_i \rightarrow c_s = \sqrt{\frac{\mu}{\rho}}$. For longitudinal waves, $\underset{\sim}{d} \parallel \underset{\sim}{p}$ and so, rearrange equation form to $\left[d_i \left(\mu + \lambda \right) \left(p_k p_k \right) + d_i \mu \left(p_k p_k \right) \right] = \rho c^2 d_i$.

So, $d_i \left(2\mu + \lambda \right) = \rho c^2 d_i \rightarrow c_l = \sqrt{\frac{\left(2\mu + \lambda \right)}{\rho}}$.

Appedix D: Shock compression of solids

Shock waves can form due to the compressibility of solids at very high pressures (>5 GPa) and are important to dynamic fracture modes, especially spall. Basic elements of the shock compression of solids will be developed and discussed below. These topics include the Rankine-Hugoniot jump conditions, including equation of state (EOS), and strength under uniaxial strain conditions.

Rankine-Hugoniot jump conditions

Derivation of the Rankine-Hugoniot jump conditions are for plane, one dimensional steady shock waves assuming no heat flow and no external heat sources. Considering a steady, planar shock wave with velocity, U_s, propagating through a tube of material. Where ρ is the density, u is the particle velocity, P is the pressure, and E is the internal energy per unit mass. The mass in the tube being swept over by the shock on the right in δt is $\rho_1 U_s A \delta t$ and the mass that leaves the shock front in δt is $\rho_2 \left(U_s - u_2\right) A \delta t$. These quantities are set equal, resulting in expression for mass conservation:

$$\rho_1 U_s = \rho_2 \left(U_s - u_2\right) \tag{D.1}$$

The force on the right of the shock is zero ($P_1 = 0$), while the force behind the shock is $P_2 A$. This force is equated with the time rate change of momentum, where the mass is $\rho_1 U_s A \delta t$ and the velocity is u_2, resulting in the expression for momentum conservation:

$$P_2 A = \frac{\delta\left(\overbrace{\left(\rho_1 U_s A \delta t\right)}^{mass}\overbrace{\left(u_2\right)}^{velocity}\right)}{\delta t} \tag{D.2}$$

$$P_2 = \rho_1 U_s u_2 \tag{D.3}$$

The change in energy is in terms of only the kinetic and internal energies, and is just the work (force, $P_2 A$ x distance, $u_2 \delta t$) done on the material. This results in the expression for energy conservation:

$$P_2 A u_2 \delta t = \overbrace{\frac{1}{2}\left(\rho_1 U_s A \delta t\right) u_2^2}^{\text{kinetic energy}} + \overbrace{\left(\rho_1 U_s A \delta t\right)\left(E_2 - E_1\right)}^{\text{internal energy}} \tag{D.4}$$

$$E_2 - E_1 = \frac{P_2}{2}\left(v_1 - v_2\right) \tag{D.5}$$

where v is the specific volume and can be related to the density as $\frac{v_2}{v_1} = \frac{\rho_1}{\rho_2}$.

In addition to the mass, momentum and energy conservation equations, above, a fourth equation is needed in order to solve for and relate all four variables. The approach has typically been to empirically relate the shock velocity to the particle velocity in the following polynomial form through experimentation:

$$U_s = C_0 + S_1 u + S_2 u^2 + \ldots \tag{D.6}$$

where, C_0 is the sound velocity in material at zero pressure. For most metals, the second and higher order coefficients terms are negligible and the shock-particle velocity relationship reduces to a linear form, i.e., $U_s = C_0 + S_1 u$. Marsh et al.

[1980] contains a significant amount of EOS data on both metallic and non-metallic materials.

Strength under uniaxial strain conditions

In order to evaluate the effects of material strength in one dimensional shocks, it is common to assume a uniaxial strain state in an elastic solid on the verge of yielding. Starting with Equation (C.9) in Appendix C and substituting the uniaxial strain, ε_{11} ($\varepsilon_{11} = 1 - \frac{v}{v_0}$) where appropriate results in various forms for the stresses and pressure:

$$\sigma_{11} = (2\mu + \lambda)\varepsilon_{11} \tag{D.7}$$

$$\sigma_{22} = \sigma_{33} = \lambda\varepsilon_{11} = \left(\frac{\lambda}{2\mu + \lambda}\right)\sigma_{11} = \left(\frac{\nu}{1-\nu}\right)\sigma_{11} \tag{D.8}$$

$$p = -\frac{\sigma_{kk}}{3} = -\left(\frac{\sigma_{11} + 2\sigma_{22}}{3}\right) = \frac{-\sigma_{11}}{3}\left(\frac{1+\nu}{1-\nu}\right) = -\left(\frac{2}{3}\mu + \lambda\right)\varepsilon_{11} \tag{D.9}$$

Now consider the J2 yield condition, $\sqrt{\frac{3}{2}\sigma'_{ij}\sigma'_{ij}} \le Y_0$, taken from simple uniaxial stress tests. The deviatoric stresses, σ'_{ij}, are calculated from the principal stresses and pressures, $\sigma'_{ij} = \sigma_{ij} + p\delta_{ij}$:

$$\sigma'_{11} = \sigma_{11} - \left(\frac{\sigma_{11} + 2\sigma_{22}}{3}\right) = \frac{2}{3}(\sigma_{11} - \sigma_{22}) \tag{D.10}$$

$$\sigma'_{22} = \sigma'_{33} = \sigma_{22} - \left(\frac{\sigma_{11} + 2\sigma_{22}}{3}\right) = \frac{1}{3}(\sigma_{22} - \sigma_{11}) \tag{D.11}$$

Equations (D.10) and (D.11) are then substituted into the J2 yield condition:

$$\sqrt{\frac{3}{2}\left[\left(\frac{2}{3}(\sigma_{11} - \sigma_{22})\right)^2 + 2\left(\frac{1}{3}(\sigma_{22} - \sigma_{11})\right)^2\right]} = \sigma_{11} - \sigma_{22} \tag{D.12}$$

$$\sigma_{11} - \sigma_{22} = \sigma_{11} - \left(\frac{\nu}{1-\nu}\right)\sigma_{11} = \sigma_{11}\left(\frac{1-2\nu}{1-\nu}\right) \leq Y_0 \qquad \text{(D.13)}$$

The Hugoniot elastic limit (σ_{HEL}) is the *stress in the direction of the shock at initial yield*.

$$\text{At yield, } \sigma_{11} \equiv \sigma_{HEL} = \left(\frac{1-\nu}{1-2\nu}\right)Y_0 \qquad \text{(D.14)}$$

$$\sigma_{11} - p = \frac{2}{3}\left(\sigma_{11} - \sigma_{22}\right) = \frac{2}{3}Y_0 \qquad \text{(D.15)}$$

For many metals, the value of the Poisson ratio is on the order of 0.25 to 0.33, resulting in HELs on the order of 1.5 to 2.0 Y_0. At high pressures, the difference between the σ_{11} and p becomes relatively small and the pressure-volume relationship tends to dominate material response.